FINITE-ELEMENT MODELLING OF THE GERBIL MIDDLE EAR

Nidal Elkhouri

Department of Biomedical Engineering
McGill University,
Montréal, Québec
February 2006

A thesis submitted to the Faculty of Graduate Studies and Research in partial fulfillment
of the requirements of the degree of
Master of Engineering

Your file Votre référence
ISBN: 978-0-494-24954-3
Our file Notre référence
ISBN: 978-0-494-24954-3

ABSTRACT

Hearing loss is the third leading chronic disability after arthritis and hypertension, and the most frequent birth defect. Non-invasive diagnoses and middle-ear prostheses are often unsatisfactory, partly because of a lack of understanding of middle-ear mechanics. The focus of this thesis is to develop a 3-D finite-element model to quantify the mechanics of the gerbil middle ear. An MRM dataset with a voxel size of 45 μm, and an x-ray micro-CT dataset with a voxel size of 5 um, supplemented by histological images, are the basis for 3-D reconstruction and finite-element mesh generation. The eardrum model is based on moiré shape measurements. The material properties of all the structures in the model are based on *a priori* estimates from the literature.

The behaviour of the finite-element model in response to a static pressure of 1 Pa is analyzed. Overall, the model demonstrates good agreement with low-frequency experimental data. For example, (1) the ossicular ratio is found to be about 3.5; (2) maximum footplate displacements are about 34.2 nm ± 0.04 nm; (3) the motion of the stapes is predominantly piston-like; (4) the displacement pattern of the eardrum shows two points of maximum displacements, one in the posterior region and one in the anterior region. The results also include a series of sensitivity tests to evaluate the significance of the different parameters in the finite-element model. Finally, in an attempt to understand how the overall middle-ear mechanics is influenced by the anterior mallear ligament and the posterior incudal ligament, results are shown for cutting or stiffening the ligaments.

RÉSUMÉ

La perte d'audition représente la troisième principale incapacité chronique après l'arthrite et l'hypertension, et le défaut de naissance le plus fréquent. Les diagnostics non-invasifs et les prothèses de l'oreille moyenne sont souvent insatisfaisants, en partie à cause d'un manque de compréhension de la mécanique de l'oreille moyenne. Le centre de cette thèse consiste à développer un modèle d'éléments finis à trois dimensions pour mesurer les mécanismes de l'oreille moyenne de la gerbille. Un ensemble de données de MRM avec une taille de voxel de 45 μm, et un ensemble de données de radiographie micro-CT avec une taille de voxel de 5 μm, supplémentés par des images histologiques, servent de base à la reconstruction et la génération en trois dimensions de mailles d'éléments finis. Le modèle du tympan est basé sur des mesures de forme, de type moiré. Les propriétés matérielles de toutes les structures dans le modèle sont basées sur des estimations *a priori* de la littérature.

Le modèle d'éléments finis est soumis à une pression statique de 1 Pa appliquée sur le tympan. Dans l'ensemble, les résultats du modèle sont en bon accord avec les données expérimentales de basse fréquence. Par exemple, (1) le rapport ossiculaire est d'environ 3,5; (2) les déplacements du « footplate » est d'environ 34 nm ± 0.04 nm; (3) le mouvement du stapes ressemble essentiellement à celui d'un piston; (3) les résultats du tympan montre deux points de déplacements maximums, l'un dans la région postérieure et l'autre dans la région antérieure. Les résultats incluent également une série de tests de sensibilité pour évaluer l'importance des différents paramètres dans le modèle d'éléments finis. Finalement, afin d'essayer de comprendre comment la mécanique globale de l'oreille moyenne est influencée par le ligament malleaire antérieur et le ligament incudal postérieur, des résultats montrent des cas où les ligaments sont coupés et raidis.

ACKNOWLEDGEMENTS

I would like to thank my supervisor, Professor W. Robert J. Funnell, for all his help and guidance throughout this work.

I am also thankful to my colleagues Qi Li, Fadi Akache and Chadia Mikhael for their support, and especially Liu Hengjin for his excellent work on generating volumetric meshes.

I would like to thank M.M. and O.W. Henson, Jr., of the University of North Carolina at Chapel Hill, for the MRI data; W.F. Decraemer, of the University of Antwerp, for the micro-CT data; and M. von Unge, of the Karolinska Institute in Stockholm, for the histological data.

I am forever indebted to my parents Fahd and Nina Elkhouri for their unconditional love and support, and for encouraging me to pursue my goals.

This work was supported by the Canadian Institutes of Health Research (CIHR) and the Natural Sciences and Engineering Research Council (NSERC).

TABLE OF CONTENTS

LIST OF FIGURES

LIST OF TABLES

CHAPTER 1

INTRODUCTION

According to The Hearing Foundation of Canada, hearing impairment – meaning complete or partial loss of the ability to hear in one or both ears – affects 1 in 10 Canadians (THFC, 2005). The National Library of Medicine states that 1 in 3 North Americans over 60 years old, and 40 to 50 % of those over 75, develop hearing loss. Hearing loss can result from a variety of problems: congenital defects, tumours, infections, brain injuries, ageing, etc. In fact, it is the most common birth defect: six in every thousand babies are born with hearing loss, including profound deafness (THFC, 2005). Often this is not discovered until the children are 3 years old and their language is noticeably delayed.

Located between the outer and inner parts of the ear, the middle ear is the site of many infections and birth defects, among other problems. Middle-ear prostheses and non-invasive diagnostic tools are often unsatisfactory. Hence, over the past decade, many groups have conducted experimental work on mammalian middle ears. In particular, gerbils are becoming popular for middle-ear research, in part because they are inexpensive and their middle-ear structures are easily approachable. For a better understanding of middle-ear mechanics, models are often used and validated by comparison with experimental data.

Lumped-parameter models were the first models used to study the acoustics of the middle-ear. Although these models are able to replicate experimental data, their parameters are not closely tied to anatomical or physiological data. Nowadays, finite-element models are popular in middle-ear research. They are based on anatomical shapes, biological material properties, and realistic boundary conditions and loading conditions. The application of such models to middle-ear research was first introduced by Funnell (1975), and has since evolved. However, over the past 30 years, there have been very few finite-element models of non-human species. Furthermore, model geometries have been greatly over-simplified and material properties have often been based on curve fitting.

The focus of this research was to develop a 3-dimensional finite-element model of the gerbil middle ear, and to quantify its mechanics. The model was based on *a priori* material-property estimates from the literature. Its geometry was defined accurately with the use of magnetic resonance imaging, x-ray micro-computed tomography data and moiré topography. Previous experimental measurements on gerbil middle ears were used for comparison with the finite-element model. This work will contribute to a better understanding of the normal (and ultimately the pathological) middle ear, to the design of prostheses, and to diagnostic and teaching methods.

A general overview of the human and gerbil auditory systems will be presented in Chapter 2. A review of the fundamentals of middle-ear mechanics will be the focus of Chapter 3. Chapter 4 briefly introduces the basic concepts of the finite-element method. The methods employed in this work (MRM, X-ray micro-CT, moiré topography, histology, image segmentation and mesh generation) will be explained in detail in Chapter 5. A thorough description of the final model is presented in Chapter 6 and the results are summarized in Chapter 7. Finally, conclusions and future work are discussed in Chapter 8.

CHAPTER 2

ANATOMY OF THE MIDDLE EAR

2.1 Introduction

The following sections will provide a general description of the middle ear. This chapter will begin by presenting in section 2.2 an extensive introduction to the anatomy of the human ear. This section is based on several sources, including Wever & Lawrence (1954), Wolff *et al.* (1957), Vander *et al.* (2004) and Drake *et al.* (2005) among others. The gerbil ear, and its similarities to and differences from the human one, will be the subject of Section 2.3.

2.2 Human middle ear

The auditory system is designed to detect sound signals important for survival. The peripheral auditory system is divided into three components: the outer ear, the middle ear and the inner ear (Figure 2.1). Sound vibrations are funnelled through the auricle and along the external auditory canal. They strike the eardrum, which links the external auditory canal to the manubrium of the malleus – the first of three bones connected in series, also known as 'ossicles' (malleus, incus and stapes). The ossicles, located in the air-filled middle ear, are attached to the middle-ear cavity walls by ligaments and muscles. They vibrate and the footplate of the stapes – the third and last bone of the ossicular chain – moves in the oval window. Movement of the stapes causes the liquid inside the inner ear to move. This causes movement of the cochlear duct, which causes hair cells to set off nerve impulses. These impulses are carried to the brain via the cochlear nerve. The brain then interprets these electrical impulses as sound.

The remainder of this anatomical description will be restricted to the middle ear, as it is most relevant to this research.

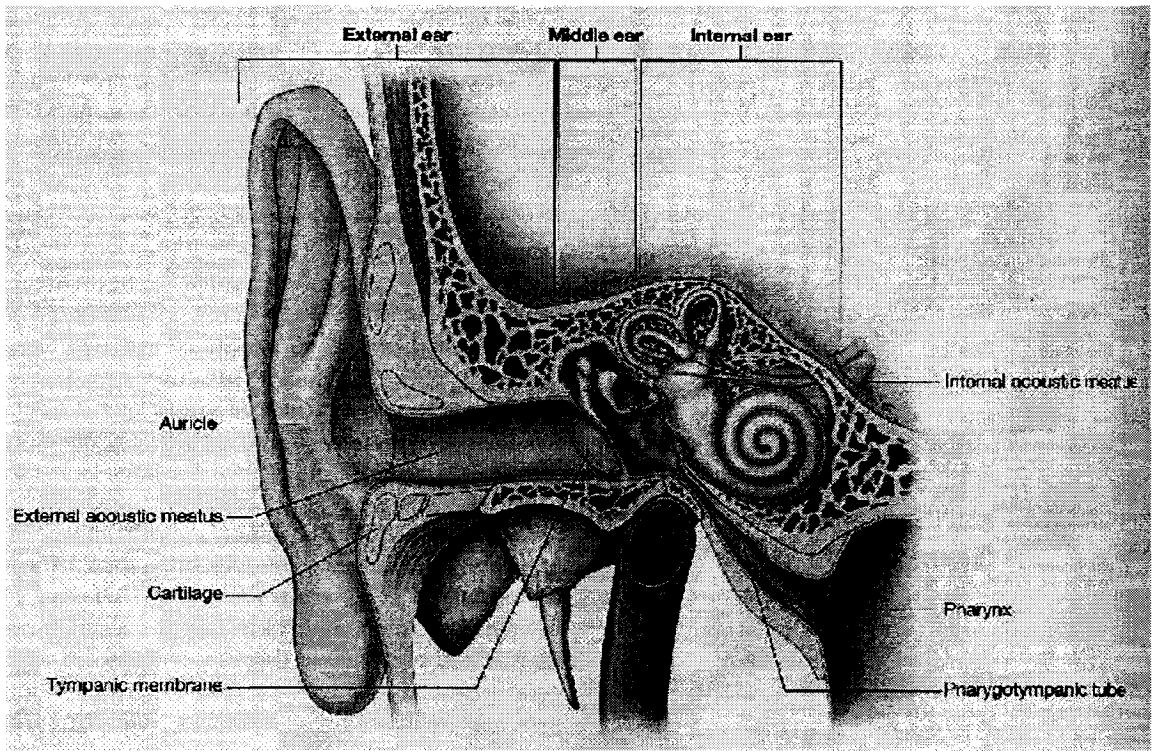

Figure 2.1: *Human auditory system (Drake et al., 2005)*

2.2.1 Middle-ear boundaries

Figure 2.2 is a schematic representation of the boundaries of the middle ear. They consist of a roof, a floor, and anterior, posterior, medial and lateral walls:

- *Roof:* The roof separates the middle ear from the middle cranial fossa. It is a thin layer of bone called the tegmen tympani.
- *Floor:* The floor consists of a thin layer of bone separating the middle ear from the internal jugular vein.
- *Lateral wall:* The lateral wall of the middle ear consists of the tympanic membrane and the encircling ring of bone. It is not shown in Figure 2.2 because it is the near wall.
- *Posterior wall:* The posterior (or mastoid) wall can be divided into two parts. The lower part consists of a bony partition between the tympanic cavity and the mastoid air cells, and the upper part consists of the epitympanic recess. The tendon of the

stapedius muscle extends from the pyramidal eminence (a bony wall surrounding the hole through which the stapedius muscle projects) to enter through this posterior wall

- *Anterior wall:* The lower part consists of a thin layer of bone separating the tympanic cavity from the internal carotid artery. The upper part contains an opening for the Eustachian (pharyngotympanic) tube, and a smaller opening for the tensor tympani muscle.
- *Medial wall:* The medial (or labyrinthine) wall is characterized by a rounded bulge (the promontory) created by the cochlea in the inner ear. Other structures associated with the medial wall are the oval window (an opening, covered by a very thin membrane, which leads from the middle ear to the vestibule of the inner ear) and the round window of the inner ear.

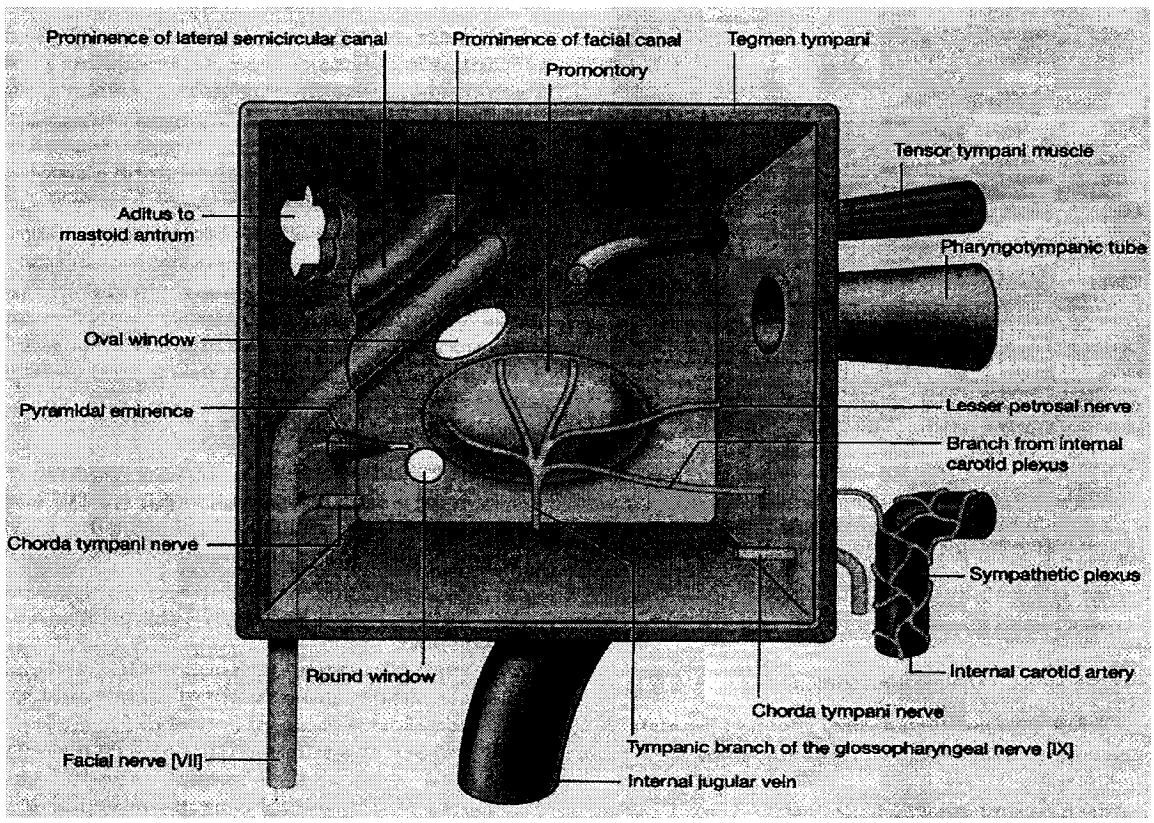

Figure 2.2: *Middle-ear boundaries (Gray's anatomy, 2005), as viewed from outside the lateral wall. The left-hand and right-hand walls are the posterior and anterior walls, respectively.*

2.2.2 Middle-ear cavities

The middle-ear cavity is an air-filled space in the petrous bone. It is approximately 2 cm^3 in volume (Békésy, 1949). It can be represented as consisting of three compartments:

- *Mesotympanum*: Located just medial to the tympanic membrane, it contains the two muscles of the middle ear, the stapes, and parts of the malleus and incus.
- *Epitympanum*: Located just superior to the tympanic membrane, it includes the head of the malleus and the body of the incus. It is also called the epitympanic recess.
- *Hypotympanum*: It is located inferior to the tympanic membrane. It is relatively wide. The opening of the Eustachian tube is found in the antero-inferior part.

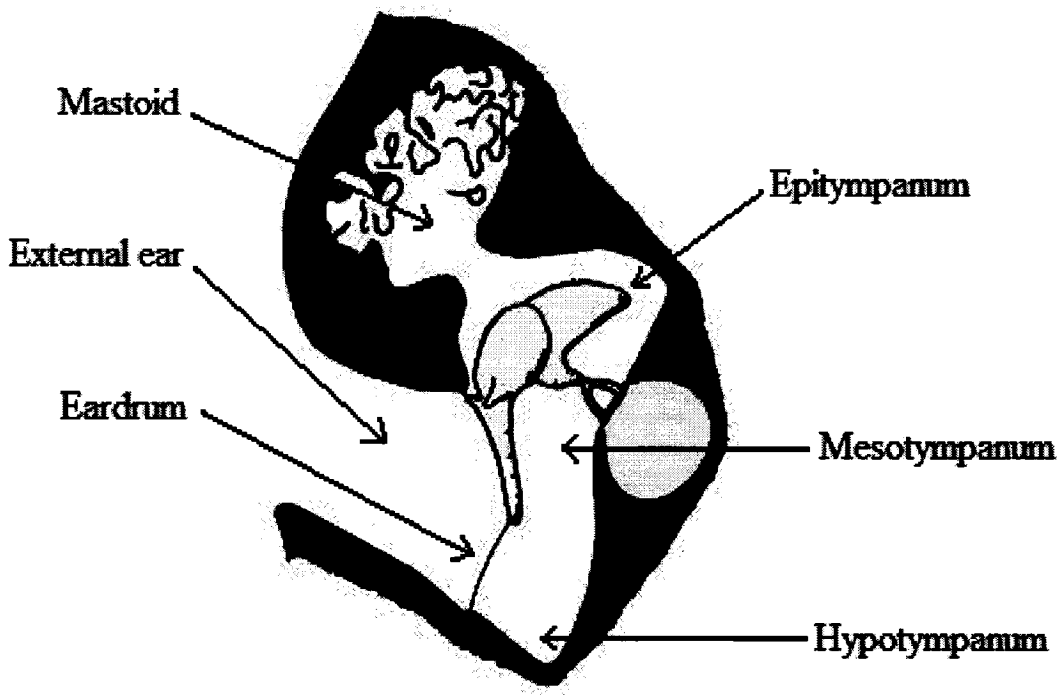

Figure 2.3: *Middle-ear spaces (modified from http://audilab.bmed.mcgill.ca/~funnell/AudiLab/teach/me_saf/me_saf.html)*

2.2.3 Tympanic membrane

The eardrum, or tympanic membrane (TM), separates the medial end of the external auditory canal from the middle-ear cavity. It is inclined at an angle (variable amongst

individuals), sloping medially from top to bottom and posteriorly to anteriorly. When observing the TM with an otoscope, a bright reflection known as the cone of light is visible antero-inferior to the umbo. The diameter of the TM along the manubrium is 8.5-10 mm, and perpendicular to the manubrium is 8-9 mm (Bezold, 1882).

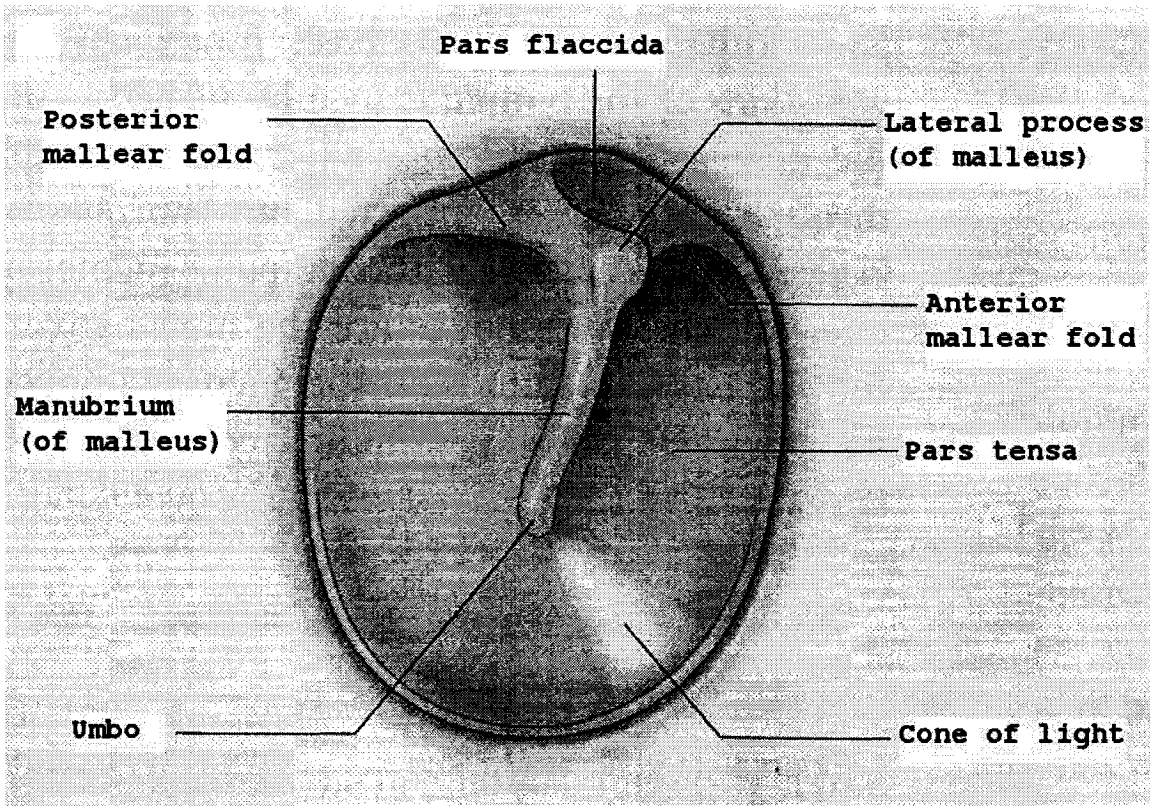

Figure 2.4: *Tympanic membrane (Gray's anatomy, 2005)*

The TM consists of two major parts: the pars tensa and the pars flaccida, shown in Figure 2.4. The pars tensa is somewhat round and conical in shape, with the apex pointing medially. The apex is located at the umbo, where the tip of the manubrium is attached. The inward offset of the umbo is about 2 mm (Siebenmann, 1897). Encircling the pars tensa is a fibrocartilaginous ring that is attached to the temporal bone. The pars flaccida is smaller and more elastic than the pars tensa, thus contributing much less to the vibrations of the ossicles (von Unge et al., 1991; Dirckx et al., 1998). As shown in Figure 2.5, the pars tensa is composed of three layers:

- *Epidermal* (*lateral*): The cutaneous layer is continuous with the skin lining of the ear canal.
- *Endodermal* (*medial*): The mucosal layer is continuous with the lining of the middle-ear cavity.
- *Mesodermal* (*fibrous*): Between the epidermal and endodermal layers, the fibrous lamina propria is composed of four layers: radial fibres which diverge from the manubrium of the malleus; circular fibres concentrated around the circumference but sparse and scattered in the centre of the TM; and two loose connective-tissue layers – subepidermal and submucosal – which lie between the radial and circular fibres of the lamina propria.

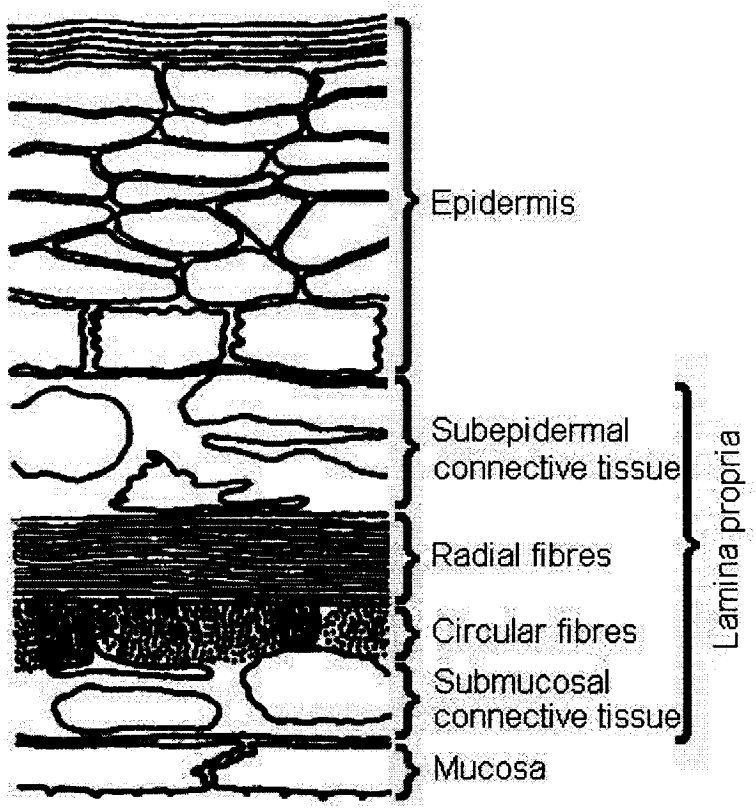

Figure 2.5: *Layers of the tympanic membrane (source: http://audilab.bmed.mcgill.ca/~funnell/AudiLab/teach/me_saf/me_saf.htm)*

This nicely organized structure of the pars tensa is not observed in the pars flaccida. In all mammalian species, the PF contains fewer collagen fibres than the PT, with an irregular arrangement of loose connective tissue (Lim, 1968 & 1970).

2.2.4 Ossicular chain

As mentioned previously, the ossicular chain consists of three ossicles - the malleus, the incus and the stapes. The first is attached to the TM, the last to the oval window of the inner ear, and the incus is connected to both by means of a joint – the incudomallear and incudostapedial joints. Figure 2.6 illustrates the location of the three ossicles in the ossicular chain.

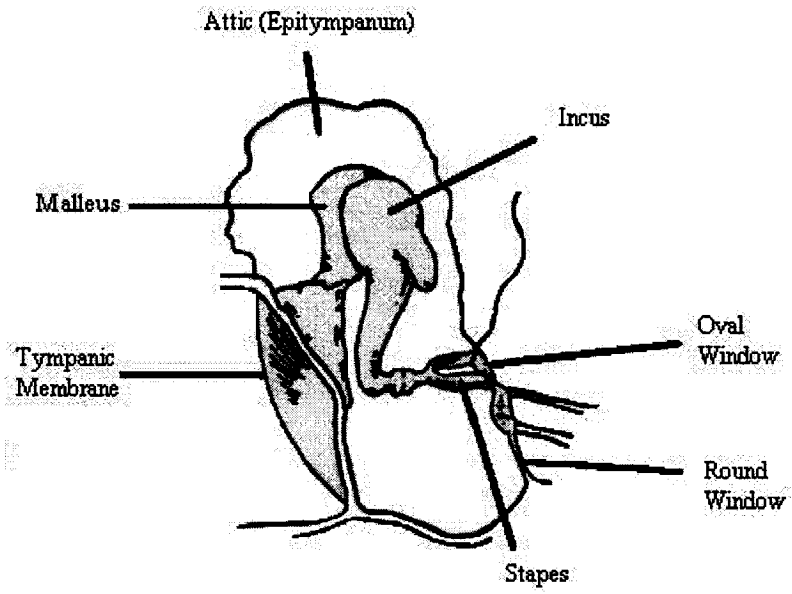

Figure 2.6: *Middle-ear ossicles (source: http://www.bcm.edu/oto/studs/anat/tbone.html)*

2.2.4.1 Malleus

The most lateral ossicle is the malleus, or hammer. It is composed of a head, a neck, a manubrium, and anterior and lateral processes. The head is the large upper extremity of the bone. It is somewhat rounded and oval in shape, and articulates posteriorly with the

body of the incus. The neck is the narrow part that bridges the head and the manubrium. The manubrium is oriented downward, medially and posteriorly. It connects to the tympanic membrane via a ligament running along its entire length. It decreases in size towards its lower end, where the tip connects to the umbo of the TM. Near its upper end, on the medial side, is a slight projection into which the tensor tympani tendon is attached. The anterior process protrudes from below the neck and is attached to the anterior wall by the anterior mallear ligament. The lateral process springs from the root of the manubrium, directed laterally. It is attached to the upper part of the TM, and to the extremities of the notch of Rivinus (a notch in the upper part of the bony ring surrounding the eardrum) by means of the lateral mallear ligament. Figure 2.7 illustrates the dimensions of the malleus.

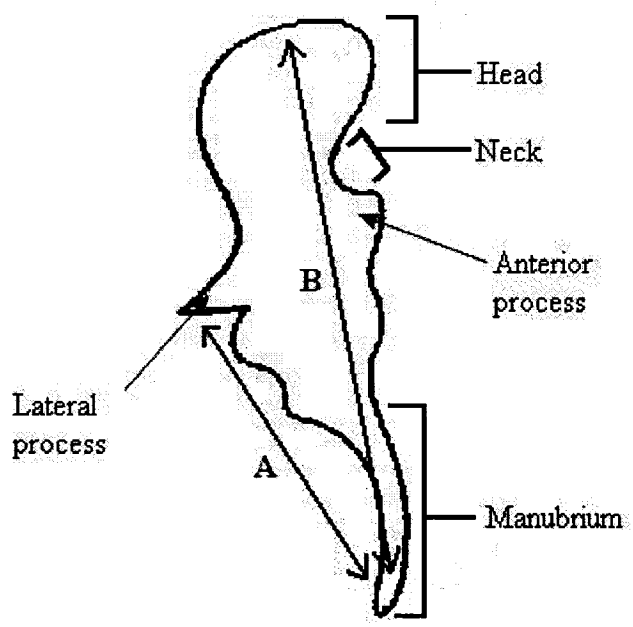

Figure 2.7: *Average dimensions of the malleus (modified from http://sprojects.mmi.mcgill.ca/oto3d/middle_ear.html). Length A, from end of manubrium to end of lateral process: 5.8 mm (Stuhlmann, 1937). Total length B: 7.6-9.1 mm (Bast & Anson, 1949).*

2.2.4.2 Incus

The incus is the second and largest bone of the middle-ear. It is also called the anvil, because it is acted on by the hammer. It consists of a body and two processes. The anterior surface of the body of the incus is saddle-like in shape, and articulates with the head of the malleus. At the other end of the incus body is the short process, somewhat conical in shape. It projects horizontally backward, and is attached to the mastoid wall by the medial and lateral bundles of the posterior incudal ligament. The long process extends nearly vertically downward from the body, and near its tip bends medially to form a rounded projection, the lenticular process, which articulates with the head of the stapes. Figure 2.8 is an illustration of the incus. Between the long process of the incus and the lenticular process is a narrow bony structure that is easily overlooked: the pedicle. Shaped like a wide and thin beam, its possible function has only recently been studied. It is believed to be prone to bending (Siah, 2002, Funnell *et al.*, 2005). Figure 2.9 shows a CT-scan image of the pedicle, illustrating how thin it is in one direction.

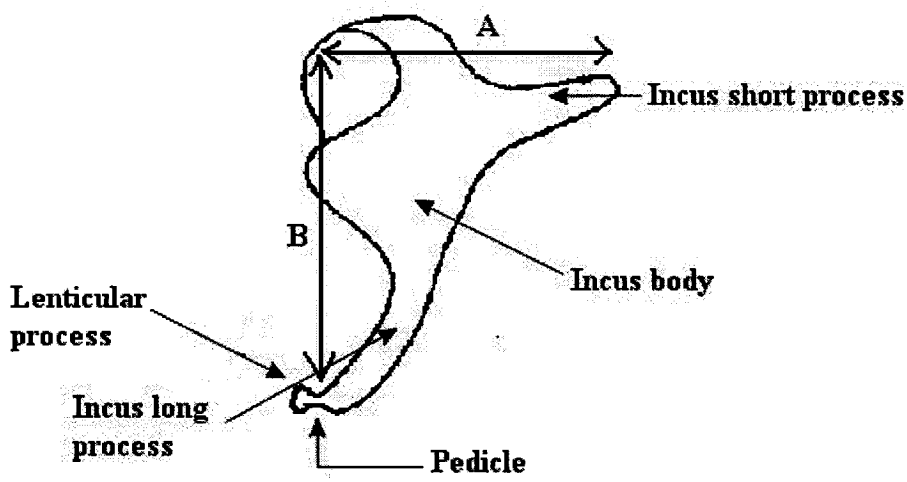

Figure 2.8: *Average dimensions of the incus . Length A, along short process: 5.0 mm. Length B, along long process: 7.0 mm. (after Stuhlman, 1937)*

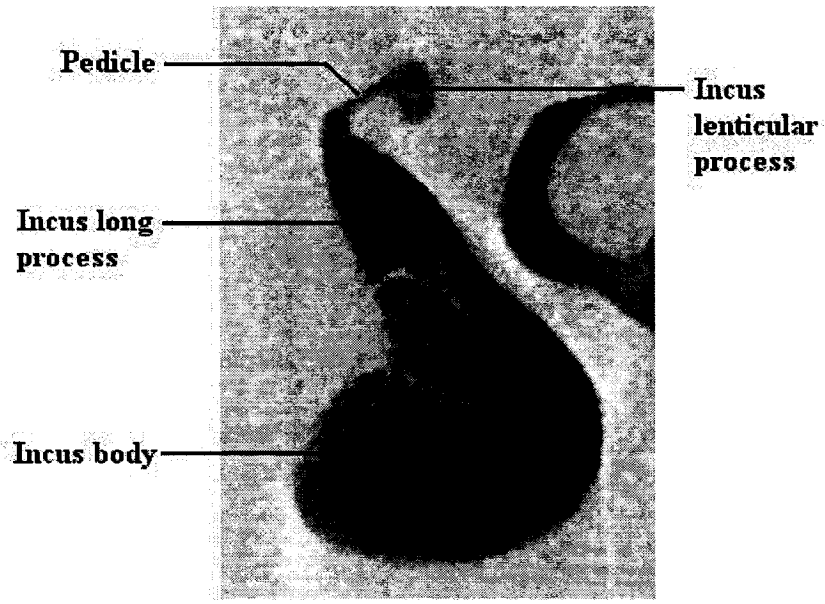

Figure 2.9: *CT-scan image of the pedicle (from the micro-CT dataset used in this work, Cf. Section 5.3.1)*

2.2.4.3 Stapes:

At the medial end of the ossicular chain lies the stapes, the smallest bone in the human body, named for its resemblance to a stirrup. Figure 2.10 illustrates the different parts: the head, anterior and posterior crura, and the footplate. The lateral surface of the head presents a slight depression which articulates with the lenticular process of the incus. Generally, the stapedius muscle joins the posterior crus to the pyramidal eminence, which is a small projection on the mastoid wall. In some cases, this muscle is connected to the head as well as to the posterior crus. The two crura diverge from the head to form a stapedial arch, and are connected at the ends to the oval footplate. The anterior crus is shorter and less curved than the posterior crus (which varies in curvature and thickness amongst individuals). The footplate connects to the oval window of the inner ear through the fibrous annular ligament. The footplate is about 20 times smaller in area than the tympanic membrane.

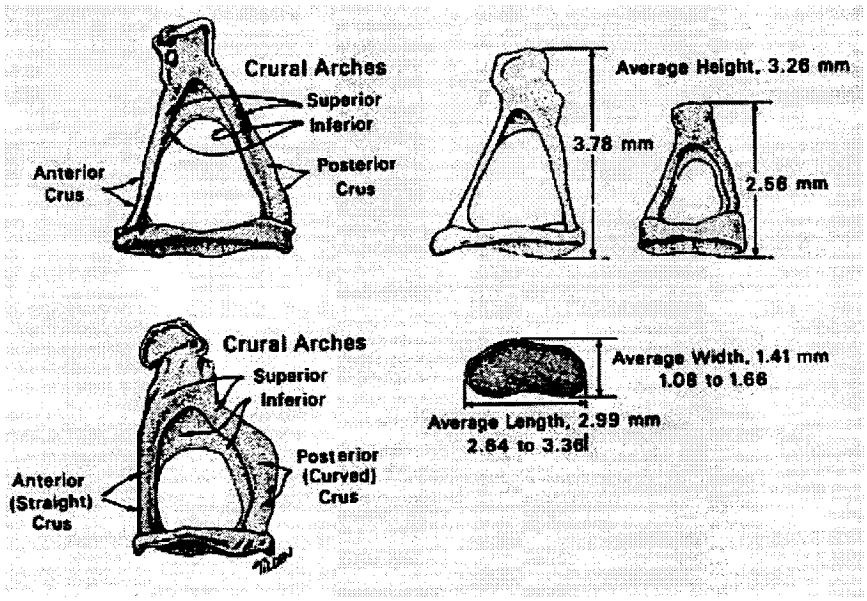

Figure 2.10: *Average stapes dimensions (Bast & Anson, 1949)*

2.2.5 Middle-ear joints

As mentioned previously, the ossicular chain is linked by two synovial joints: the incudomallear and incudostapedial joints. The former is a saddle-shaped joint (Figure 2.11). The latter connects the surfaces of the convex lenticular plate and the concave stapes head (Figure 2.12). Each joint is composed of a synovial space, a ligamentous capsule and two compartments of articular cartilage at the extremities of the articulating bones (Gulya & Schuknecht, 1995). The ligamentous capsules consist of three layers – mucous, fibrous and synovial membranes. Their main mechanical function is to hold the bones together, and prevent the synovial fluid from leaking out. The latter lubricates the joint, allowing smooth articulation.

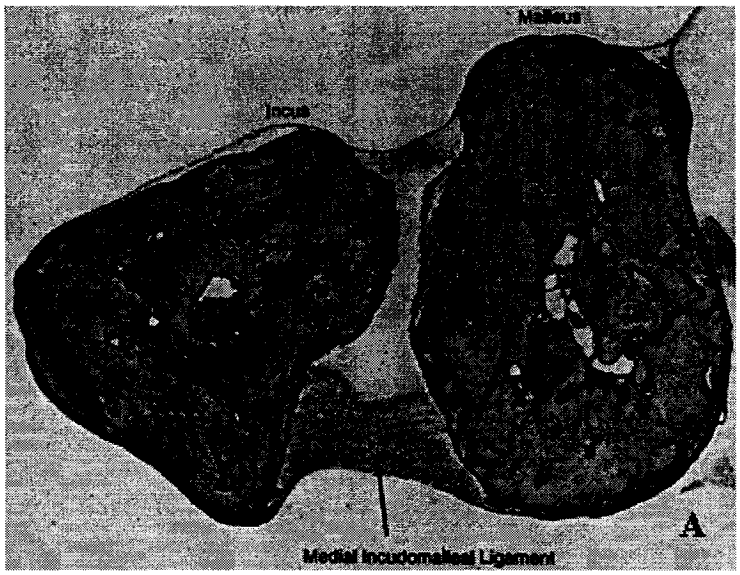

Figure 2.11: *Incudomallear joint (Gulya & Schuknecht, 1995). The joint capsule consists of what is labelled here as the 'medial incudomalleal ligament' and the smaller fibrous band on the other side of the joint.*

Figure 2.12: *Incudostapedial joint (Gulya & Schuknecht, 1995)*

2.2.6 Middle-ear muscles

The middle ear contains two muscles acting as antagonists – the tensor tympani and the stapedius (Figure 13).

The tensor tympani muscle is a striated muscle which is contained in a bony canal of the temporal bone, just above the Eustachian tube. It ends in a tendon in the tympanic cavity, and attaches to the antero-medial surface of the manubrium of the malleus. During contraction, this muscle pulls the TM medially to increase its tension and decrease the amplitude of vibrations.

The smallest skeletal muscle in the human body, the stapedius muscle emerges from the pyramidal eminence in the posterior wall of the middle ear, where its fibres converge in a conical shape to form the stapedius tendon. It attaches to the head and/or posterior crus of the stapes. It is composed of both striated and non-striated fibres. This muscle pulls the head of the stapes posteriorly during contraction, to prevent excessive vibrations.

Ligaments and muscles help to protect and stabilize the ossicular chain. However, the function of the muscles is not clearly understood. Muscles play a role in controlling (or reducing) the eardrum's vibration intensity. They contract mainly in response to high-intensity sounds, as a result of an 'acoustic reflex'. Thus, they protect the cochlea by reducing the sound transmission. Prof. Harald Feldmann (as cited by Huttenbrink, 1996) suggested that middle-ear muscle contraction controls the circulation of synovial fluid in the joints.

The existence of smooth-muscle fibres has been reported in bats (Henson & Henson, 2000), in gerbils (Yang & Henson, 2002), and in other species. In humans, the evidence is less clear so far (Henson *et al.*, 2001). These smooth-muscle fibres consist of radially oriented collagen fibres attaching the TM to the fibrocartilaginous ring. Their location suggests that they have a role in regulating the tension of the TM.

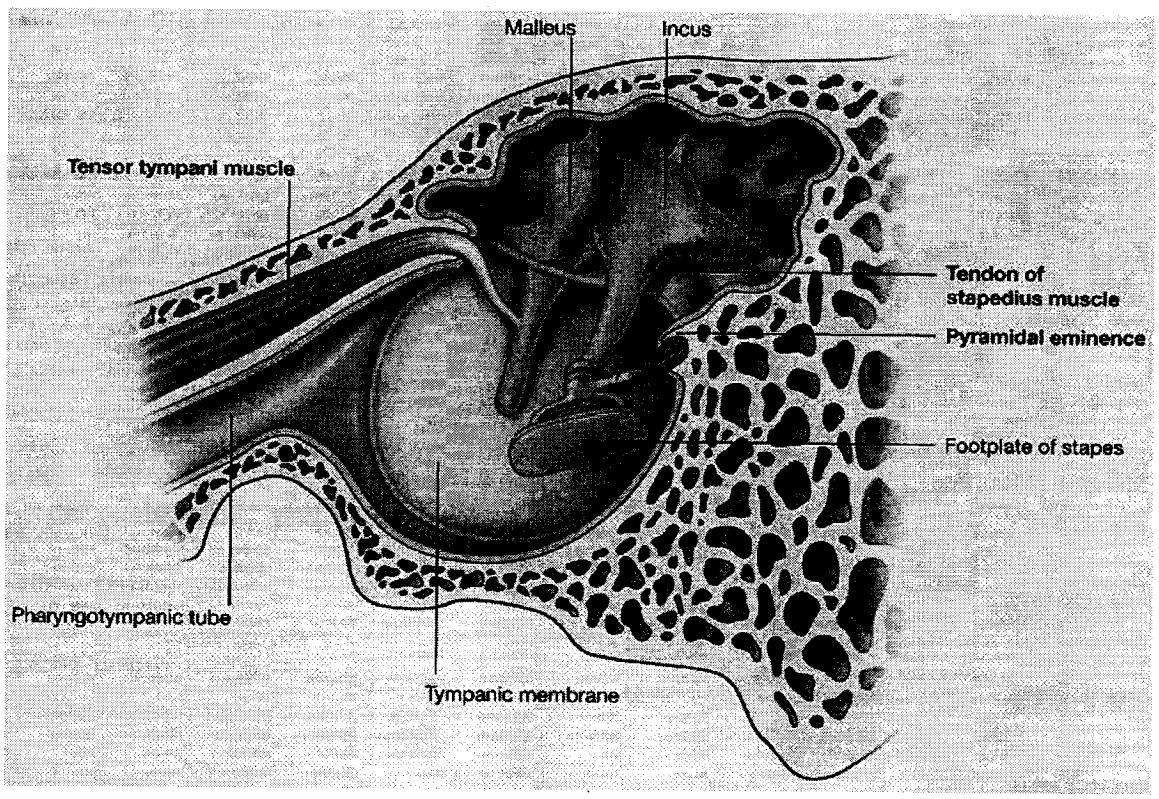

Figure 2.13: *Middle-ear muscles and ligaments (Gray's anatomy, 2005)*

2.2.7 Middle-ear ligaments

The number of ligaments is still subject to disagreement. The following descriptions are based in large part on a review by Mikhael (2005).

2.2.7.1 Mallear ligaments

- *Anterior mallear ligament (AML)*: This ligament originates from the anterior wall of the tympanic cavity, close to the petrotympanic fissure, and is inserted into the anterior process of the malleus. This ligament forms one end of the natural axis of rotation of the ossicles.
- *Lateral mallear ligament (LML)*: The fibres of this ligament form a triangular shape, and fan out from the posterior part of the notch of Rivinus to the head of the malleus (Palva *et al.*, 2001).
- *Superior mallear ligament (SML)*: A slender, rounded bundle passing from the roof

of the epitympanic recess to the head of the malleus (Wolff *et al.*, 1957).

- *Posterior mallear ligament (PML)*: The existence of such a ligament is still subject to disagreement. Some authors believe that it is a thick portion of the posterior mallear fold connecting the neck of the malleus to the pretympanic spine (Gulya & Schuknecht, 1995).
- *Suspensory ligaments*: There is a lot of controversy as to the existence of these ligaments, at least partly because of a difference in terminology. Gulya & Schuknecht (1995) have observed anterior (ASL), superior (SSL) and lateral (LSL) suspensory ligaments. The LSL and LML have similar insertion points, as do the SSL and SML. The ASL is said to be above the AML.

2.2.7.2 Incudal ligaments

The posterior incudal ligament (PIL) consists of two short and thick bundles connecting the lateral and medial aspects of the posterior end of the short process of the incus to the posterior incudal recess.

2.2.7.3 TM-malleus attachment

The manubrium is strongly attached to the TM at the umbo and at the lateral process, where the ligament is fibrous. In the middle, the ligament is mucosal, and thus forms a weaker attachment. In the upper third, where the distance between the manubrium and the TM is largest, the fibres are slender and long (Graham *et al.*, 1978).

2.2.7.4 Annular ligament

The stapes annular ligament consists of radially-oriented elastin fibres attaching the stapes footplate to the oval window.

2.3 Gerbil middle ear

In this thesis, Mongolian gerbils (*Meriones unguiculatus*) are used. Mongolian gerbils are rat-like animals. They are abundantly widespread across Shansi province of China and the Gobi Desert (China-Mongolia). Oaks (1967, pp. 78 ff.) divided the middle ears of the Gerbillinae subfamily into essentially four types, *Meriones unguiculatus* having type 2.

There are many similarities between the gerbil and human middle-ears. Differences arise mainly when comparing cavity size and the orientation of the TM and ossicles. What follows is a brief description, based on Oaks (1967), of the Mongolian gerbil middle ear, and some highlights of differences between it and the human middle-ear. From this point on, the Mongolian gerbil will simply be referred to as "gerbil".

The TM of the gerbil has about the same orientation as the human TM. The cross section of the manubrium is relatively flat in humans but T-shaped in gerbils. As in humans, the manubrium of the malleus and the long process of the incus are not perpendicular to the ossicular axis, but slant slightly forward and backward respectively. The malleus and incus are not fused together. In gerbils, the only attachments of the ossicles to the walls of the tympanic cavity are the two muscles, the anterior mallear ligament and the posterior incudal ligament, and the TM-manubrium attachment. The manubrium is tightly connected to the TM along its whole length.

The middle-ear air space in gerbils has a volume of about $0.2cm^3$, which represents about a tenth of the volume of the human middle-ear cavity, and about 5 times that of rats and hamsters, rodents of similar body size (Oaks, 1967). According to Rosowski et al. (1999), large middle-ear air spaces play a role in improving hearing sensitivity at frequencies below 2–3 kHz in gerbils.

The gerbil has a relatively large pars flaccida (PF). In humans, the PF surface area is 2-3% of the pars tensa (PT) surface area. In gerbils, the figure goes up to 10-20% (Dirckx et al., 1998). However, its actual function is not understood.

CHAPTER 3

MIDDLE-EAR MECHANICS

3.1 Introduction

In this chapter we shall first begin with an overview of middle-ear mechanics. In the second part, a review of experimental observations of vibration patterns of the eardrum and ossicles will be presented. Finally, we shall define the assumptions of our finite-element model in the third part of this chapter.

3.2 Middle-ear mechanics

3.2.1 Acoustical impedance

The middle ear acts as a transformer mechanism between the air-filled external ear and the liquid-filled inner ear. If the sound waves were passed directly from air to the liquid, the intensity would decrease greatly, since the acoustical impedance of air is about 3880 times smaller than that of sea water (Wever & Lawrence, 1954, p. 72). Acoustical impedance is commonly denoted by the letter Z, and is defined by the following equation:

$$Z=\frac{P}{U}$$

where P is the sound pressure, and U is the volume velocity (area times velocity). When sound waves travel from a compartment of low Z to a compartment of high Z, the higher the Z of the second compartment, the more energy is reflected and the less energy enters the second compartment.

The middle ear is designed to reduce the loss of hearing sensitivity. The energy-transfer mechanism of the middle ear is complex, but is often described as a combination of three simple factors: the eardrum-to-stapes **surface area ratio**, the **lever mechanism** of the ossicles, and the **eardrum curvature**.

3.2.2 Surface-area mechanism

Pressure is defined by

$$P = f \cdot A$$

where f is the applied force, and A is the effective surface area. Assuming that a force f_1 applied on the eardrum is equal to the resulting force f_2 at the stapes, the force balance is:

$$\frac{P_1}{A_1} = \frac{P_2}{A_2}$$

Since the effective surface area of the eardrum (A_1) is greater than that of the footplate (A_2), the pressure created by the stapes (P_2) must be greater than the pressure on the eardrum (P_1).

The gain in pressure is equal to the ratio of the two effective surface areas. The effective area of the eardrum is the cross-sectional area of a rigid piston that displaces a volume of air equal to that which is displaced by the deformed eardrum. The effective area is some fraction of the anatomical area. Békésy's eardrum vibration results on fresh human cadavers indicated that the eardrum vibrates like a rigid plate. He found that the human eardrum effective area is about two-thirds of the total area. The effective surface area of the stapes is the cross-sectional area of the footplate, assuming piston-like motion. In humans, the effective surface areas are said to be about 55 mm^2 and 3.2 mm^2 for the eardrum and stapes, respectively (Wever & Lawrence, 1954). The surface-area ratio is thus about 17.

Complex behaviour patterns of both the eardrum (Khanna & Tonndorf, 1972) and stapes (Decraemer *et al.*, 2000) have been reported, as discussed in Section 3.3. This complicates the determination of the effective areas.

3.2.3 Ossicular lever mechanism

The second impedance-transfer mechanism assumes a fixed axis of rotation running from the anterior process of the malleus to the posterior incudal ligament. The malleus and incus together would act as a lever, and the lever arms would be determined by the perpendicular distances from the axis of rotation to the umbo and to the incudostapedial joint. This simple lever ratio would contribute to the increase in stapes pressure. Wever & Lawrence (1954) reported a ratio of about 1.31 in human, and a ratio of about 2.5 in cat. However, the axis of rotation has been shown to shift with changes in frequency (e.g., Gyo et al., 1987; Decraemer & Khanna, 1994). At high frequencies, moreover, the incus and malleus exhibit significant relative motion, and they cannot be assumed to behave as a single unit.

3.2.4 Eardrum curvature

Originally proposed by Helmholtz (1869), this mechanism involves a relationship between the eardrum's curvature and the sound-pressure amplification. The eardrum vibration study on fresh human cadavers by Khanna & Tonndorf (1972) supported the curved-membrane hypothesis of Helmholtz. Khanna & Tonndorf (1972) invoked the effect of the eardrum's curvature, and its radial and circular fibre architecture, on amplifying the incoming sound pressure before it hits the manubrium. Funnell (1996) studied the coupling of forces from different points on the eardrum to the manubrium by means of a finite-element model of the cat eardrum. According to Funnell, "certain regions of the eardrum are more effective in driving the manubrium than can be explained on the basis of their distance from the axis of rotation". This additional effectiveness was due to the curvature of the eardrum and, contrary to what Helmholtz assumed, required neither tension nor anisotropy. Its effect is probably relatively small.

3.2.5 Conclusion

There is no clear way to separate the force-transformation mechanism into these three distinct factors (eardrum/footplate area ratio, ossicular lever-arm ratio, and curvature transformation ratio). The characteristics of the overall pressure-to-force transformation can only be determined as a combination of these three factors as well as the effects of inertia and damping at higher frequencies.

3.3 Experimental observations of vibration patterns

3.3.1 Eardrum

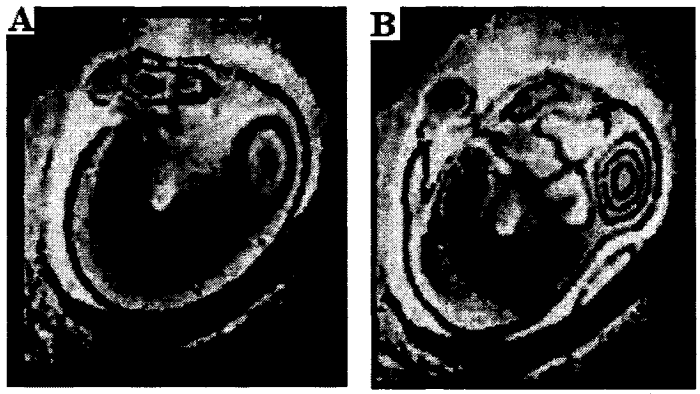

Figure 3.1: *Vibration pattern of human eardrum obtained from time-averaged holograms (Khanna & Tonndorf, 1972): (A) 522 Hz at 116 dB, and (B) 5069 Hz at 113 dB.*

Figure 3.1-A shows a low-frequency vibration pattern for a human eardrum obtained from time-averaged holograms (Khanna & Tonndorf, 1972). The alternating bright and dark lines result from holographic interference, each of them representing a specific amplitude of vibration. These isoamplitude contours are well identified in the posterior region (on the right-hand side of the figure), with a maximum displacement in the centre of the region. The amplitudes are smaller in the anterior region (left-hand side of the figure), with a maximum vibration zone just anterior to the manubrium. Figure 3.1-B shows the more complex vibration pattern of the eardrum at a high frequency. The authors reported that the simple low-frequency vibration pattern starts to break up at a transition frequency of about 2 kHz. Decraemer & Khanna (1996) – in cats – reported a transition frequency of about 2.5 kHz. In fresh human cadavers, Dirckx & Decraemer (1991) also observed maximum eardrum displacement regions, one on each side of the manubrium. Their experiments were done at much lower frequencies than those of Khanna & Tonndorf (1972), and the displacements were much larger in magnitude.

There is a lack of eardrum vibration data in gerbil. In this work, we shall characterize eardrum displacement by its maximum value, and by the ratio of its maximum value to the displacement at the umbo. These measures are commonly used to summarize eardrum motion and its effect on the ossicles. We shall also look at eardrum displacement patterns and compare our results to those obtained in human and cat.

3.3.2 Ossicles

Békésy (1960) described the ossicular motion as a rotation of the malleus and incus about a fixed axis running from the anterior process of the malleus to the posterior incudal ligament. However, several authors have observed a complex combination of translational and rotational motion, and a shifting of the ossicular axis of rotation at high frequencies (Gundersen, 1976; Gyo et al., 1987; Decraemer & Khanna, 1994). In a review of the vibration modes in the middle ear, Decraemer & Khanna (1996) stated that, at frequencies below 1 kHz, the rotational motion is dominant in the cat and human middle ears, and the axis of rotation may be taken to be approximately fixed.

The incudomallear joint has been observed to be rigid at low frequencies (e.g., Guinan & Peake, 1967; Gundersen *et al.*, 1976). However, these studies also showed flexion in the joint at frequencies greater than 1 kHz.

Guinan & Peake (1967) and Decraemer *et al.* (1994) reported that the incudostapedial joint is non-rigid, the lenticular plate and stapes head behaving as articulating surfaces. In a finite-element study, Siah (2002) and Funnell *et al.* (2005) reported that the flexibility between the incus and the stapes may be mostly attributable to the pedicle, rather than to the incudostapedial joint. The effect of the pedicle on the ossicular mechanism had been ignored in previous studies.

The displacement of the stapes footplate has been the focus of numerous studies, because it has a major role in transferring energy to the inner ear. A piston-like motion of the footplate has been commonly assumed at frequencies below 1 kHz (e.g., Guinan and Peake, 1967). However, recent experimental measurements showed a complex

combination of piston-like and rocking motions at frequencies above 1 kHz (Heiland *et al.*, 1999; Decraemer *et al.*, 2000; Huber *et al.*, 2001).

3.4 Assumptions of the finite-element model

The aforementioned findings show that the mechanical behaviour of the middle ear is complex at high frequencies. For our finite-element model, some assumptions were based on the fact that the model is restricted to simulating low-frequency behaviour (i.e., below 1 kHz). Other assumptions are based on other findings discussed earlier in this chapter, or on the particular anatomy of the gerbil middle-ear in comparison with other species.

- The TM-malleus attachment is simply modelled as rigid. In other words, the ligament at the junction between the TM and the manubrium is not included in the model because the manubrium is tightly connected to the TM in the gerbil.
- The incudomallear joint is not modelled. The junction between the malleus and incus is simply a continuous connection of elements representing the mechanical properties of bone.
- For simplicity, the incudostapedial joint is not modelled. This is based on the assumption that the pedicle is more important than the incudostapedial joint. This will permit us to investigate the effects of the pedicle on the ossicular mechanism at low frequencies.
- The Young's moduli of the stapedial annular ligament, anterior mallear ligament and posterior incudal ligament are assumed to be the same in all directions (i.e., isotropic), and their value is based on the literature.

CHAPTER 4

THE FINITE-ELEMENT METHOD

4.1 Introduction

The use of mathematical models in general is very popular. Experiments are often very difficult to do and to understand. Models can describe the behaviour of a system to predict how the system could work. In particular, the finite-element method is a modelling technique that is very attractive in research involving a vast range of areas such as structures, electromagnetics, fluid dynamics, thermal analysis, transient dynamic response, non-linear response, etc. It can handle complex problems and systematically deal with non-linear systems, non-uniform materials, irregular geometries and irregular boundary conditions. For example, it can account for the shape and structure of an organism (i.e., its anatomy) as well as its functions (i.e., its physiology). However, experience and judgment are always needed in identifying the structures on scanned images (cf. Chapter 5), and in choosing element types and solution procedures. Powerful computers and reliable finite-element software are also essential.

In the finite-element method, a structure is broken down into a finite number of substructures, or elements, which form a mesh. Elements can have various shapes: rectangular, triangular, tetrahedral, etc. (Figure 4.1). Virtually anything can be divided into discrete elements, from a simple rectangular beam to a complex organ of the human body. In a mechano-acoustical system, each element is assigned a set of parameters for its material, thermal or acoustical properties, load and boundary conditions, thicknesses, etc. The response of an element to loading conditions is expressed in terms of displacements (or strains) and stresses. A set of equations is obtained for each element. Since the elements are connected to one another, an overall set of equations can be obtained by adding each elemental set of equations to a matrix describing the overall behaviour of the system (or model).

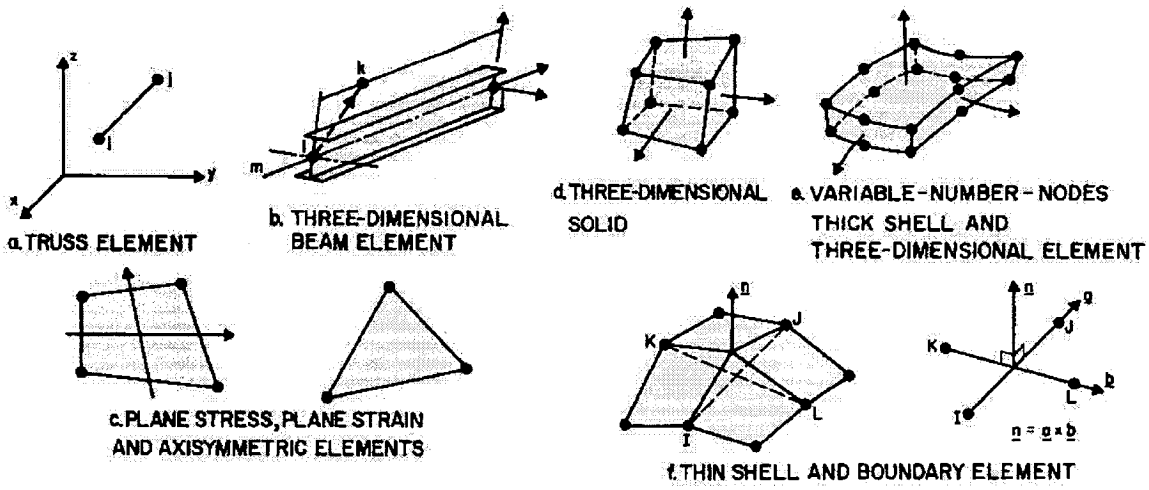

Figure 4.1: *Examples of element types that can constitute a mesh (source taken from http://audilab.bmed.mcgill.ca/~funnell/AudiLab/teach/fem/fem.html, and based on a figure from the SAP IV manual).*

The following section will provide a brief description of one of the most common methods used in finite-element analysis: the Ritz-Rayleigh method. There are other methods that can be used, such as the weighted-residual method or the direct differential formulation (Grandin, 1986). Section 4.3 will present the finite-element software used, followed by a discussion in Section 4.4 of the choice of elements in the finite-element model. Finally, Section 4.5 will discuss the need for a convergence analysis to determine the size of the elements required for sufficiently accurate results within a reasonable time frame.

4.2 Ritz-Rayleigh method

The basis of this approach is the principle of minimum potential energy, which states that "of all the geometrically possible configurations that a body can assume, the true one ... is identified by a minimum value for the total potential energy" (Grandin, 1986).

In the following sections, we shall use the convention that {} denotes a vector and [] denotes a matrix. Throughout the formulation of the Ritz-Raleigh method, the 'system'

being considered is a single element. The development of these sections is based on: Bathe (1982), Grandin (1986), Funnell (1989) and Zienkiewicz & Taylor (1989).

4.2.1 Basic concepts

For a linear elastic system in static equilibrium, the potential energy Π of one element is equal to the sum of the strain energy U (or internal energy) and force energy W (or external work done on the system):

$$\Pi = U + W \tag{1}$$

The strain energy can be defined as

$$U = \frac{1}{2}\int_{\Lambda}\{\varepsilon\}^T\{\sigma\}d\Lambda \tag{2}$$

where $\{\varepsilon\}$ and $\{\sigma\}$ are the strain and stress vectors respectively, and Λ is the element volume.

The force energy can be defined as

$$W = -\int_{\Lambda}\{r\}^T\{F\}d\Lambda - \int_{S}\{r\}^T\{T\}dS - \{w\}^T\{P\} \tag{3}$$

where $\{F\}$, $\{T\}$ and $\{P\}$ are the body-force, surface-traction and concentrated-force vectors, respectively; Λ and S are the element volume and surface, respectively; $\{r\}$ is the displacement vector at each node; and $\{w\}$ is the nodal displacement vector of the entire structure. Since work is being done on the system, a negative sign is placed in front of each force term.

Substituting equations (2) and (3) in (1), and knowing that the stress-strain relation is

$$\{\sigma\} = [E]\cdot\{\varepsilon\} \tag{4}$$

where $[E]$ is the matrix defining the material properties, the total potential energy of a single element can be reformulated as

$$\Pi = \frac{1}{2}\int_{\Lambda}\{\varepsilon\}^T[E]\{\varepsilon\}d\Lambda - \int_{\Lambda}\{r\}^T\{F\}d\Lambda - \int_{S}\{r\}^T\{T\}dS - \{w\}^T\{P\} \qquad (5)$$

4.2.2 Local coordinate system

To simplify the equation, it is preferable to convert the global displacement vectors to local displacement vectors:

$$[H]\cdot\{u\} = \{r\} \qquad (6)$$

where $[H]$ is the displacement interpolation matrix, and $\{u\}$ is the local displacement vector for each element. The corresponding local element strains can be expressed as:

$$\{\varepsilon\} = [B]\cdot\{u\} \qquad (7)$$

where $[B]$ is the strain-displacement matrix, obtained by differentiating $[H]$.

Substituting (7) into the strain-energy term of (5), we obtain an expression for U for each element in terms of local coordinates:

$$U = \frac{1}{2}\int_{\Lambda}\{\varepsilon\}^T[E]\{\varepsilon\}d\Lambda = \frac{1}{2}\int_{\Lambda}\{u\}^T[B]^T[E][B]\{u\}d\Lambda \qquad (8)$$

Similarly, the external force energy W for each element – in terms of local coordinates – can be obtained by substituting (6) and (7) into (3):

$$W = -\int_{\Lambda} \{r\}^T \{F\} dV - \int_{S} \{r\}^T \{T\} dS - \{w\}^T \{P\}$$
$$= -\int_{\Lambda} \{u\}^T [H]^T \{F\} d\Lambda - \int_{S} \{u\}^T [H]^T \{T\} dS - \{w\}^T \{P\} \quad (9)$$

4.2.3 Global finite-element equilibrium equations

Summing up the potential energies of each element, we can obtain the overall potential energy of the system:

$$\Pi = \frac{1}{2} \sum_{i=1}^{m} \{u\}_i^T [k]_i \{u\}_i - \sum_{i=1}^{m} \{u\}_i^T \cdot \left(\int_{\Lambda_i} [H]_i^T \{F\}_i d\Lambda + \int_{S_i} [H]_i^T \{T\}_i dS \right) - \{w\}^T \{P\} \quad (10)$$

where

$$[k]_i = \int_{\Lambda} [B]^T [E]_i [B] d\Lambda \quad (11)$$

is the element stiffness matrix for each element.

Equation (10) can be simplified to

$$\Pi = \frac{1}{2} \{w\}^T [K] \{w\} - \{w\}^T \{R\} \quad (12)$$

where $\{R\} = \left[\sum \left(\int_{\Lambda_i} [H]_i^T \{F\}_i d\Lambda + \int_{S_i} [H]_i^T \{T\}_i dS \right) + \{P\} \right]$,

$\{w\} = \Sigma\{u\}$, and

$[K] = \Sigma\{k\}$.

According to the principle of minimal potential energy, we can find the stable equilibrium state by differentiating equation (12) with respect to each nodal displacement variable

$\{w\}$, leading to

$$[K]\{w\} = \{R\} \tag{13}$$

Equation (13) is applicable only to static systems. In the case of mechano-acoustical systems, low-frequency analysis can be assumed to be static, therefore neglecting damping and inertia. For dynamic analysis, damping and inertial effects must be accounted for, and the overall finite-element equilibrium equation becomes

$$[M]\{w\}'' + [C]\{w\}' + [K]\{w\} = \{R\} \tag{14}$$

where $[M]$ and $[C]$ are the inertia and damping matrices, respectively, and $\{w\}'$ and $\{w\}''$ are the first and second time derivatives of the displacement vector $\{w\}$.

4.3 Finite-element software

There are numerous finite-element software packages available. Some commercial packages on the market today include ANSYS, ABAQUS and NASTRAN. There is also free finite-element software with source code downloadable from the Internet, including TOCHNOG, Modulef, Cast3m and CalculiX, among others. Pre-processors are available to help the user in the segmentation and mesh-generating processes, as well as post-processors to examine results.

In this thesis, the finite-element software used is SAP IV. The program is written for the static and dynamic response of linear three-dimensional systems. SAP IV is used simply because we are used to it in our lab, and we have pre- and post-processors that function well with it. SAP was originally developed at UC Berkeley, and its source code was freely distributed. It has been modified over the years by Dr. WRJ Funnell, including the addition of tetrahedral elements and changes to the handling of shell elements. A complete list of the changes made is available at http://audilab.bmed.mcgill.ca/~funnell/AudiLab/sw/sap.html.

4.4 Choice of elements

The choice of element type is crucial for the accuracy of the solution. For example, the thickness of the eardrum is much smaller than its other dimensions and the stresses in that direction can be assumed to be insignificant. Therefore, a two-dimensional type of element is appropriate, such as a triangular shell element. The specific SAP element used is a quadrilateral element (with six degrees of freedom per node), from which the fourth node can be omitted to create a triangular element. Ideally, all solid structures should be modelled with volume elements. However, for reasons discussed in Chapter 6, the use of volume elements is not always necessary. When volume elements are necessary – for example, for the pedicle and ligaments, in which mechanical behaviours such as bending (for the former) and twisting (for the latter) require elements that yield accurate results – the SAP element used is a three-dimensional tetrahedral element (with six degrees of freedom per node). The mesh specifications for each part of our model will be described in detail in Chapter 6.

4.5 Convergence

In general, as the resolution of a mesh is increased, the accuracy of a finite-element analysis increases, but so too does the computation time. Thus, the problem to be addressed is that of how many elements are needed for sufficiently accurate results within a reasonable computation time. A trade-off is required between computation time and accuracy. The convergence analysis will be discussed in more detail in Chapter 7.

To ensure adequate convergence, the elements should be *complete* and *compatible* (Bathe, 1982). The *completeness* of an element can be described by the ability to define all rigid-body displacements and constant-strain states. Rigid-body displacements are displacements of the element that do not develop stress (i.e., pure translation or rotation). A constant-strain state of an element can be understood if we imagine that "more and more elements are used in the mesh of a structure. Then in the limit as each element approaches a very small size, the strain in each element approaches a constant value, and any complex variation of strain within the structure can be approximated" (Bathe, 1982).

Compatibility implies that displacements must be continuous within and between elements. Therefore, no gaps or overlaps must be present in the assemblage of the elements.

In general, the *completeness* condition can be satisfied. On the other hand, considering complex problems in which elements of different sizes and shapes must be used to represent different regions of a structure, *compatibility* requirements may be difficult to maintain. However, experience shows that adequate results are often obtained even if the *compatibility* condition is violated.

CHAPTER 5

METHODS

5.1 Introduction

The tools and techniques used in the development of our finite-element model will be discussed in detail in this chapter. Section 5.2 will provide a brief summary of the imaging techniques (magnetic resonance microscopy, X-ray micro-computed tomography, histology and moiré topography) used to acquire data. Section 5.3 will present details of the data themselves. Section 5.4 will present a detailed description of the image-segmentation tools and techniques used. Finally, Section 5.5 will discuss the details of the finite-element mesh generator.

5.2 Imaging technology

5.2.1 Magnetic resonance imaging

Magnetic resonance imaging (MRI) is derived from the study of nuclear magnetic resonance (NMR). The original name was 'nuclear magnetic resonance imaging' (NMRI), but the word 'nuclear' was dropped to avoid negative connotations. NMR was first described in 1946 by Felix Bloch and Edward Mills Purcell, who shared the Nobel Prize in Physics in 1952. NMR is a physical phenomenon based upon the magnetic properties of sub-atomic particles. It exploits the response of the atom's nucleus in magnetic and electromagnetic fields in order to obtain physical, chemical and structural information. Several publications deal with the principles of NMR and MRI (e.g., Curry et al., 1990; Zhou *et al.*, 1995; Brown *et al.*, 1999).

MRI is a 3-dimensional scanning method of creating images for a wide variety of purposes; in particular, it can display normal and pathological features of living tissues. It was discovered in the 1970's by Paul Lauterbur and Sir Peter Mansfield, who shared the Nobel Prize in Medicine in 2003. MRI scanners rely upon the relaxation properties of hydrogen nuclei in water. The tissue to be imaged is placed in a powerful, uniform

external magnetic field which aligns the hydrogen atoms (Figure 5.1). The atoms are then perturbed using an electromagnetic field and assume a temporary non-aligned high-energy state. As the high-energy nuclei relax and realign, they emit energy which is recorded to provide information about their environment. The information is subsequently processed by a computer to obtain the desired images. One of the advantages of MRI is the use of non-ionizing radiation, which is harmless to patients, whereas x-rays are ionizing radiation which increases the probability of malignant tumours.

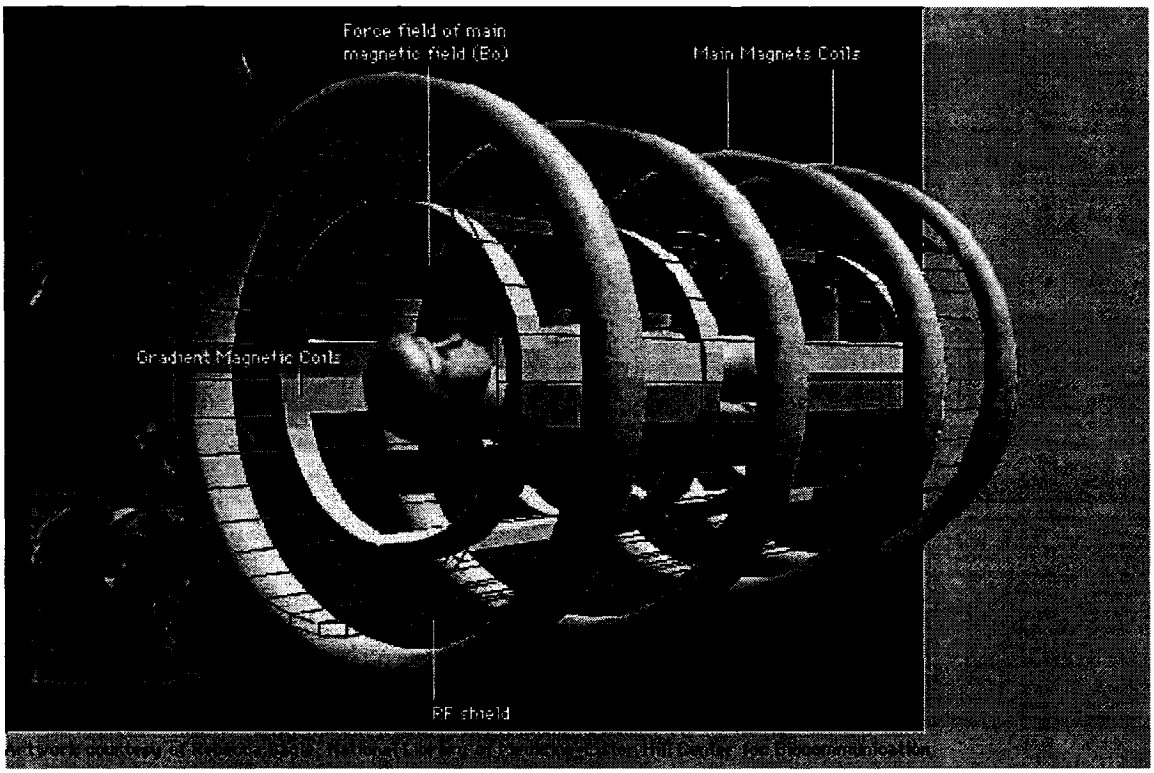

Figure 5.1: *Diagram showing the basic principles of MRI (http://science.howstuffworks.com/mri)*

Magnetic resonance microscopy (MRM) is basically MRI at a microscopic level with smaller specimen size and finer resolution (Zhou *et al.*, 1995).

5.2.2 X-ray computed tomography

Computed tomography (CT) was invented in 1968 by the British engineer Godfrey

Hounsfield of EMI Central Research Laboratories. He shared the Nobel Prize in medicine in 1979 with Allan McLeod Cormack of Tufts University who had independently published a reconstruction algorithm in 1963. CT is a medical imaging method in which digital processing is used to create two- or three-dimensional images of an object. X-ray CT uses a series of two-dimensional X-ray images, taken from different angles, to generate a three-dimensional image of the internal structures of an object (e.g., Kak & Slaney, 2001). CT has been used with several modalities other than X-rays, including MRI and positron emission tomography (PET). It has become a standard technique in the field of diagnostic medical imaging, including middle-ear diagnosis (e.g., Swartz, 1983; Fuse *et al.*, 1992).

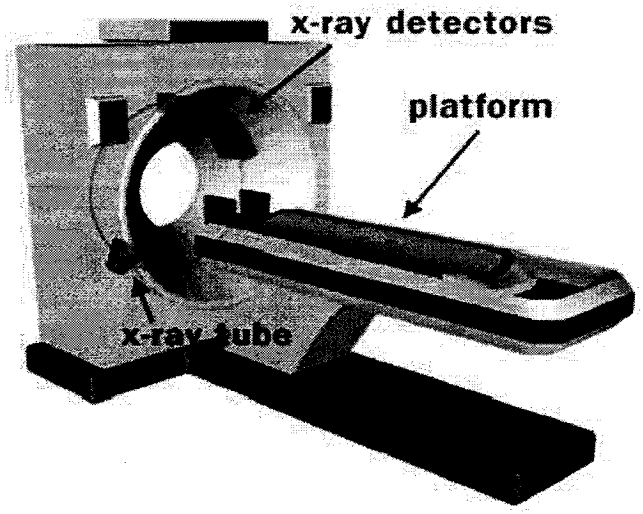

Figure 5.2: *Diagram showing the basic principle of a clinical CT machine. The X-ray tube and detectors are mounted on a ring which rotates about the platform.*
(http://science.howstuffworks.com/cat-scan)

In an X-ray CT machine, an object is placed between an X-ray source and an array of sensors (Figure 5.2). The source emits a beam. The X-ray beam is absorbed to different extents depending on the object composition. Each sensor detects an intensity value that corresponds to an integration of the absorption along the path of the beam. Depending on

the source-sensor arrangement of the specific X-ray generation used, a projection is obtained as a collection of such intensity values from all the sensors. The X-ray tube rotates 180° incrementally giving a matrix of these projections, which is used by different algorithms to generate a cross-sectional image of radiographic density. A translation along the object gives a set of slices that form the complete 3-D representation of the object.

X-ray micro-CT is basically X-ray CT at a microscopic level. The sample is placed on a horizontal platform. This sample holder system is available in two types:

- The platform is stationary, and the tube rotates around it. This is commonly used for in-vivo animal scans and other situations where the sample should remain unmoving, but is very expensive.
- The platform rotates, and the tube is stable. It is much cheaper to build, since moving the platform requires fewer components than moving the tube containing the X-ray detectors and the X-ray source.

X-ray micro-CT is available from a handful of manufacturers worldwide including Scanco Medical (Switzerland), Bio-Imaging Research (USA), Stratec (Germany), CTI Concorde (USA), SkyScan (Belgium), Toshiba IT & Control Systems (Japan) and GE Healthcare (UK). The GE scanner was originally developed in Canada by EVS Ltd., which was then acquired by GE Healthcare.

5.2.3 Histology

Histology is the anatomical study of microscopic structures of tissues sectioned in thin slices (Ham & Cormack, 1979). Usually, the examination starts with the removal of the specimen by surgery, biopsy or autopsy, although in small enough specimens this is not necessary (e.g., embryos). The tissue is then fixed in a fixative (such as formalin) which stabilizes the tissue and prevents it from decaying. Next, the tissue may be decalcified – the sample is immersed in a decalcifying solution (such as ethanol or formic acid) for several hours. Afterwards, the sample is embedded in a sliceable material (e.g., paraffin wax) which turns soft moist tissues into a hard block, without any chemical transformation of the sample, and can preserve its morphology for years. The point of

embedding is at least as much to permit slicing as it is to permit storage. The sample is sectioned into slices of thicknesses ranging from about 100 nm to about 20 μm, using a microtome – a mechanical instrument used to cut biological specimens into very thin segments for microscopic examination. Slices are then mounted on glass plates and dried, appearing almost completely transparent. Because of its transparency, a slice has to be stained with one or more pigments. For example, two commonly used pigments are hematoxylin – a natural stain which dyes acidic components of a tissue blue/purple – and eosin – a synthetic stain which dyes basic components of a tissue pink/red. Hematoxylin and eosin are commonly used together to simultaneously highlight both types of tissue. Finally, the slices are covered with a glass slide for protection.

5.2.4 Moiré topography

Phase-shift moiré topography is a non-contacting optical method that can measure the precise 3-D shape of an object (Dirckx & Decramer, 1989, 1990). In brief, a light is shone through a grid of straight lines onto the eardrum's curved surface, causing curved shadows. Looking at the curved shadows through the grid produces moiré interference patterns which define the shape of the eardrum's surface. These patterns are combined to form an image in which the grey level of each pixel is proportional to the z coordinate.

5.3 Image data

5.3.1 MRM and micro-CT data

The gerbil middle-ear structures were segmented from MRM and micro-CT data sets. Figure 5.3 shows an example of a slice from each data set.

For the MRM data, the middle-ear structures were prepared by Drs. M. Henson & O.W. Henson, Jr., of the University of North Carolina at Chapel Hill, and then scanned at the Duke University Center for In Vivo Microscopy to obtain a dataset (number 15516). The set consists of 168 horizontal sections of 256 by 256 pixels each, with a voxel size of about 45 μm. It can be downloaded from the Hensons' Web site at:
http://cbaweb2.med.unc.edu/henson_mrm/pages/Scans_Rodents.html

The X-ray micro-CT data were generated using a SkyScan 1072 scanner, and were made available by Dr. W.F. Decraemer of the University of Antwerp, Belgium. The set consists of 601 sections of 1024 by 1024 pixels each, with a voxel size of about 5.5 μm.

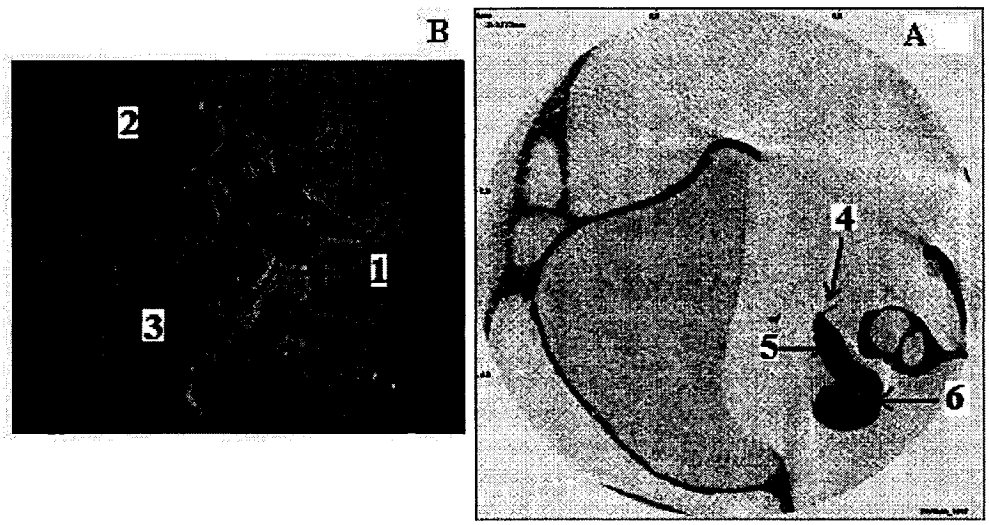

Figure 5.3: *Gerbil middle-ear cross-sectional images. A: Slice number 80 from MRM set 15516 showing the stapes (1), manubrium (2) and TM (3). B: Slice number 590 from micro-CT data set showing, among other things, the pedicle of the incus (4), the incus long process (5) and the body of the incus (6).*

The SkyScan images were scanned at a much higher resolution than the MRM images. The gerbil model was completed using the MRM data set, and then the X-ray data set was used to improve it.

- The anterior mallear ligament, posterior incudal ligament, and pedicle of the incus were easier to distinguish in the micro-CT images than in the MRM images. They were remodeled on the MRM images with visual reference to the micro-CT images.
- The stapes footplate and annular ligament were hardly distinguishable in the MRM images. They were re-segmented from the micro-CT images, after which the stapes footplate and annular ligament models were merged with the MRM model. This will be further discussed in Chapter 6.

The original tympanic membrane (from moiré) and ossicles were not modified based on the micro-CT data, because the MRM images provided sufficient resolution and contrast.

5.3.2 Histological data

Histological data were not directly used to create the model for the following reasons:

- When sectioning with a microtome (cf. Section 5.2.3), some of the structures in the sample are sometimes shifted from their natural positions and the slices are often stretched or torn.
- Successive slices would need to be aligned, which is difficult.

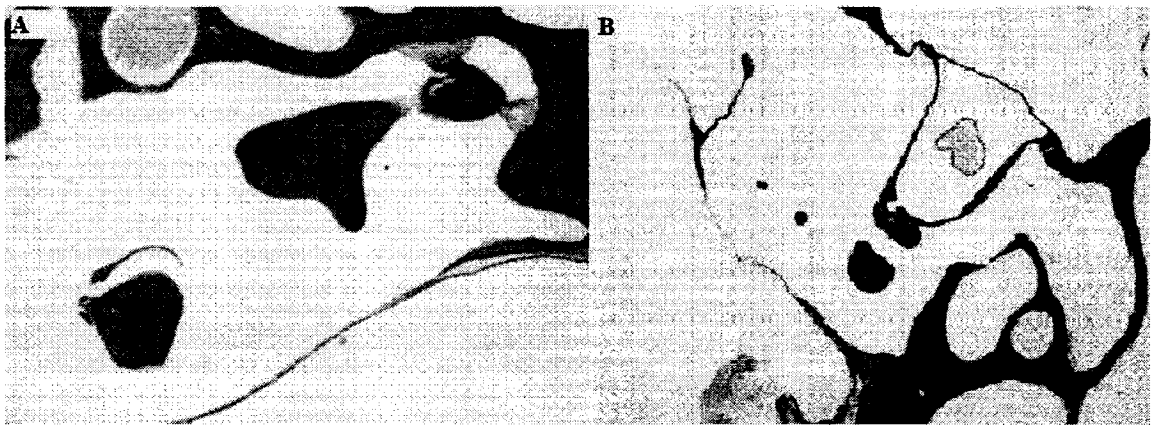

Figure 5.4: *Examples of histological sections, stained with toluidene blue, of the posterior incudal ligament (**A**) and the incudostapedial joint (**B**).*

The MRM and micro-CT data were supplemented by the use of histological serial sections (courtesy of Dr. Magnus von Unge of the Karolinska Institute in Stockholm, Sweden) to clarify certain details, because the resolution and contrast of histological sections is very good. For example, histology was very helpful in defining the exact points of origin and insertions of ligaments, and the complex structures of joints. Figure 5.4 shows details of the posterior incudal ligament and of the incudostapedial joint.

5.3.3 Moiré data

The eardrum model used here was generated using images from phase-shift moiré

topography. These images were produced in Dr. WF Decraemer's lab in Antwerp, Belgium. The model (Figure 5.5) is the same one used by Funnell (1999 & 2000). By applying static pressure during the shape measurement, one can accurately determine the boundaries of the eardrum (Funnell *et al.*, 2000).

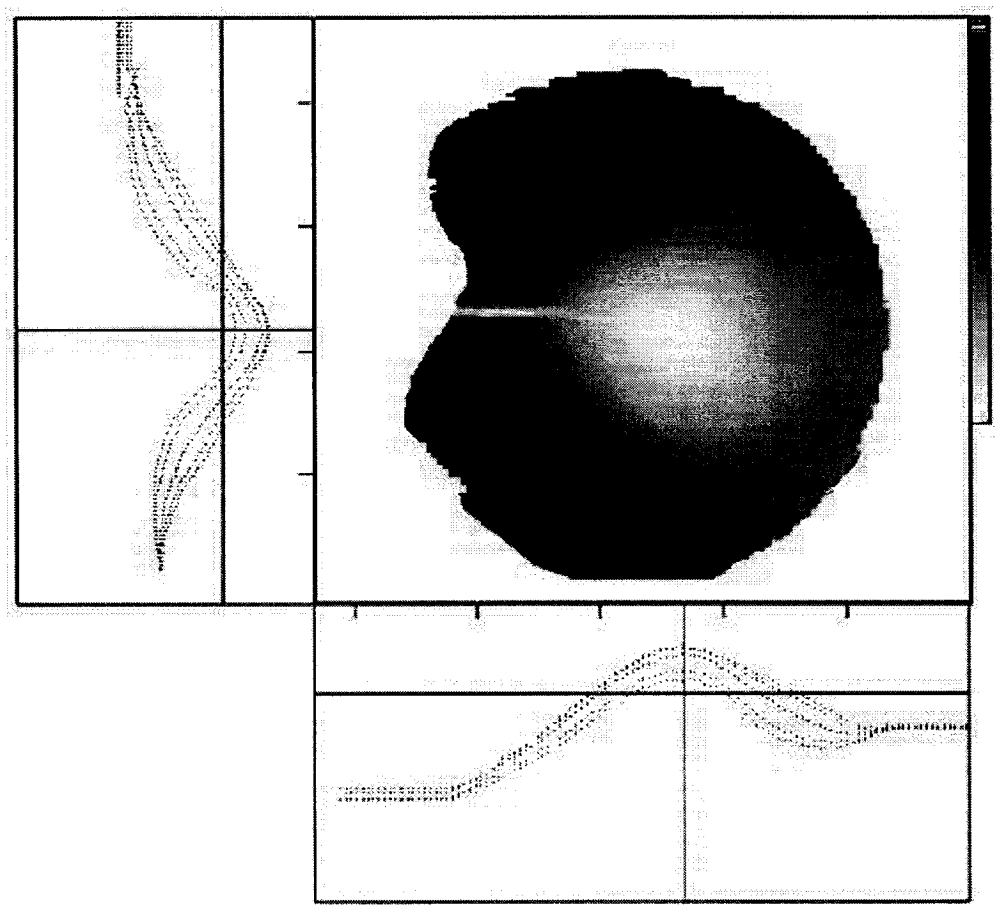

Figure 5.5: *Moiré image of a gerbil eardrum (Funnell et al., 2000). The profile at the left is along a line perpendicular to the manubrium, in the region of the umbo (as indicated by the vertical line in the bottom box). The profile on the bottom is along a line posterior to the manubrium (as indicated by the horizontal line in the left-hand box) and roughly parallel to it. The contours show both the resting shape and the shapes resulting from the application of two positive and two negative pressures.*

5.4 Segmentation

5.4.1 Introduction

Segmentation can be seen as a computer-vision problem (Stytz et al., 1991; Ayache, 1995). The basic goal is to locate and extract objects of interest. There is a variety of different segmentation techniques which can be divided into two groups: low-level and high-level methods. Low-level methods, such as thresholding, clustering and region-growing, are fast and simple, but usually overlook important information such as small details in complex regions (e.g., Bizais et al., 1995). High-level methods include, amongst others, active contours (Kass et al., 1986; Caselles, 1995), dynamic contours (Lobregt & Viergever, 1995) and geometrically deformable models (Miller, 1990). They may generate better results, but they are computationally expensive.

The methods used in our laboratory (including an active-contour technique), and the software, will be discussed in the following sections.

5.4.2 Snake algorithm

Snakes, or active contours, were introduced by Kass et al. (1987) and have been improved over the years (e.g., Yezzi et al., 1997; Xu & Prince, 1997, 1998). The snake algorithm used in our lab was developed by Lobregt & Viergever (1995), re-implemented locally by Hamelin *et al.* (1999), then modified and enhanced by Hatamzadeh-Tabrizi (2003). The basic principle consists of using curves which are deformed by internal and external 'forces'. The external forces drive the model close to the image features, whereas the internal ones serve to preserve the regularity and smoothness of the line.

5.4.3 Fie

A home-grown program was developed by Dr. WRJ Funnell for segmenting images. Fie (Fabrication d'imagerie extraordinaire) can perform various image-editing and related tasks (e.g., Herrera et al., 1991, 1997). It is written in Fortran, and is compatible with GNU/Linux and Microsoft Windows. Images in TIFF, JPEG or raw formats are read into Fie, which outputs a text file (.tr3) containing the complete segmentation information that is later used for mesh generation. Fie is freely downloadable from

http://audilab.bmed.mcgill.ca/~funnell/AudiLab/sw/fie.html. What follows is a discussion of some issues related to the use of Fie.

A palette can be applied to grey-level images. It is used to help to distinguish any boundary in general (such as between bone and soft tissue). Grey-level values under a first threshold are set to shades of blue, and those over a second threshold are set to shades of yellow. This helps to guide the snake – the grey levels are adjusted up or down before being passed to the snake algorithm. The sample image shown in Figure 5.6 has the thresholds set to differentiate among bone (shown in yellow), soft tissue , and air (shown in blue).

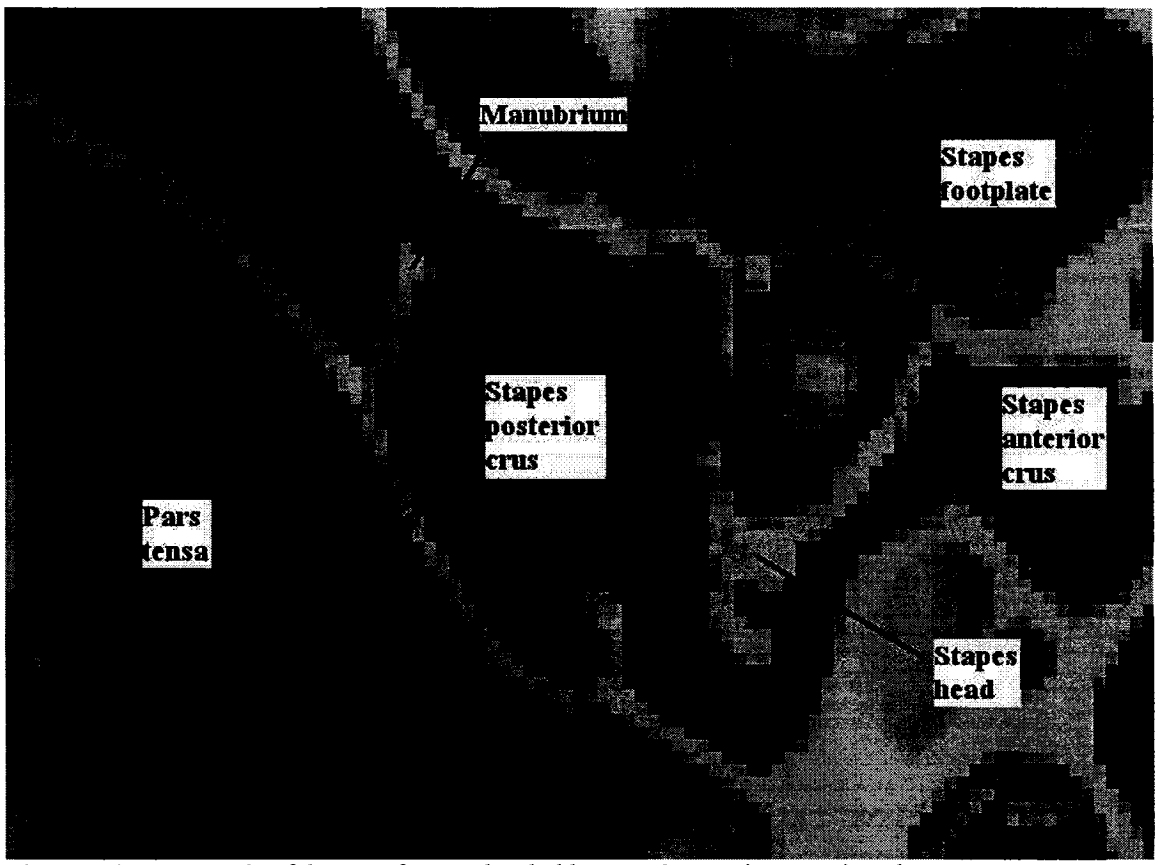

Figure 5.6: An example of the use of a two-threshold grey palette, using our Fie software.

A curve-smoothing function (which smoothes splines by an interpolation algorithm) is available if required to adjust the final shape of the curve.

One must identify the lines with an adequate naming system. Conventions are needed so that any user will be able to locate the different lines with relative ease, and to facilitate subsequent handling of related lines. The system we use is as follows. The first part of the name is simply the name (or an abbreviation of the name) of the structure where the line is located (incus, malleus, manubrium, eardrum, etc.). Then, abbreviations of the specific locations are added, such as "med" for medial, "proc" for process, and so on. Finally, the number of the slice in which the line first appears is added at the end of the name.

5.4.4 Open and closed lines

There are two different types of lines in the segmentation process. Closed lines are used to represent closed 2-D regions which are not connected to any other structure. Open lines are used when a line needs to be joined to another line. They are also used for thin structures, such as the eardrum, since the latter represents a single layer. One major advantage of open lines is their ability to define complex boundaries. Figure 5.7 shows examples of open and closed lines.

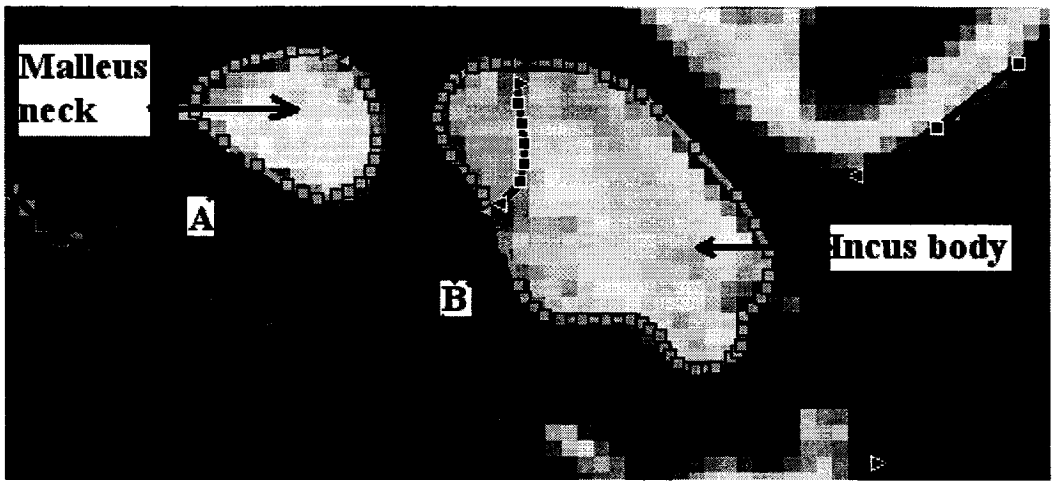

Figure 5.7: Examples of closed (**A**) and open (**B**) lines segmented in Fie. The boundary of the malleus neck is segmented with a closed line. Open lines were used for the incus body and the pars flaccida (in blue), pars tensa (in green) and the incus body. The two open lines that define the incus body are connected to each other at both ends. The anterior end of the pars flaccida (in blue) is connected to the posterior end of the pars tensa (green).

5.4.5 Tr3 text file

As mentioned before, Fie generates a .tr3 output file in plain-text format. This output file contains information about all the properties of the lines: scaling, coordinates, connectivity, resolution, color, thickness, material properties, etc. In addition, comments may be added to track the history of changes. The following subsections will describe the major components of the .tr3 file.

5.4.5.1 Line attributes

A detailed description of the syntax for qualifiers is available at http://audilab.bmed.mcgill.ca/~funnell/AudiLab/sw/fie.html. A typical line syntax is shown in this example:

Example 1:

Pars_tensa_ant_53: -c Green -xyr 100 -zr 5 -tr 0.5 -mat 1 -th 5.u -b CSF -p 1. ;TM

The line name is '*Pars_tensa_ant_53*'. It represents a section of the anterior portion of the pars tensa. The line first appears in slice 53. During mesh generation, it will be triangulated with a resolution of 100 elements per diameter (*-xyr 100*). This means that the element sizes will be approximately 1/100 of an estimated overall diameter of the entire model. The *z* resolution is 5, which means that every fifth slice will be used during triangulation. The line is coloured green (*-c Green*) and it will have a transparency of 0.5 (*-tr 0.5*). This means that, in a 3-D image viewer, the structure will appear green and semi-transparent; in this case, the line will also be displayed as green within Fie, although a different colour can be specified. The line has material properties of type 1 (*-mat 1*), and a thickness of 5 μm (*-th 5.u*). It is clamped at its start node and along its entire first slice (*-b CSF*). A pressure of 1 Pa (*-p 1*) is applied to its elements. A description text is added at the end of the syntax, preceded by a semi-column (';').

5.4.5.2 Line connectivity

To ensure the continuity of a structure composed of multiple lines, connectivity options are essential. They include 'start-at' and/or 'finish-at' qualifiers, as well as the JOIN

command. Example 2 shows an example of the syntax for the 'start-at' and 'finish-at' qualifiers:

Example 2:

Malleus_head_med_44: -c Yellow -xyr 100 -mat 2 -s f Malleus_head_lat_44 -f s Malleus_ant_proc_med_44 Malleus head

The open line '*Malleus_head_med_44*' represents the medial side of the malleus head, and is colored yellow. It has material properties of type 2. When triangulating, it will be divided with a resolution of 100 elements per diameter. This line starts at the last node of a lateral line, '*Malleus_head_lat_44*', and finishes at the first node of an anterior-process line, '*Malleus_ant_proc_med_44*'.

The 'start-at' and/or 'finish-at' commands may only be used to link lines within the same slice. On the other hand, the JOIN command links lines from different slices. A number of lines from one slice can be connected to other lines from another slice in just one JOIN command. Example 3 shows a typical case:

Example 3

Incus_head6: Incus_head_med_60 -Incus_head_lat_60 Incus_head_dum_60 to Incus_long_med_proc_69 -Incus_long_lat_proc_69

The join named '*Incus_head6*' links the last slice in which the lines '*Incus_head_med_60*', '*Incus_head_lat_60*' and '*Incus_head_dum_60*' appear (in this case it is slice 66) to the first slice in which the lines '*Incus_long_med_proc_69*' and '*Incus_long_lat_proc_69*' appear (in this case, it is slice 69), while taking into account the *z* resolution of each. The lines are listed in the order in which they are connected to one another. A minus ('-') sign before a name means that the line is to be traversed backwards when being linked with other lines. This example also shows that the JOIN command can be used to join lines between two slices that are not necessarily one after the other. In this case, the last slice in which the lines '*Incus_head_med_60*', '*Incus_head_lat_60*' and '*Incus_head_dum_60*' appear is slice 66, and the first slice in

which the lines '*Incus_long_med_proc_69*' and '*Incus_long_lat_proc_69*' appear is slice 69.

The JOIN function can also be used to link the first and/or last nodes between lines. The symbol '>' or '<' after a line name denotes that only the first or last node of that line is used, respectively, as shown in example 5:

Example 5

TM1: Pars_tensa_ant_53< Pars_flaccida_53> to Pars_tensa_ant_73< Pars_flaccida_73>

A first line is generated between the last node of line '*Pars_tensa_ant_53*' and the first node of line '*Pars_flaccida_73*', and a second line is generated between the last node of '*Pars_tensa_ant_73*' and the first node of '*Pars_flaccida_73*'. The join named '*TM1*' links those two lines.

5.4.5.3 Caps for closing structures

If a closed contour is not connected to any other contours in the slices before or after, then an opening will appear. Figure 5.8-A shows the open ends of the incus long process and of the head of the stapes. There are two ways using Fie to close such openings. A single node can be added in the slice after. This will create a conical closing as shown for the end of the incus long process in Figure 5.8-B. Alternatively, a CAP command can be used to 'cap' the structure, thereby creating a flat surface, as shown for the end of the head of the stapes in Figure 5.8-B. In order to use the CAP option, the line (or lines) to be capped must form a closed loop.

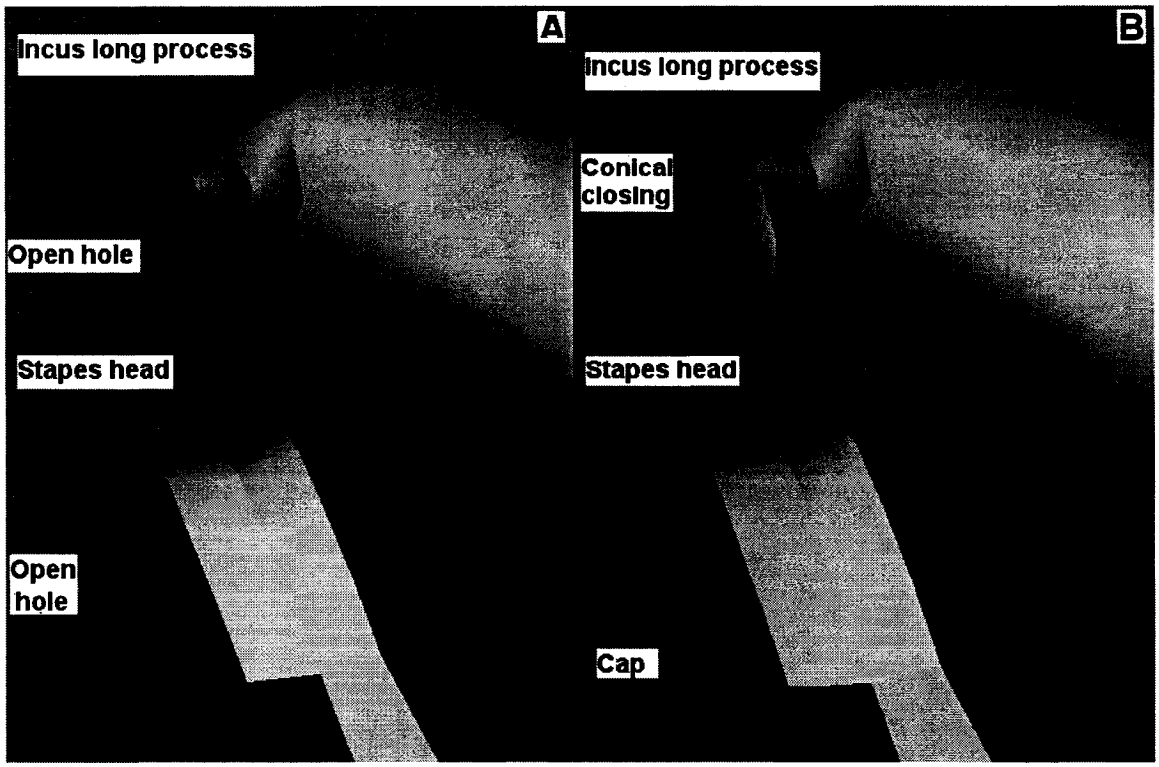

Figure 5.8: *Examples of a conical closing of the incus long process, and a CAP closing of the head of the stapes.*

Example 6

Lig_ann: HEAD Lig_ann_med_75 Lig_ann_ant_75 Lig_ann_lat_75 Lig_ann_post_75

The cap '*Lig_ann*' represents the closing of the opening formed by the lines '*Lig_ann_med_75*', '*Lig_ann_ant_75*', '*Lig_ann_lat_75*' and '*Lig_ann_post_75*'. Since the line names are preceded by the word HEAD, the first slice in which those lines appear will be capped. If TAIL were used instead, the last slice in which those same lines appear would be capped.

5.4.5.4 Subsets

Lines can be divided into subsets. Subsets are useful when only certain structures need to be included in a 3-D model. The subset command is also a fast and simple way to modify line attributes before running simulations, and to have different attributes defined

simultaneously in different subsets.

Example 7

TM
**: -off*
Pars: -on -xyr 30 -zr 2*
Pars_flaccida: -th 15.u -mat 6*
Pars_tensa: -th 5.u -mat 7*
END of subset

Notice the use of '*'. The symbol '*' after a character string means that all the line names starting with that word are selected. If there are no characters before '*', then all of the lines are incorporated. In the above example, the subset name is 'TM', and it starts by turning off all the lines (**: -off*). Then, all lines starting with the letters 'Pars' are selected (*Pars*: -on*), with the specified attributes (*-xyr 30 -zr 2*). The lines starting with the strings 'Pars_flaccida' and 'Pars_tensa' are then defined with different values for the thickness (15 and 5 μm) and material properties (types 6 and 7). These new attributes override previous definitions.

5.4.5.5 Material properties

The MATERIALS section contains a list of the material types used in the model definitions. All materials are assumed to be linear and isotropic.

Example 8

2 200.M 0.3 1500. ;bone (Ossicles)

In this example, the material type is defined by the first column (in this case, the type is 2). The Young's modulus for this material type is equal to 200 MPa, with a Poisson's ratio of 0.3 and a density of 1500 kg/m3. The description of the material type is defined as '*bone (Ossicles)*'.

Since Fod (a locally developed post-processor) displays separate displacement results for

each material type, important structures with the same material properties were sometimes given different material types. A list of the material types used in our model definition is included in Appendix A.

5.5 Mesh generation

Before running simulations with the finite-element model, a mesh must be generated to represent the structures of the model. There are many different methods available for mesh generation.

The Tr3 program used in this work was created in our lab by Dr. WRJ Funnell to generate surface meshes. It triangulates 3-D surfaces between serial-sections, creating shell elements that consist of triangles with 3 nodes. A .tr3 text file (the file created by Fie, as discussed above) is fed into the Tr3 program, which outputs a .wrl file and a .sap file. The .wrl file is a VRML (Virtual Reality Modeling Language) file for visualization. VRML is a standard file format for distributing 3D interactive models on the web (http://www.web3D.org). The .sap file contains information about the nodes and elements of the mesh (i.e., coordinates, material properties, loads and boundary conditions). This file is fed into the Sap IV finite-element processor mentioned in section 4.3. Tr3 is implemented in Fortran and, like Fie, is compatible with GNU/Linux and Microsoft Windows 95/98/NT/2000/XP. It can be freely downloaded from http://audilab.bmed.mcgill.ca/~funnell/AudiLab/sw/tr3.html.

The eardrum is modeled with shell (or surface) elements, as generated by Tr3. The rest of the model should ideally be modelled with volume elements. Volume elements – consisting of tetrahedral elements with 4 nodes – would characterize the volumes of the structures (both the boundaries and the interiors). A larger number of nodes would be needed to fill the interiors of the ossicles. This would slow down the analysis. The decision to model the large structures (the ossicles) as shell elements was taken in order to simplify and accelerate the triangulation and simulation processes. This is an acceptable decision, since the ossicles are assumed to behave as rigid structures, at least at low frequencies. The pedicle and ligaments, however, cannot be assumed to be rigid.

They were therefore modeled with volume elements as discussed in Section 5.5.2 below.

5.5.1 Surface meshes

Figure 5.9 shows an example of the meshing of a section of the pars tensa across two different slices. Side and bottom views are shown on the right-hand side and at the bottom of the figure, respectively. The black line is the line in one slice, and the red line is the same line in the next slice. The meshing is represented by the green lines between the black and red lines.

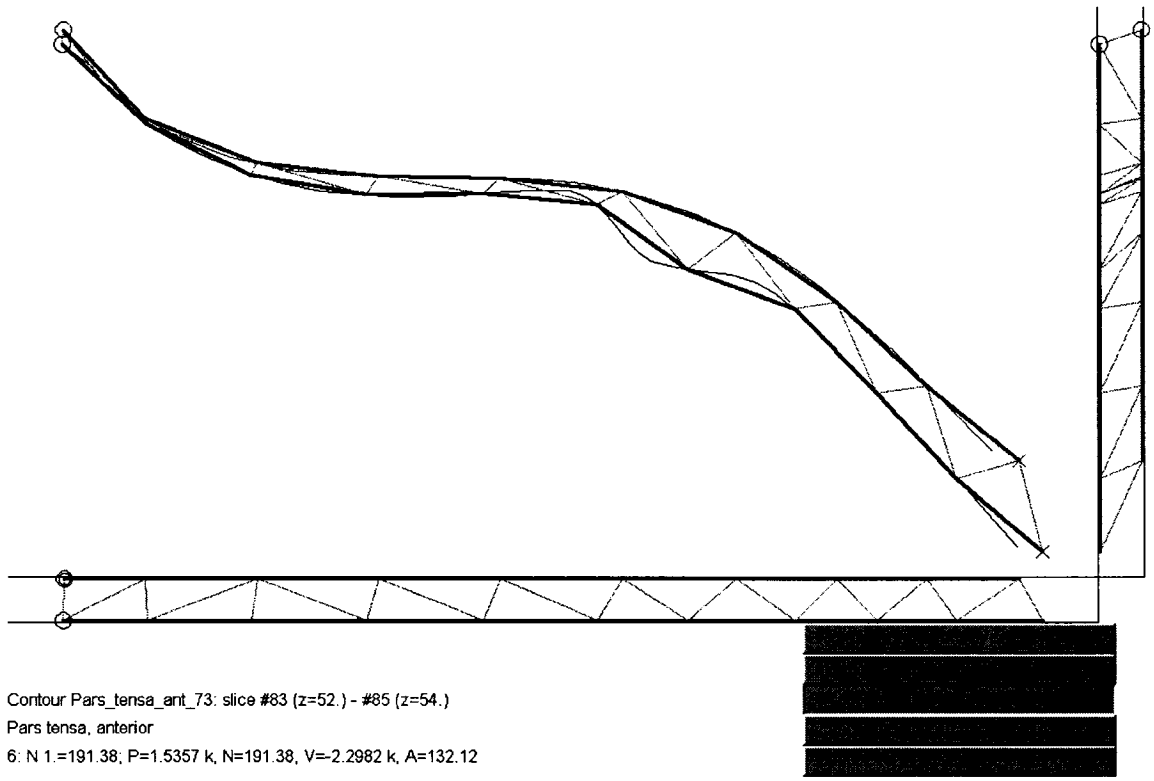

Figure 5.9: *Example of a surface triangulation between two slices using Tr3.*

The thicknesses of the shell elements for the ossicles were based on direct measurement from the MRM slices. In a slice that best showed the average shape of the solid structure, the approximate diameter was measured, and contours of that structure were given a thickness equal to about one third of the structure's diameter. In regions within a structure where the thickness decreases considerably, different thicknesses were assigned. One example of such a case is the malleus, where the anterior process and the body have

different thicknesses (the latter being much thicker).

Specific values for the thicknesses are given in Chapter 6.

5.5.2 Volume meshes

The 3-D finite-element mesh-generation software used here is Gmsh. Its authors are Christophe Geuzaine and Jean-François Remacle (http://www.geuz.org/gmsh/). Gmsh works with definitions of points, lines, surfaces and volumes, based on the geometrical data of the model. An algorithm based on Delaunay triangulation (Ruppert, 1995) is implemented in Gmsh. The 3-D mesh-generation process can be summarized as follows:

- Surface triangular mesh definition of a model (.sap file) is imported into a file-format converter (developed by Hengjin Liu, a fellow lab student) and converted to a .geo file.
- Gmsh (version 1.60, modified by Hengjin Liu) generates a volumetric tetrahedron mesh based on the surface triangular mesh definitions.
- Boundary conditions, loads and material properties of the model are extracted from the original model and, by a program developed by Hengjin Liu, combined with the volumetric tetrahedron mesh to form a new .sap file.

As mentioned previously, only the pedicle and the ligaments were modeled using volume elements.

5.5.3 Mesh Resolution

The finite-element process depends in part on how fine a mesh is used to represent the geometry. The mesh resolution is defined in our software by the *xy* resolution (or the number of elements per diameter) and the *z* resolution (the spacing between slices). As the mesh resolution increases, the computed displacements converge towards the true displacements. However, the number of degrees of freedom also increases, and thus will strongly affect the computation time. For example, Figure 5.10 shows the relationship between computation time and TM resolution in one of our preliminary experiments. A trade-off in the mesh resolution is necessary to limit the computation time. This will be further discussed in Chapter 7.

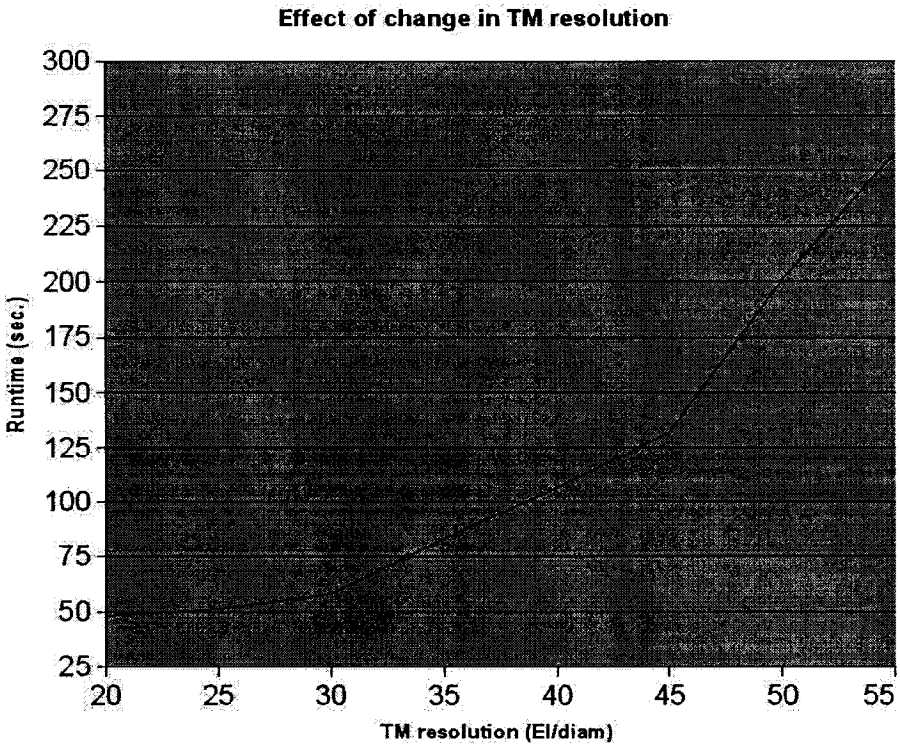

Figure 5.10: *Computation increases with increasing resolution.*

5.5.4 Bandwidth

The computation time is also dependent on the bandwidth of the system stiffness matrix. The bandwidth is defined as the maximum width of the band of non-zero numbers lying along the matrix diagonal. To minimize the computation time for a given mesh, a locally developed bandwidth minimization program (Bwm) is used. It renumbers the nodes using an algorithm developed by Crane *et al.* (1976), adapted to the Sap finite-element program used here. The bandwidth depends on how nodes are connected, and how Fie numbers the nodes. In some cases, the bandwidth was reduced by as much as 95 %.

CHAPTER 6

THE FINITE-ELEMENT MODEL

6.1 Introduction

In this chapter we shall present the details of our newly developed finite-element model (Figure 6.1).

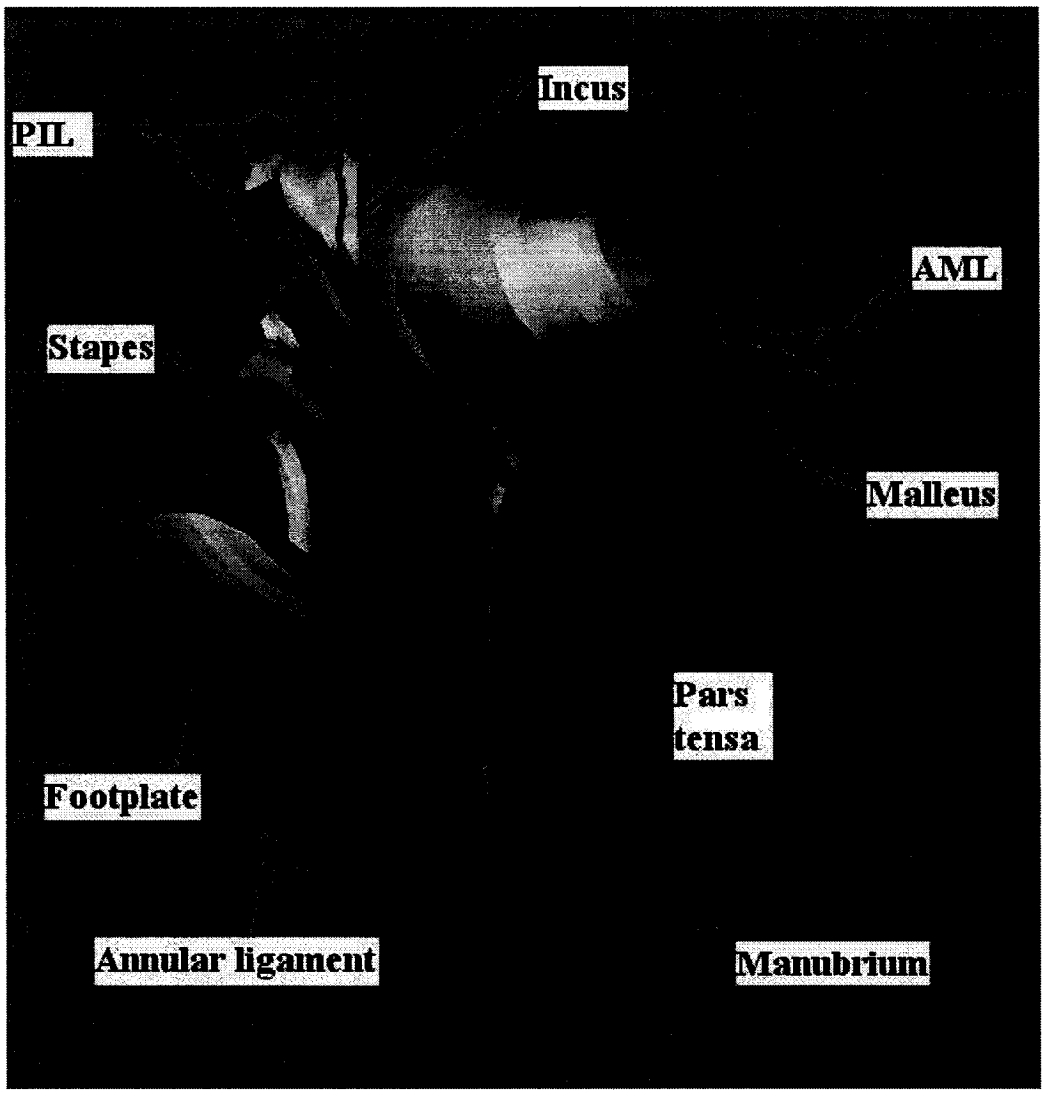

Figure 6.1: *A VRML representation of our complete gerbil middle-ear model. AML = anterior mallear ligament; PIL = posterior incudal ligament.*

All structures were assumed to be homogeneous, with isotropic linear elastic properties. The structures are the tympanic membrane, malleus, incus, stapes, anterior mallear ligament, posterior incudal ligament and stapedial annular ligament.

A detailed description of the characteristics of each structure will follow. The ossicles will be presented in Section 6.2, followed by the tympanic membrane in Section 6.3 and the ligaments in Section 6.4. The two muscles of the middle-ear (tensor tympani and stapedius) were omitted for reasons which will be discussed in Section 6.5.

6.2 Ossicles

6.2.1 Introduction

The following is a description of the ossicles in our model (Figure 6.2). A literature review of the material properties of bone will be presented in Section 6.2.2. This brief review will be followed by descriptions of the ossicles in our model, in Sections 6.2.3 to 6.2.5.

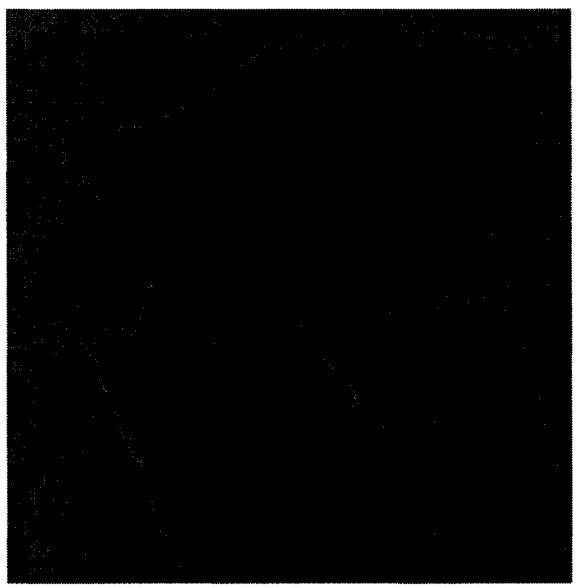

Figure 6.2: *A VRML representation of the ossicles: Malleus (in green), Incus (in red) and Stapes (in blue).*

6.2.2 Material properties

To date, only one experimental study has attempted to determine the mechanical properties of middle-ear bone. Speirs *et al.* (1999) measured a value of about 1.5 GPa (19% standard deviation) for the Young's modulus of human middle-ear ossicle allografts, using axial compression. A number of investigators have measured the Young's modulus of non-middle-ear human and bovine bone specimens. For example, Lang (1969) measured values of about 26 GPa in the axial direction and about 18 GPa in the transverse direction for dried bovine femoral bone, using ultrasonic wave propagation to determine the elastic stiffness. Yoon & Katz (1976) measured a value of about 27 GPa for dried human femoral bone, also using an ultrasonic technique. Reilly & Burstein (1975) reported values of about 23 GPa for fresh bovine femoral bone, and about 17 GPa for fresh human femoral bone, under tensile loading. Currey (1979) measured a value of about 13 GPa for dry bovine femoral bone, under bending load conditions. Fung (1993) reported a value of about 18 GPa in tension for living human bone. Rho *et al.* (1998) reported values of about 22 GPa in the axial direction and about 17 GPa in the transverse direction for dehydrated human tibia specimens, measured by nano-indentation. Mente & Lewis (1994) experimentally measured the elastic modulus of subchondral bone in bovine femoral bone, using a three-point bending test. They reported values of 5.7 GPa ± 0.9 GPa. Ascenzi (1967) measured the tensile Young's modulus of a fully calcified single osteon (of a human femur) to be about 11 GPa, using a micro-testing machine.

Some authors rely on experimental measurements of tissue properties, such as the above mentioned measurements, to characterize their finite-element models. Funnell *et al.* (1992) assigned a Young's modulus to the cat ossicles of 20 GPa, based on measurements from the literature. In more recent finite-element models, values of the Young's modulus for the human ossicles were taken to be 14.1 GPa (Prendergast *et al., 1999;* Sun *et al.*, 2002) and 12 GPa (Koike *et al.*, 2002). The former value was based on Speirs *et al.* (1999). Koike *et al.* (2002) based their value on a review by Evans (1973).

A preliminary value of 20 GPa is assigned to the ossicles in our model. In order to ensure that the ossicles are sufficiently stiff, their rigidity is tested by varying the Young's

modulus. The results are discussed in Chapter 7. Because no measurements of the Poisson's ratio of bone are available, its value was set to 0.3, which is the value used by Funnell *et al.* (1992), Prendergast *et al.* (1999), Koike *et al.* (2002) and Sun *et al.* (2002).

6.2.3 Malleus

The method of choosing thicknesses was explained in Section 5.5.1. Some parts of the malleus were assigned different mesh resolutions (cf. Section 5.5.3) and thicknesses. The thicknesses were 156 μm for the head, 63 μm for the neck and manubrium, and 10 μm for the anterior process. The *xy* resolution varied across the malleus from 75 to 200 elements per diameter, and *z* resolutions of 1 and 2 were used.

6.2.4 Incus

The thicknesses assigned to the incus were 156 μm for the head, 50 μm for the long process, 21 μm for the lenticular process, and 36 μm for the posterior process. The *xy* resolution varied across the incus from 75 to 200 elements per diameter, and *z* resolutions of 1 and 2 were used.

The pedicle of the incus was the only part of the ossicles to be modeled using volume elements (Figure 6.3). This decision was based on the work done by Siah (2002) and Funnell *et al.* (2005), who concluded that the pedicle may not be rigid (and may play a major role in the motion between the incus and the stapes. As in that work, a Young's modulus of 5 GPa was assigned to the pedicle based on the measurements of Mente & Lewis (1994).

As mentioned in Section 5.3.1, micro-CT images were used as a supplement to establish the geometry of the pedicle. The latter was not based directly on the micro-CT data because of time constraints. The thickness of the pedicle was determined to be about 30 μ m, based on the micro-CT data, but its thickness was set to 45 μm, which is the voxel size (slice thickness) on the MRM images. On the other hand, there were no restrictions in the *x-y* plane (width and length) of the pedicle, and coordinates can be fractions of pixels in Fie. The width and length of the pedicle are approximately 70 μm and 140 μm, respectively.

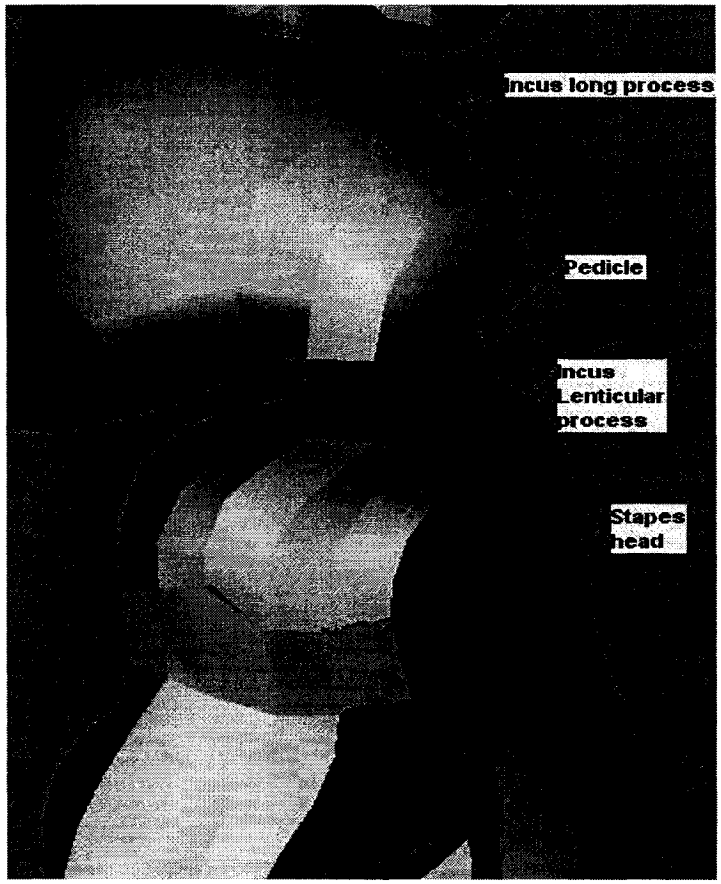

Figure 6.3 *A VRML representation of the pedicle.*

6.2.5 Stapes

The different regions of the stapes were assigned the following thicknesses: 42 μm for the head, 21 μm for both crura, and 31 μm for the footplate. Throughout the stapes, the *z* and *xy* resolutions were set to 1 and 75 elements per diameter, respectively. Only the footplate was based on the CT images. An explanation will be provided at the end of this chapter, when the stapedial annular ligament is discussed.

6.3 Tympanic membrane

6.3.1 Overall shape

The pars tensa (PT) in the MRM dataset appeared to be smooth but might have been distorted by the liquid. The pars flaccida (PF) definitely appeared to be displaced and its layers appeared to have been separated by the liquid inserted into the middle ear prior to MRM scanning (Figure 6.4). Hence, we resorted to using phase-shift moiré topography to generate a finite-element model of the complete TM, as discussed in Section 5.3.3.

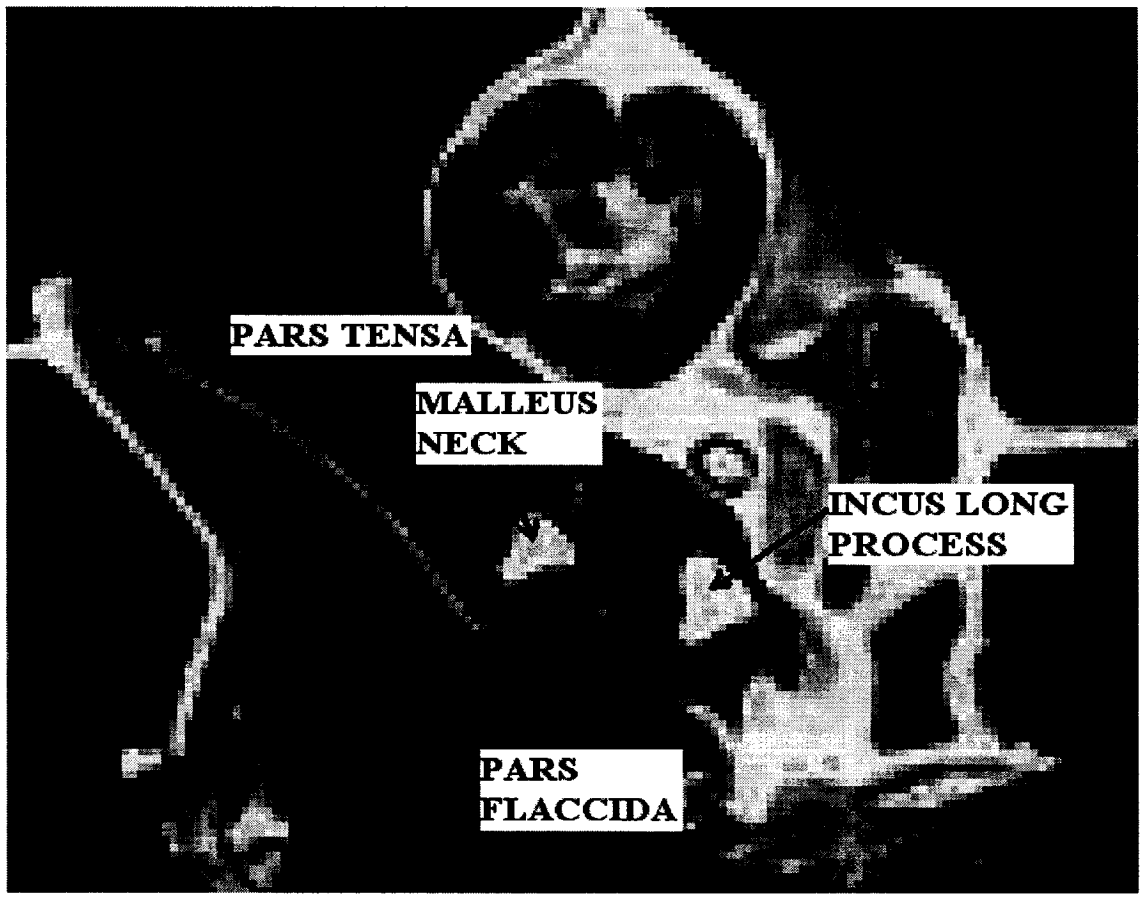

Figure 6.4: *MRM section of the gerbil middle ear, as viewed on Fie.*

6.3.2 Thickness

Von Unge *et al.* (1991) measured the thickness of the gerbil TM using light microscopy and transmission electron microscopy, after a delicate preparation process described in

the first paragraph of the "Materials and Methods" section of the paper. The study reported a thickness of 3-5 μm for the PT between its periphery and the manubrium, and a thickening towards the periphery up to about 20 μm. The PF was reported to be almost uniformly thick throughout, ranging between 10 and 20 μm. In a later study, von Unge *et al.* (1999) obtained mean PT thicknesses of about 3 μm in the central region between the umbo and manubrium, and about 18 μm near the annulus. Both studies used histological sections of TM tissue.

More recently, confocal laser scanning microscopy (CLSM) was used to measure the thickness of the gerbil PT (Kuypers *et al.,* 2000; Kuypers, 2005). The key feature of CLSM is its ability to provide direct, non-invasive serial optical sectioning of intact, relatively thick specimens with minimum sample preparation. The gerbil TM thickness measurements done by Kuypers (Figure 6.5) had an accuracy of 0.9 μm. Seven TM's (six right and five left) of healthy mature female Mongolian gerbils were used for the PT measurements, and three TM's (two right and one left) were used for the PF measurements. Overall, the PT thickness had a rather uniform value of about 7 μm. In the central region, shaped like a horse-shoe, thickness ranged from 5.6 μm to 14.4 μm. The PT thickens sharply near the outer edge, with values of 28.8 μm with a standard deviation of 0.7 μm (region B in Fig. 6.5). A pronounced thickening of 34 μm (standard deviation of 0.7 μm) extends as a ring along the entire annular periphery of the PT (region A in Fig. 6.5). Near the manubrium (region M in Fig. 6.5), the PT thickens to 21.1 μm, with a standard deviation of 0.7 μm. The PF is thicker than the PT. In the PF central region, the mean thickness is about 23.5 μm, with a standard deviation of about 4 μm. The PF thickens, up to about 80 μm, near the edges.

In our gerbil finite-element model, the pars tensa and pars flaccida were given uniform thicknesses of 7 μm and 24 μm, respectively, for simplicity.

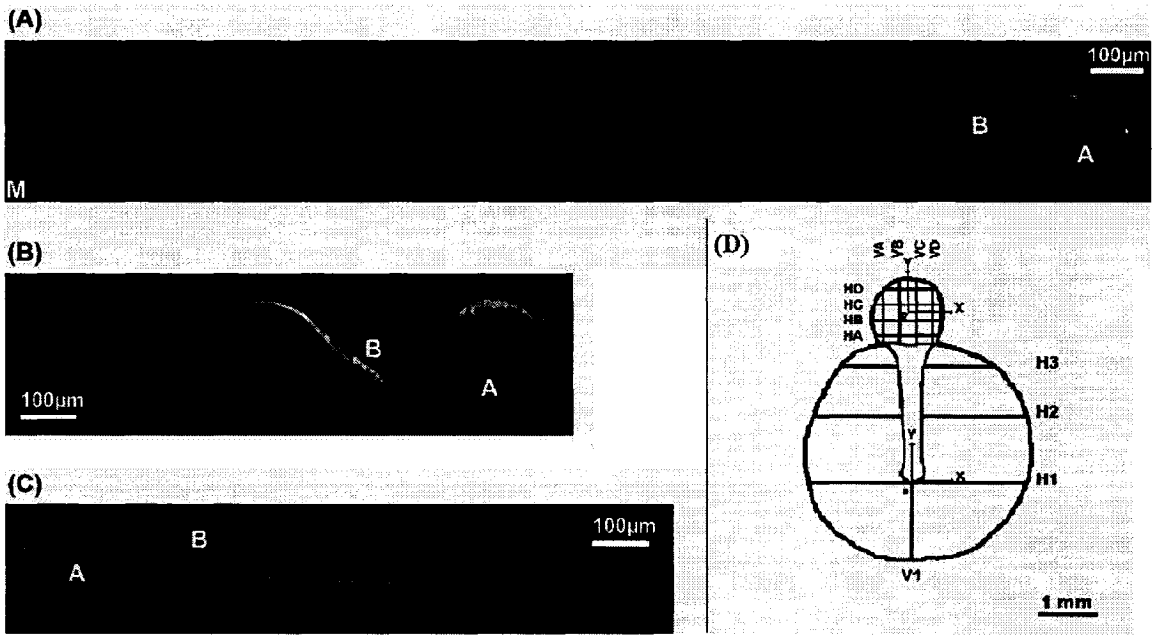

Figure 6.5: *Complete scan of a cross-section of a left gerbil TM along line V1 (a), line H1 (b) and line H2 (c). The manubrium (M), bulge (B) and annular ring (A) are indicated. (d): A schematic representation of a gerbil TM. (Kuypers, 2005)*

6.3.3 Material property

The elastic properties of the TM are not well known. Very few studies have attempted to determine these properties for the human TM, and none in animals. Békésy (1949) found a Young's modulus of about 20 MPa, using a beam-bending test. Kirikae (1960) measured a Young's modulus of about 40 MPa, using a longitudinal vibration technique. Decraemer *et al.* (1980) found a value of about 23 MPa at large strains, using a uniaxial tension test. Most recently, Fay *et al.* (2005) used theoretical methods to assess Young's modulus values for cat and human TM assuming first isotropy, then orthotropy. When the material properties of the TM fibre layers are assumed orthotropic, the elastic modulus of the TM lay in the range 100-200 MPa in their human model, and 100-400 MPa for their cat model. Values for the isotropic case in the cat and human models were 30-60 MPa for the posterior region of the TM, and 60-90 MPa for the anterior region. In all of the papers mentioned in this paragraph, the studies were performed on the PT and not on the PF.

In our model, the Young's modulus of the PT was set to 60 MPa. For the PF the Young's

modulus was set to 20 MPa, based on Koike *et al.* (2002). The latter assumed that the Young's modulus of the PF is a third of that of the PT, because of a lack of measurements of the mechanical properties of the PF.

Both the PF and the PT (Figure 6.6 & 6.7) were triangulated with an *xy* resolution of 30 elements per diameter (Funnell & Decraemer, 1996). The software used were Fud and Mum, which were developed by Dr. WRJ Funnell.

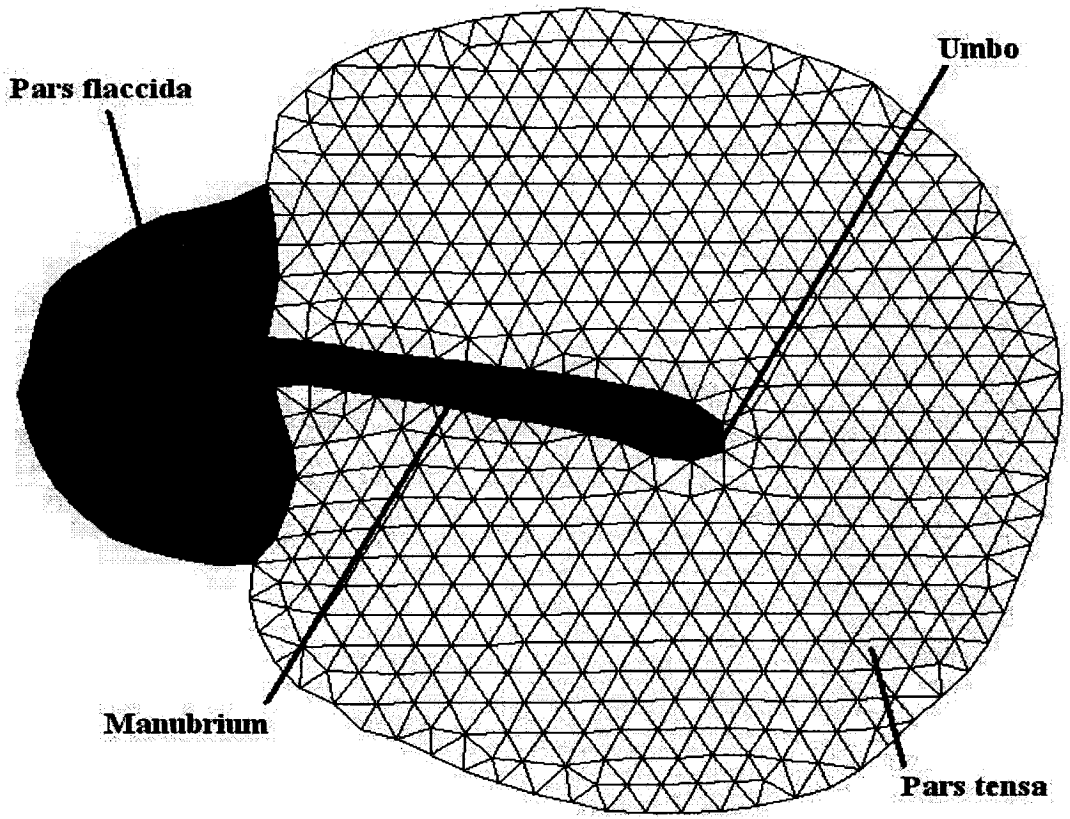

Figure 6.6: *2-D illustration of the gerbil TM model, viewed with the pre-processor Fad.*

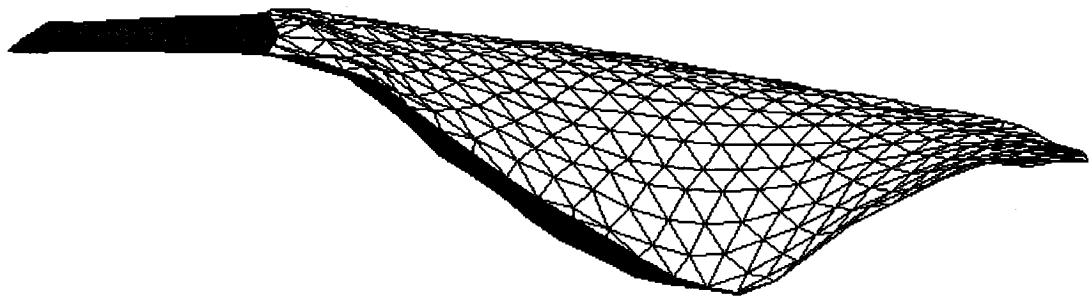

Figure 6.7: *3-D illustration of the gerbil TM model, viewed with Fad.*

6.3.4 Fibrocartilaginous ring

The fibrocartilaginous ring around the TM was not segmented. The resolution of the MRM images available is not sufficiently high to clearly identify the ring. In a finite-element model analysis of the moustached bat, van Wijhe (2000) simulated radial forces applied on the fibrocartilaginous ring around the TM. He observed that the ring was essentially rigid compared with the TM, at least at low frequencies. Therefore, the outer ends of the TM – where the latter meets the ring – were fully clamped in our model. This means that there are zero displacements in the 6 degrees of freedom (3 translational and 3 rotational).

6.4 Ligaments

The following is a description of the ligaments in our model. The anterior mallear ligament and the posterior incudal ligament will be presented in Section 6.4.1, followed by the stapes annular ligament in Section 6.4.2.

6.4.1 Mallear and incudal ligaments

To date, no experimental measurements of the elastic properties of the middle-ear ligaments have been done. Authors have fitted their models to experimental data to determine the Young's modulus of the ligaments (Prendergast *et al.*, 1999; Koike *et al.*, 2002; Sun *et al.*, 2002). In our model, the Young's modulus of the anterior mallear ligament and posterior incudal ligament was set to 20 MPa, based on non-middle-ear

measurements. This *a priori* value was used in previous models in our lab (Funnell *et al.*, 1996; Ladak & Funnell, 1996; Ghosh & Funnell, 1995).

The anterior mallear ligament is connected at one end to the anterior process of the malleus, and it is clamped at the other end to represent its attachment to the cavity wall. It was modeled with volume elements. The *xy* and *z* resolutions were set to 200 elements/diameter and 1, respectively.

The posterior incudal ligament is composed of two distinct bundles, one medial and the other lateral to the incus posterior process. Both bundles are connected on one side to the incus posterior process, and are clamped at the other ends to represent their attachments to the cavity wall. The *xy* and *z* resolutions were set to 200 elements per diameter and 1, respectively.

6.4.2 Annular ligament

Lynch et al. (1982) reported that the annular ligament controls the behaviour of the acoustic impedance of the stapes and cochlea at frequencies below 1 kHz. Based on measurements of the vestibular sound pressure and stapes velocity, the impedance was determined. Assuming that the annular ligament is composed of a homogeneous and isotropic material, and that the stapes motion is piston-like (purely translational), they calculated a value of 10 kPa for the Young's modulus of the stapedial annular ligament. This value was used by Sun *et al.* (2002) and Mikhael (2005) in their finite-element models. It was also used in our finite-element model.

The annular ligament is connected on its interior side to the stapes footplate, and on its exterior side to the oval window. It was modeled with volume elements, and with an *xy* resolution of 100 elements per diameter and a *z* resolution of 1. The attachment to the oval window was represented as a fixed boundary condition (i.e., zero displacements).

As explained in Section 5.3.1, the contours of the annular ligament were segmented from the micro-CT images because the resolution of the MRM was so low that it was impossible to discern the ligament. Because of the intimacy of the connection, the

footplate was also segmented from the micro-CT images. As mentioned in Section 5.4.2, the volume-meshed annular ligament was joined to the surface-meshed footplate using the Fad pre-processor (Figure 6.8, A). The combined structure was then joined with the inferior ends of the crura from the MRM images (Figure 6.8, B). The splatter of orange triangles around the outside of the footplate is a visual artefact produced by Fad and has no effect on the properties or behaviour of the model.

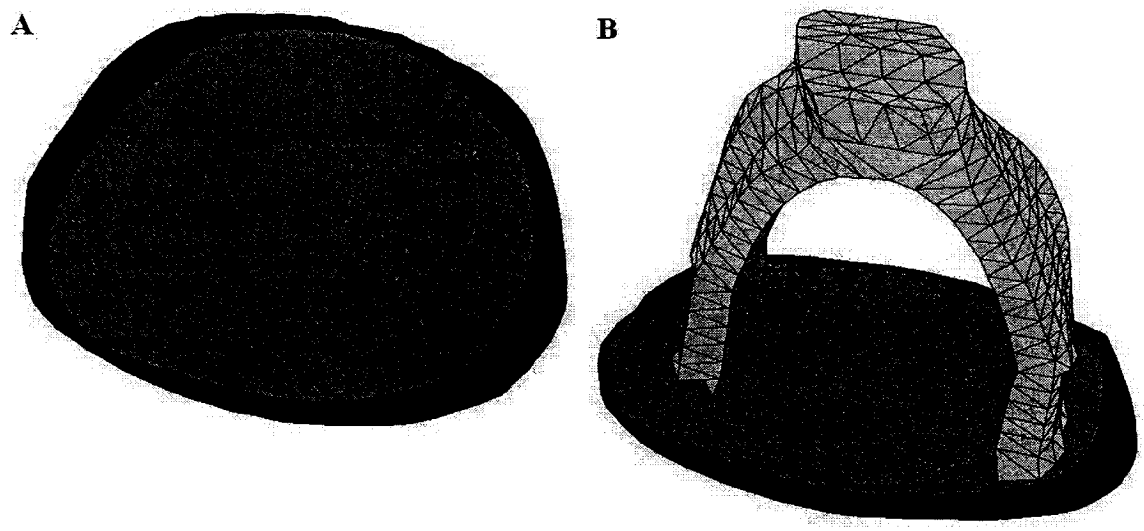

Figure 6.8: ***A****: 3-D representation of the annular ligament (in blue) and the stapes footplate (in orange), on Fad software.* ***B:*** *Stapes crura (in yellow) and stapes footplate (in orange).*

6.5 Muscles

As mentioned at the beginning of this chapter, middle-ear muscles have been omitted from the finite-element model. The animal and human experiments described in the literature, which we are using for comparison with our model, are done under anaesthesia or post-mortem. In such conditions, the muscles are in a relaxed state. The passive mechanical effects of the middle-ear muscles are negligible: Dirckx & Decraemer (2001) have assessed that, at very low frequencies, the passive muscles do not play a significant role in controlling ossicular motion.

CHAPTER 7

RESULTS

7.1 Introduction

Simulation results for the complete gerbil finite-element model – subjected to a static pressure of 1 Pa applied to the eardrum – are presented and discussed in this chapter. The preliminary convergence tests on mesh-resolution (Section 7.2) and ossicular stiffness (Section 7.3) will lead to the final base model whose results are presented in Section 7.4. In Section 7.5, the sensitivity of the model to each parameter is evaluated. We compare our findings with experimental results in Section 7.6. Finally, a summary will be presented in Section 7.7.

7.2 Convergence test

In Section 5.5.3, we discussed the need for convergence testing. In this section, the final model's mesh resolution is tested. The number of elements per diameter (*xy*-resolution) and the slice spacing (z-resolution) were varied for all structures. Results for the stapes footplate displacements are shown for each simulation, as well as the time elapsed for each simulation.

We performed eight runs, with resolutions varying as follows: *x*-*y* resolutions varied between 20 and 100 el/dia (elements per diameter) for the ossicles, between 50 and 200 el/dia for the ligaments and pedicle, and between 20 and 30 el/dia for the TM. Slice spacings (or *z* resolutions) of 1 and 2 were used for the ossicles and TM, but a *z* resolution of 1 was always used for the ligaments and pedicle because of their small sizes. The results are summarized in Figures 7.1 and 7.2.

Figure 7.1 shows that, with increasing resolution, stapes footplate displacement increases sharply at low resolutions, then gradually at higher resolutions, until it reaches a "plateau region" where changes in displacements are insignificant. At a mesh size of about 7500

elements, stapes displacement values reach 97% of the maximum value of the "plateau region". At about 9000 elements, displacement values reach 99.7% of the maximum value of the "plateau region".

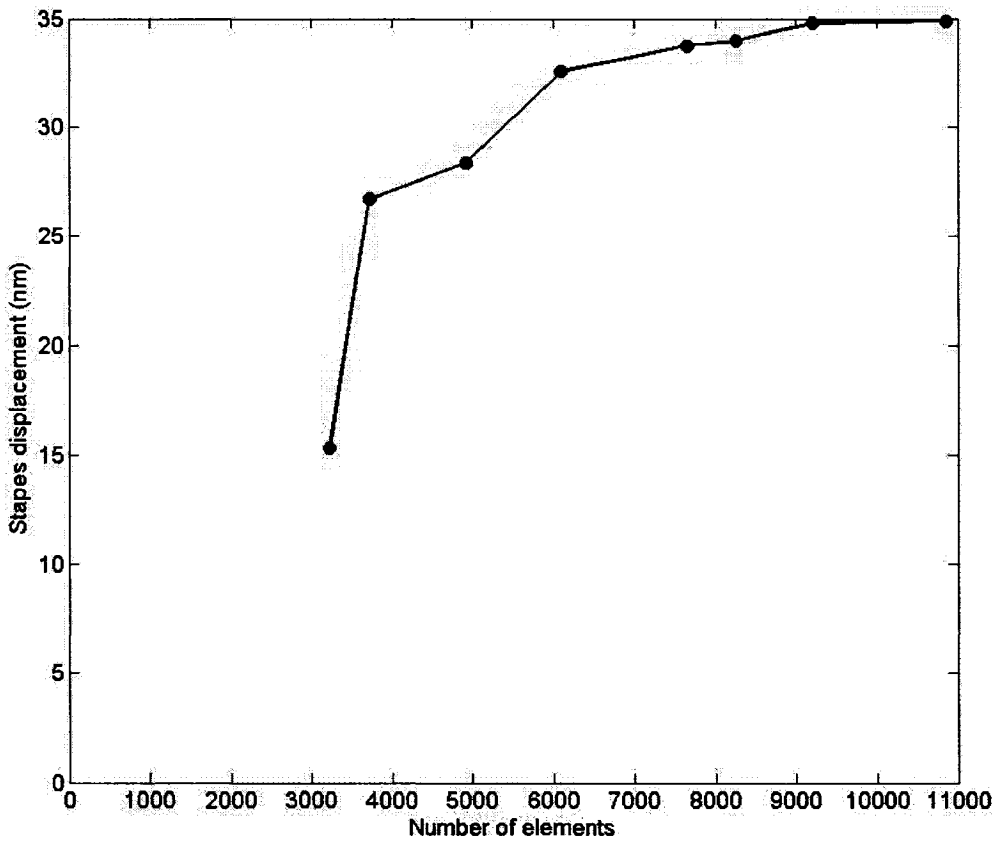

Figure 7.1: *Middle-ear model convergence test. The mesh-resolution is defined by the number of elements.*

Figure 7.2 shows that, with increasing resolution, computation time increases exponentially. We decided to choose a resolution of 9208 elements, the computation time for each run being less than 780 seconds (or 13 minutes). Beyond that point, the computation time increases by more than 1000 seconds but displacements change by less than 1 nm.

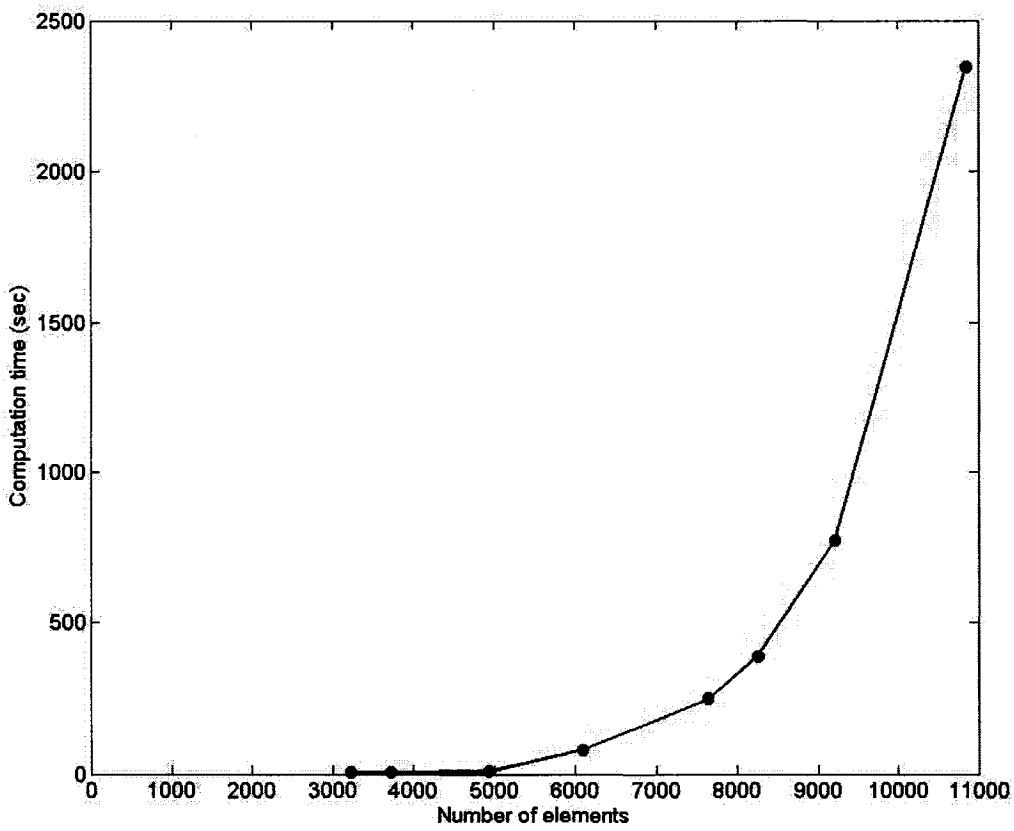

Figure 7.2: *Effect of mesh resolution on computation time.*

7.3 Ossicular stiffness

In this section, we investigate the ossicular stiffness of the model. As discussed in Section 6.2.2, we need to determine an elastic modulus for the ossicles. We use thin-shell elements for the ossicles (cf. Section 5.5).

To evaluate the rigidity of the ossicular model, the Young's modulus for the shell elements was changed for each simulation in this test. For reasons mentioned in Section 6.2.3, the Young's modulus of the pedicle was kept constant. It is expected that the displacements will change as the degree of flexibility of the shell elements changes, and

that displacements will become more or less constant as the elements become rigid.

Figures 7.3 to 7.6 show the effects of the shell-element Young's modulus on the maximum displacements of the pars tensa, manubrium, pedicle and stapes footplate, respectively. The Young's modulus of the ossicles ranged from 1 uPa to 200 GPa.

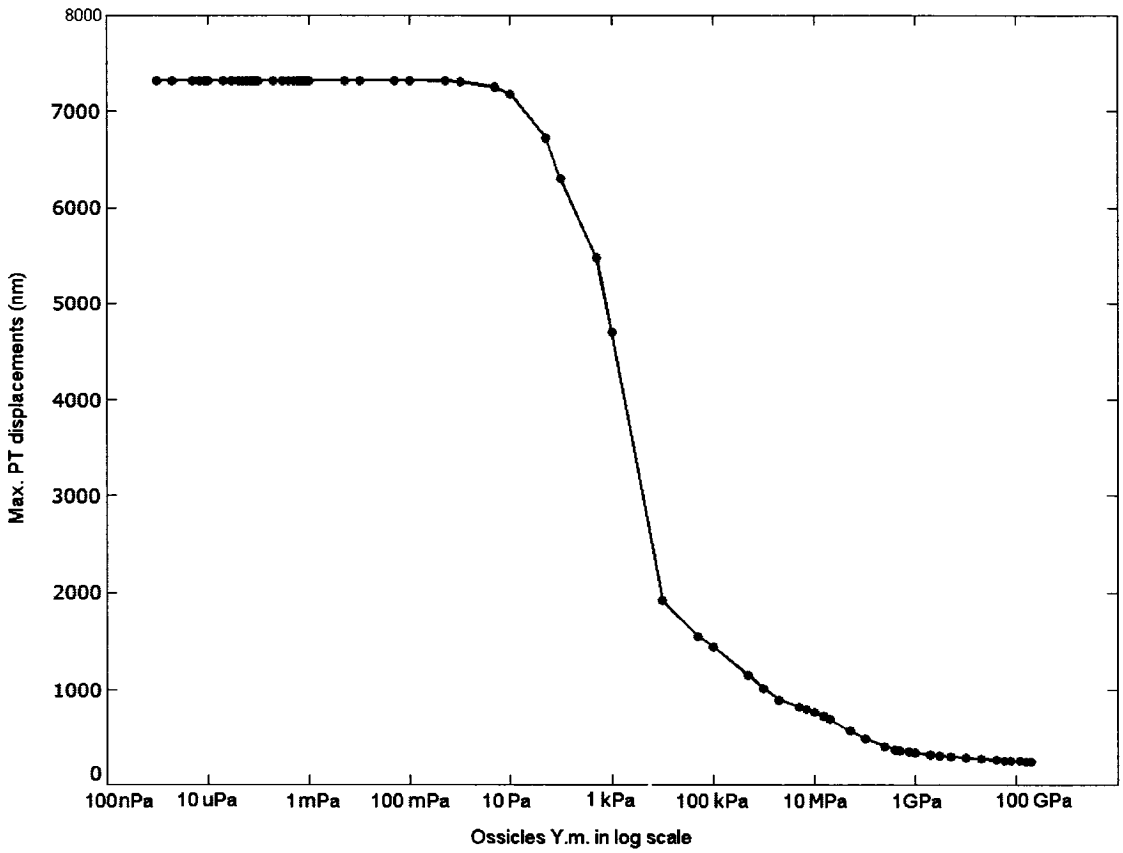

Figure 7.3: *Effect of the ossicular Young's modulus on the maximum displacement of the pars tensa.*

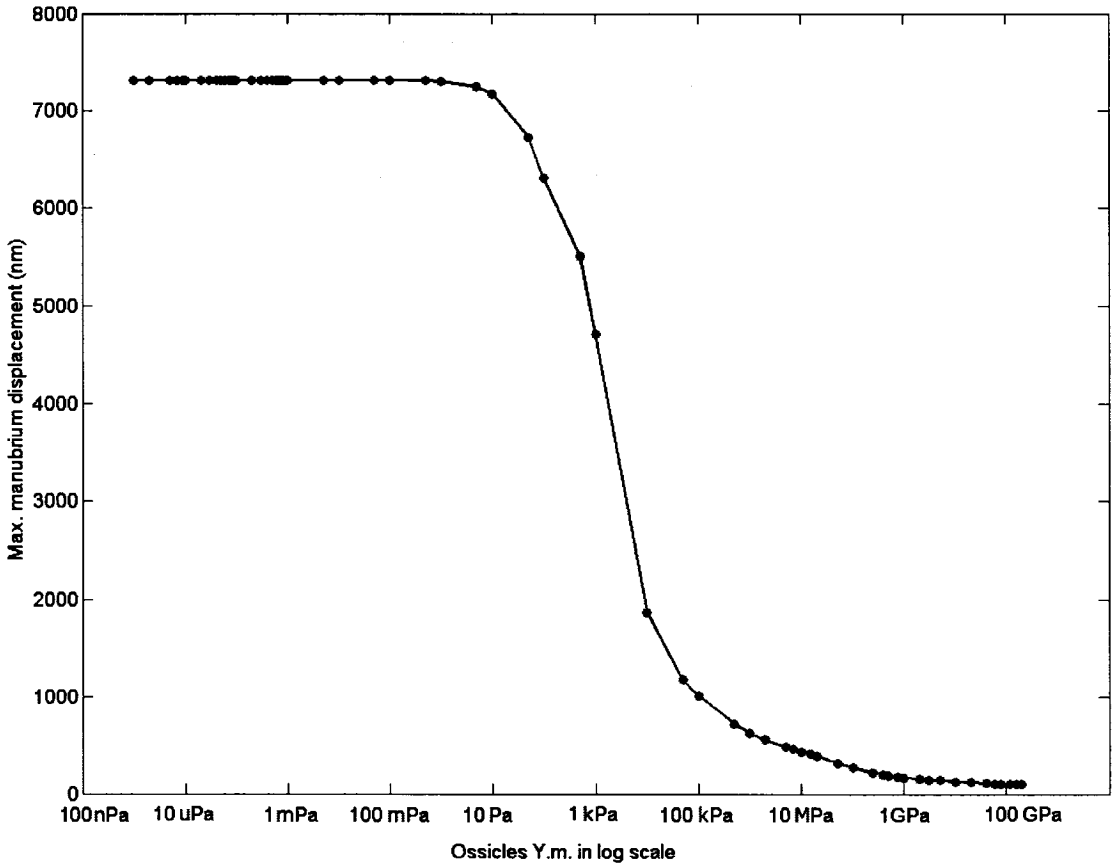

Figure 7.4: *Effect of the ossicular Young's modulus on the maximum displacement of the manubrium.*

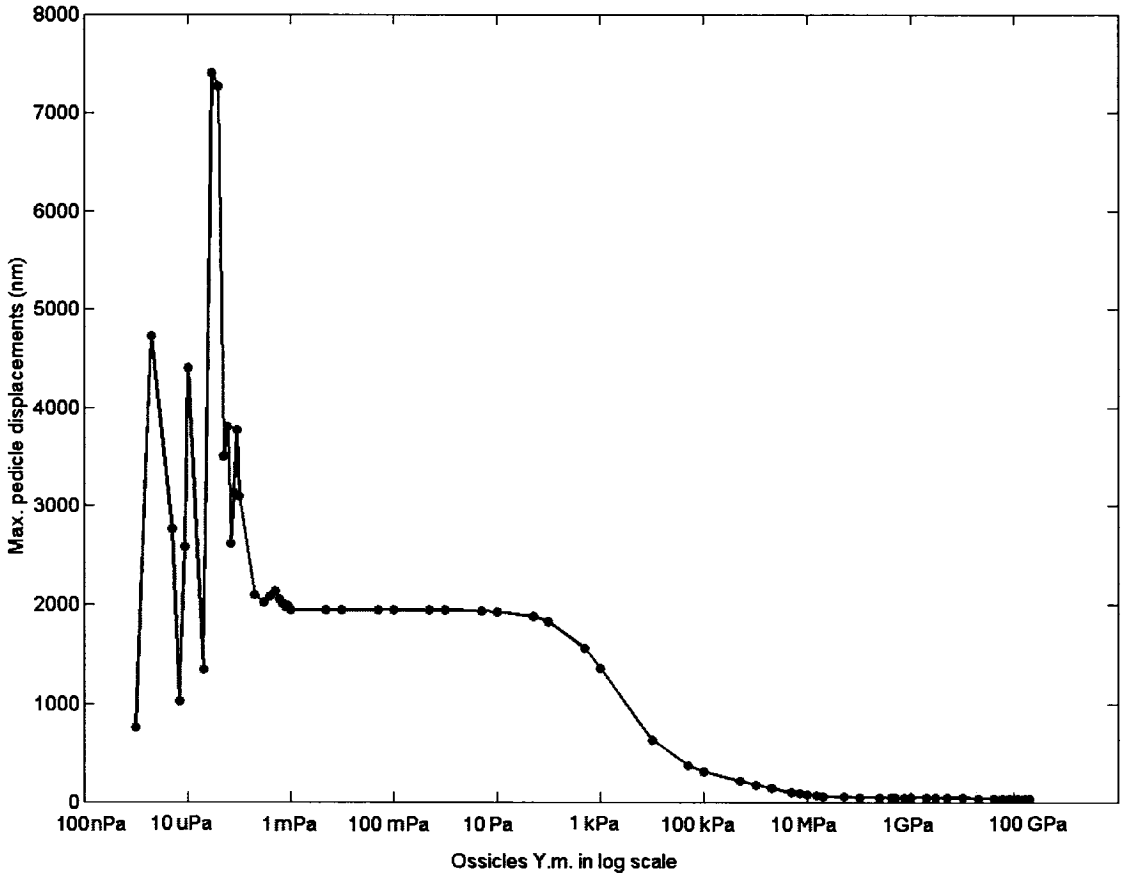

Figure 7.5: *Effect of the ossicular Young's modulus on the maximum displacement of the pedicle.*

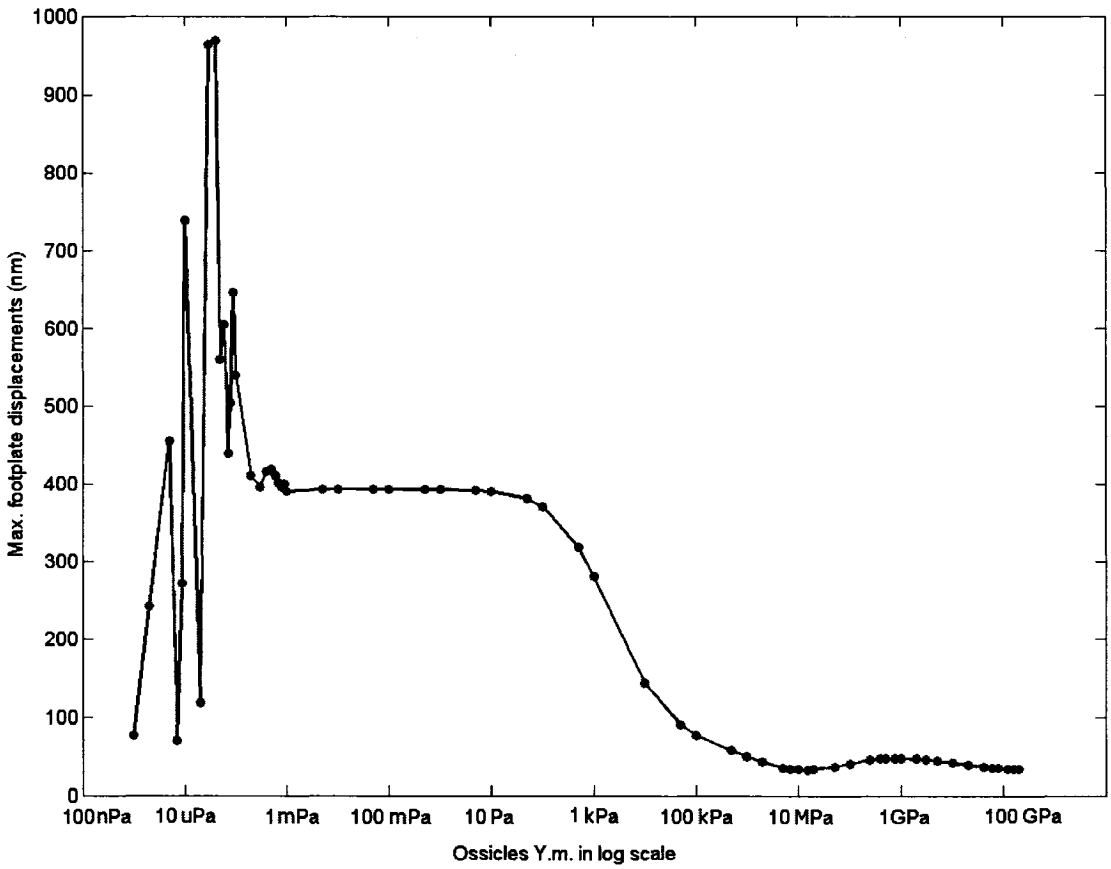

Figure 7.6: *Effect of the ossicular Young's modulus on the maximum displacement of the footplate.*

For the purpose of choosing the Young's modulus, the right-hand end of the range is the important part. When the elastic modulus of the ossicles increases from 1 GPa to 80 GPa, the displacements decrease by 25%, 39%, 29% and 27% for the PT, umbo, pedicle and footplate, respectively. The displacements decrease by less than 3% for all four measured locations beyond a Young's modulus value of about 80 GPa. This means that the displacement changes are negligible, and the ossicles are stiff enough. Therefore, a nominal Young's modulus value of 80 GPa will be used for the shell elements representing the ossicles.

In order to confirm that the model would behave as expected, we investigated the lower parts of the curves. As the ossicles become less stiff, the coupling with the TM decreases,

and the pars tensa (PT) displacements increase (Figure 7.3). When the ossicles are so flexible that they have no more influence on the eardrum (i.e., below a Young's modulus of about 10 Pa), the PT displacements approach a constant value of about 30 times the nominal value at 80 GPa. The manubrium displacements show a similar behaviour (Figure 7.4). They approach a constant value of about 70 times the nominal value when the ossicular Young's modulus decreases to about 1 Pa.

Although we might have expected the pedicle displacements to decrease as the ossicles become less stiff, they show a behaviour similar to that of the PT and manubrium. When the Young's modulus of the ossicles decreases, the increasing TM displacements more than compensate for the decreasingly effective coupling. Therefore, pedicle displacements increase until they approach a constant value of about 58 times the nominal value, the stiffness of the ossicles having no more effect on the load transferred by the TM. In Figure 7.5, this occurs at a Young's modulus of about 1 Pa.

Below a Young's modulus of about 1 mPa, pedicle displacements show an erratic behaviour. The onset of erratic results is the beginning of numerical problems which increase for lower Young's moduli. These numerical problems occur due to round-off and truncation in floating-point computations of the finite-element software.

The footplate displacements show a behaviour similar to that of the three other displacement locations measured, below 15 MPa (Figure 7.6). They approach a constant value of about 11 times the nominal value when the ossicles Young's modulus decreases to about 1 Pa. Above 15 MPa the footplate shows a different behaviour than the other structures do (Figure 7.7). Rather than continuing to decrease as in the TM, umbo and pedicle, footplate displacements increase as the stiffness of the ossicles increases. At about 1 GPa, the displacements reach a peak before dropping. As the ossicular stiffness is increased to even higher values, footplate displacements approach a constant value.

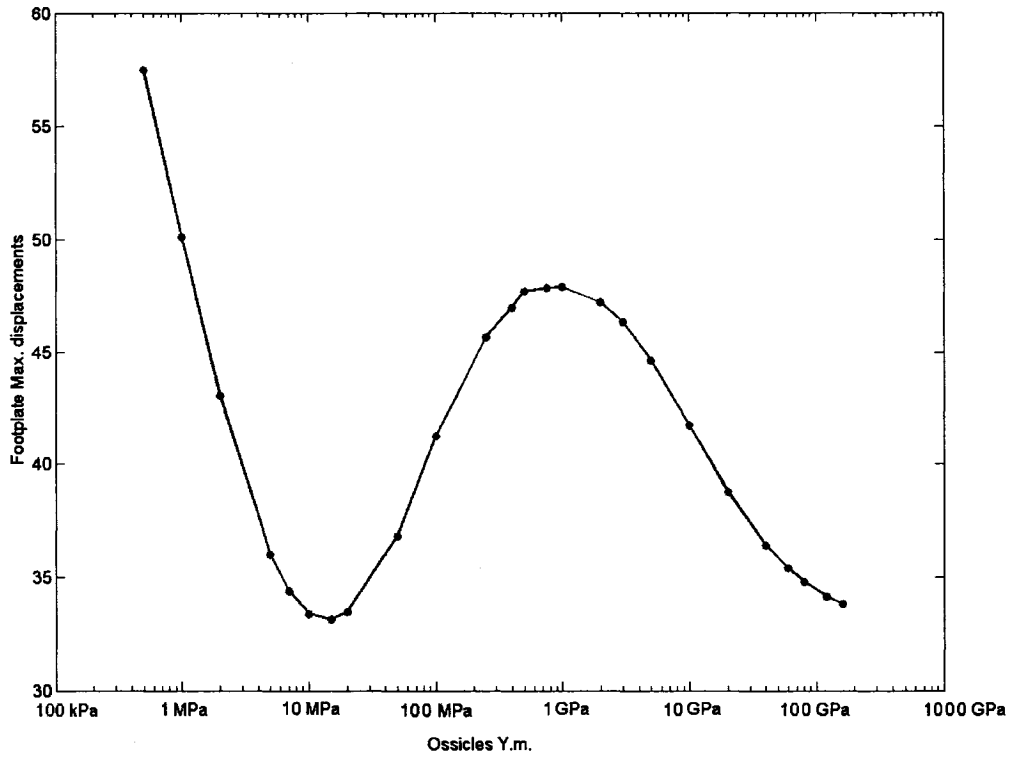

Figure 7.7: *Effect of the ossicles Young's modulus on the footplate displacements. This is a greatly magnified version of the right-hand part of Figure 7.6.*

Figure 7.8 shows the displacement patterns of the footplate at ossicular Young's moduli of 15 MPa, 1 GPa and 120 GPa.

Figure 7.8-A shows that at 15 MPa the footplate displacements are maximal in the two regions where the crura are connected. Figures 7.8-B & 7.8-C show that at 1 and 120 GPa the footplate displacements are uniform. The footplate mode change, from rigid (uniform displacement at 1 and 120 GPa) to flexible (bulging under the crura at 0.01 GPa), occurs on the lower side of the peak in the footplate displacement curve (Figure 7.7). The onset of bulging presumably causes the more complicated shape of the footplate displacement curve.

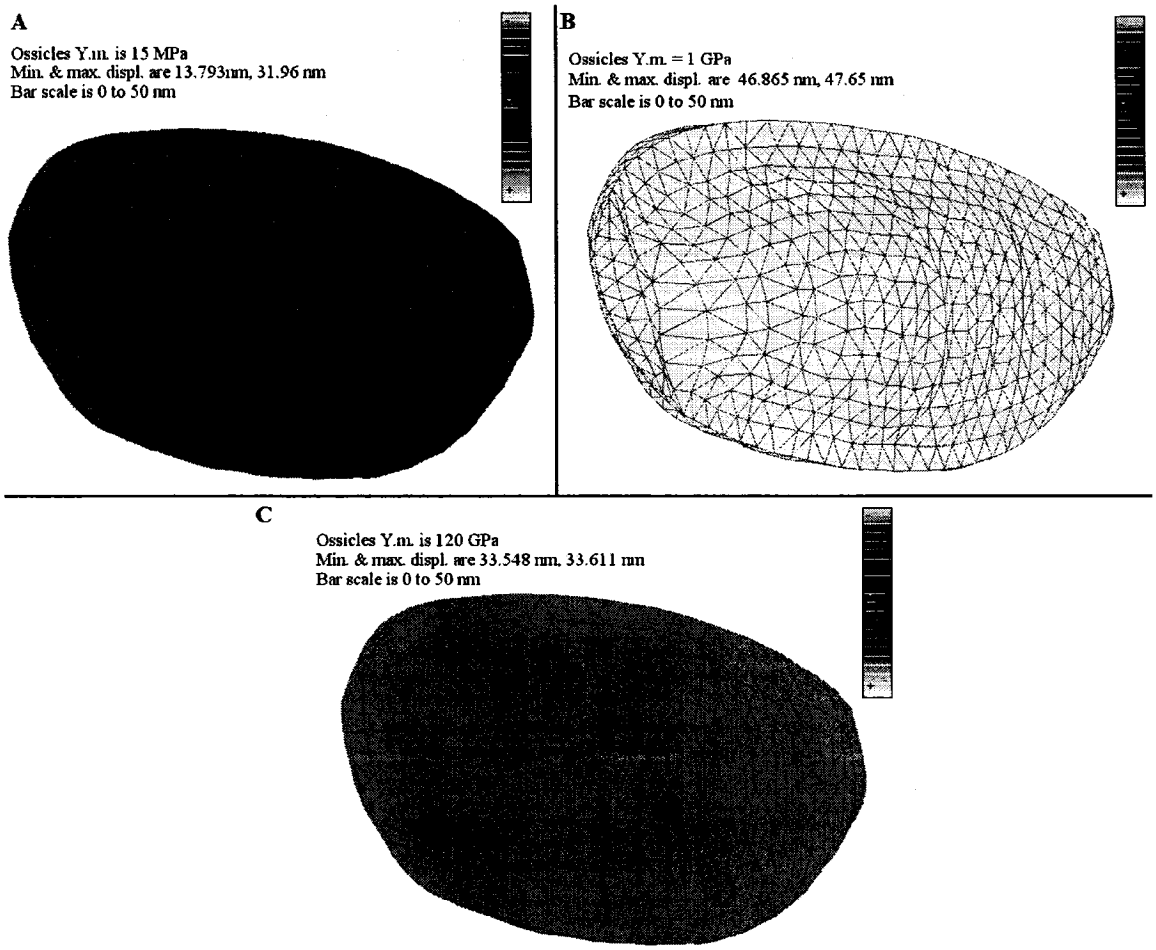

Figure 7.8: *Footplate displacement pattern at ossicular Young's moduli of 15 MPa (A), 1 GPa (B) and 120 GPa (C).*

7.4 Base model results

7.4.1 Introduction

Model results based on the *a priori* estimates of material properties will be shown as screen shots from the post-processor Fod, a locally developed program by Dr. WRJ Funnell (http://audilab.bmed.mcgill.ca/~funnell/AudiLab/sw/fod.html), implemented in Fortran. Minimum and maximum displacements are presented for each material type on the left side on the screen. A colour scale is used to represent the displacements: the scale ranges from black through blue, green and yellow to white for positive displacements,

and from black to red for negative displacements. Lines of constant displacements are also shown to clarify the changes in displacement patterns. The maximum (and minimum) displacement values displayed indicate the maximum (or minimum) displacement vectors for each structure with a specific material type.

7.4.2 TM and manubrium displacements

Figure 7.9 displays the displacement pattern of the eardrum and the maximum displacement values. The maximum pars flaccida (PF) displacement is 65 nm. There are two points of maximum displacement on the pars tensa (PT): one in the posterior region, the other in the anterior region. The larger of the two maximum displacements is 250 nm, in the posterior region.

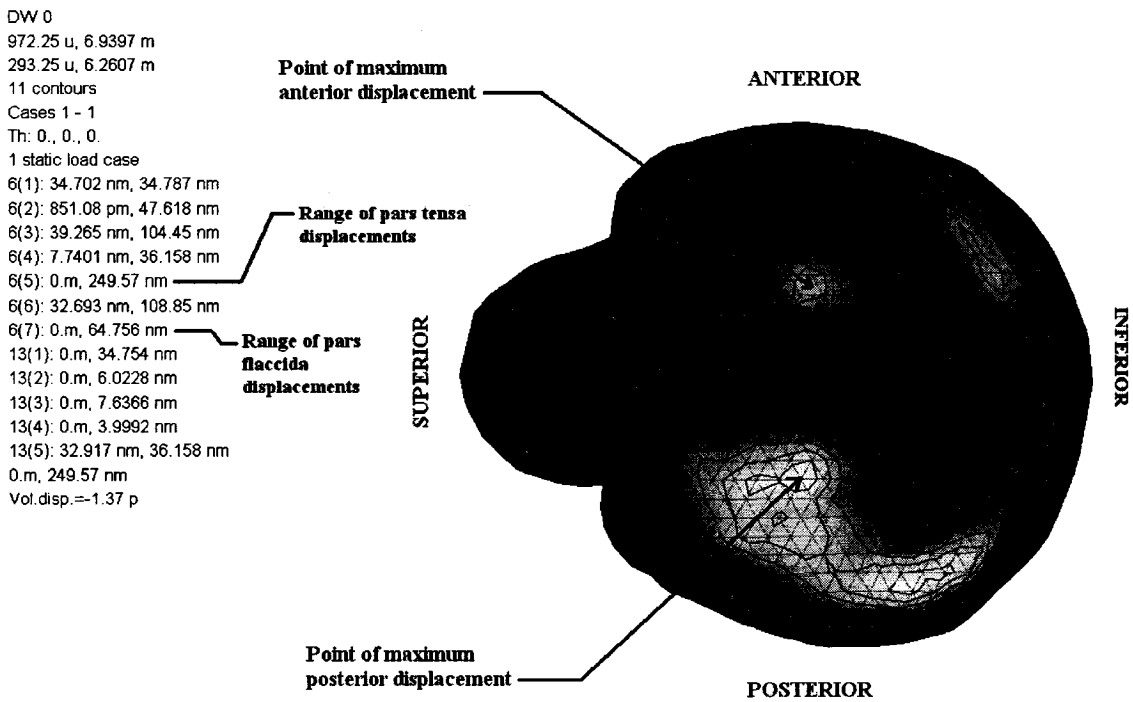

Figure 7.9: *Displacement (or vibration) pattern of the TM in response to a static pressure of 1 Pa, as viewed in Fod. Maximum displacements for the PT and PF are 250 nm and 65 nm, respectively.*

Figure 7.10 displays the vibration pattern of the manubrium. The displacement range for the colour scale is different from that in Figure 7.9 because, the ossicular displacements

being much lower than those of the TM, the range for the colour scale was lowered to show clear vibration patterns for the ossicles. The maximum displacement (104.5 nm) occurs at the umbo. Along the manubrium, contours of constant displacement appear to be equidistant. This indicates that there is little or no manubrial bending.

7.4.3 Axis of rotation

Figure 7.10 shows the apparent axis of rotation of the ossicles. The colours indicate the displacement in the *z*-direction, which is the direction normal to the plane of the figure. The axis, as indicated by the region of very small displacements, extends from the posterior incudal ligament to near the anterior mallear ligament. Figures 7.11 and 7.12 display the displacement vectors of the ossicles, as viewed along the axis of rotation from the anterior and posterior views, respectively. The direction of the vectors clearly shows the nature of the rotation about the axis. This is more or less consistent with the classical description discussed in Sections 3.2.2 and 3.3.2.

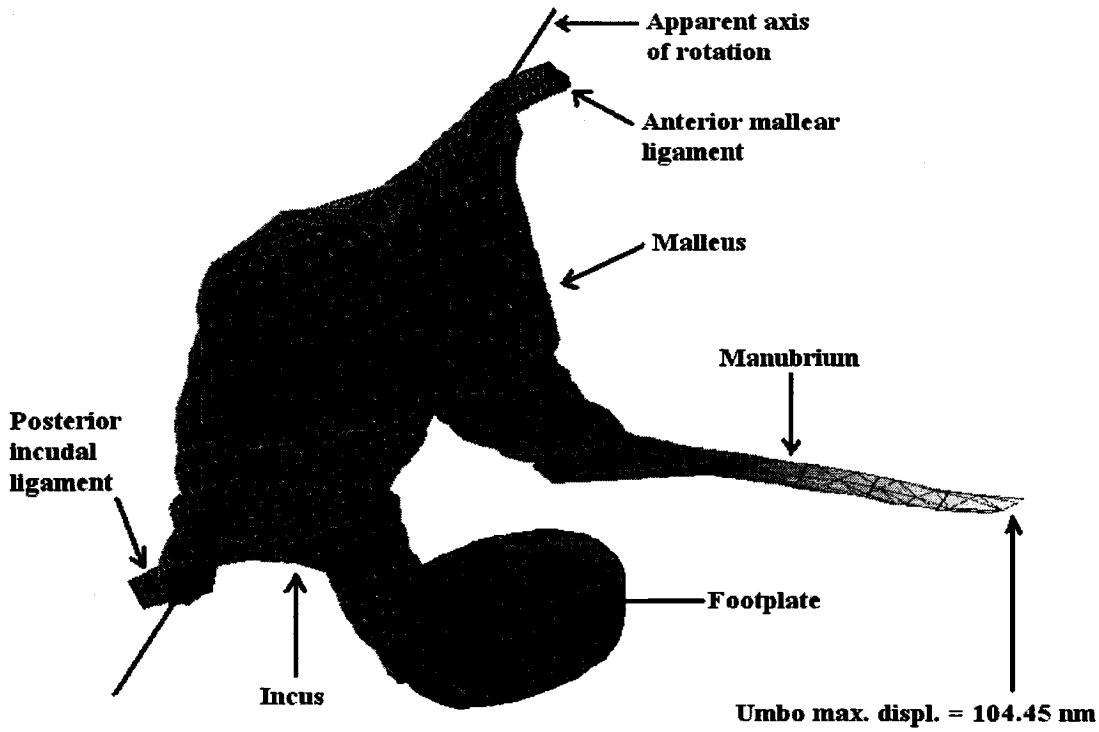

Figure 7.10: *Apparent axis of rotation, from the anterior mallear ligament to the posterior incudal ligament.*

Figures 7.11 and 7.12 also show that the displacement vectors at the footplate, and elsewhere on the stapes, are parallel to each other. This indicates a conversion from rotational motion to translational motion, apparently happening at the pedicle.

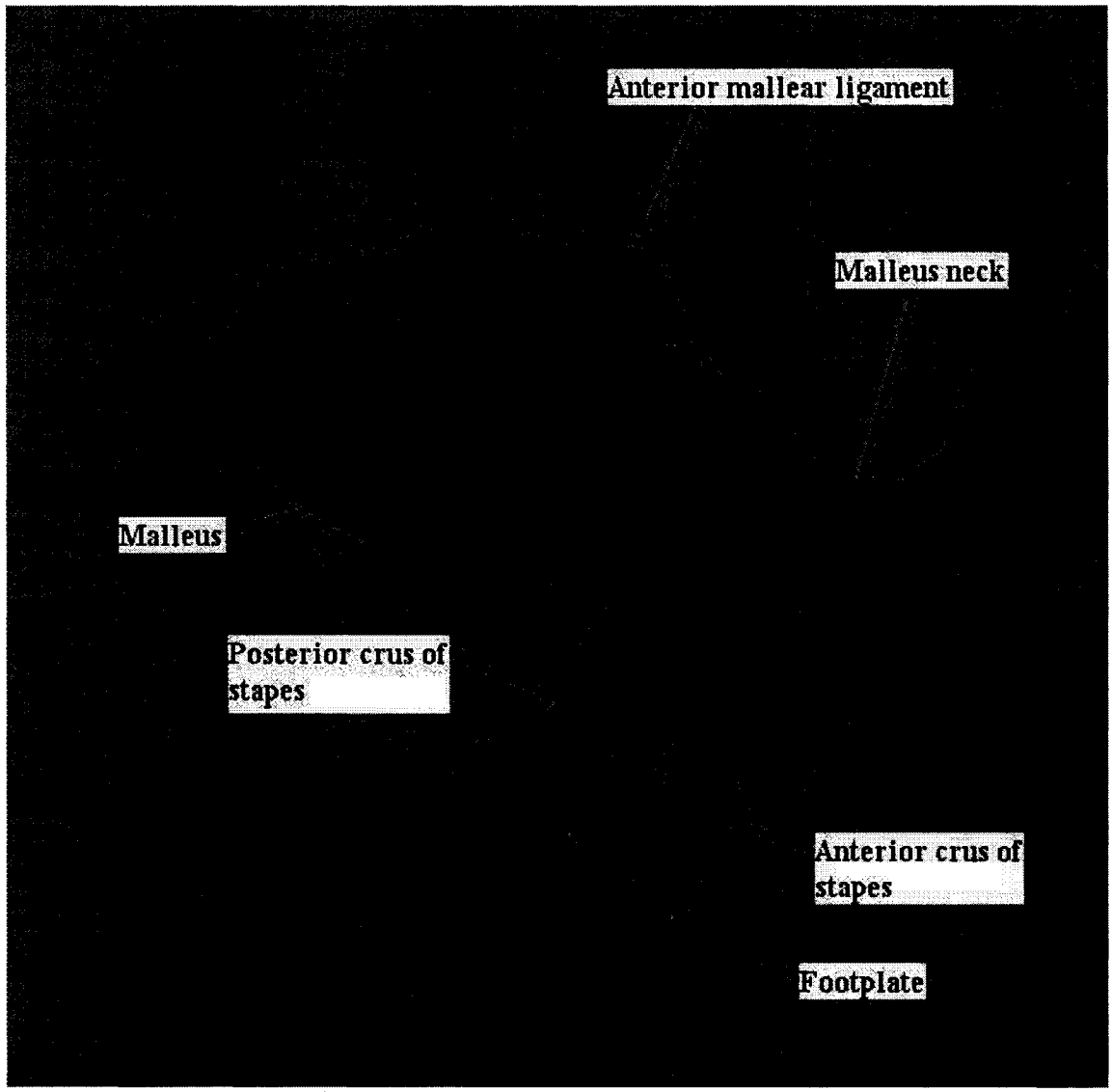

Figure 7.11: *Anterior view of the ossicles (TM and manubrium omitted for clarity) showing the axis of rotation through the anterior mallear ligament.*

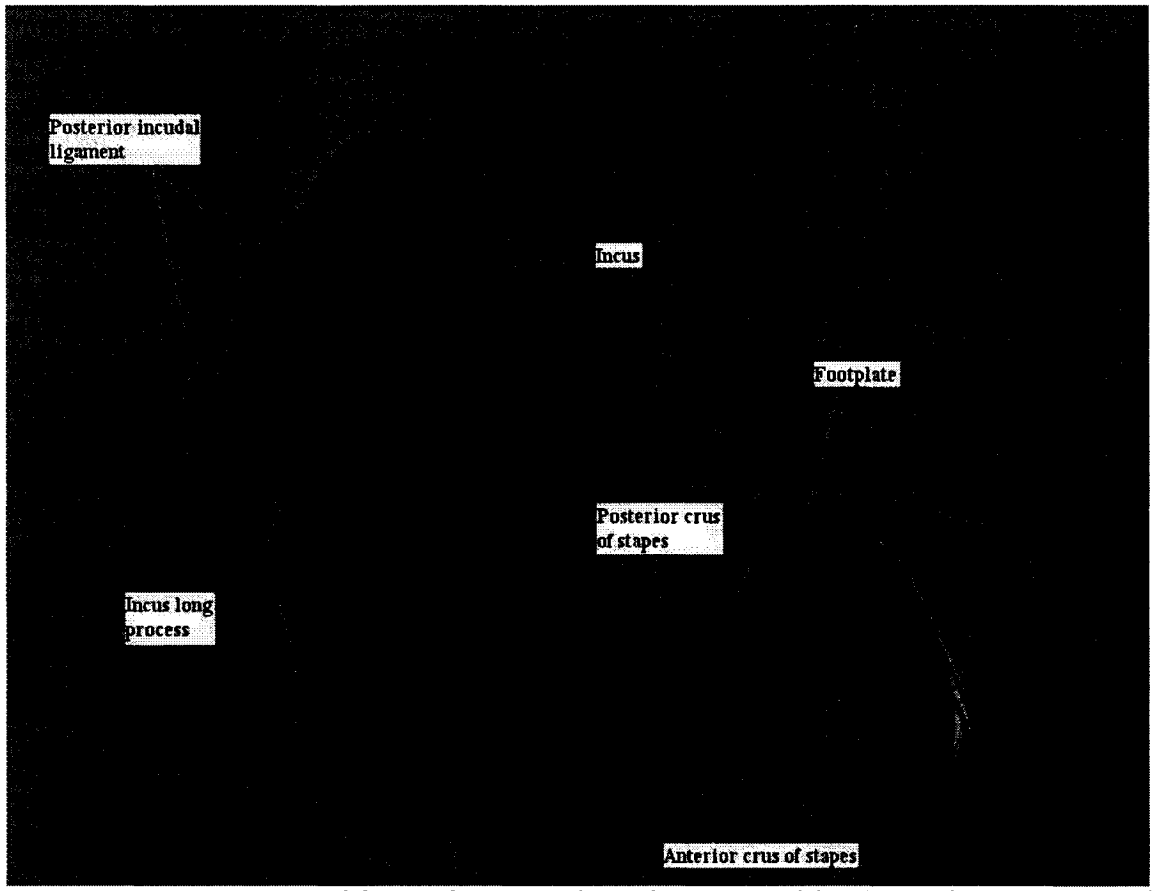

Figure 7.12: *Posterior view of the ossicles (TM and manubrium omitted for clarity) showing the axis of rotation between the two bundles of the posterior incudal ligament.*

7.4.4 Pedicle

Figure 7.13 shows a close-up of the incus long process and lenticular process, and the pedicle between them. The ossicular rotation is clearly evident when observing the displacement vectors across the incus long process.

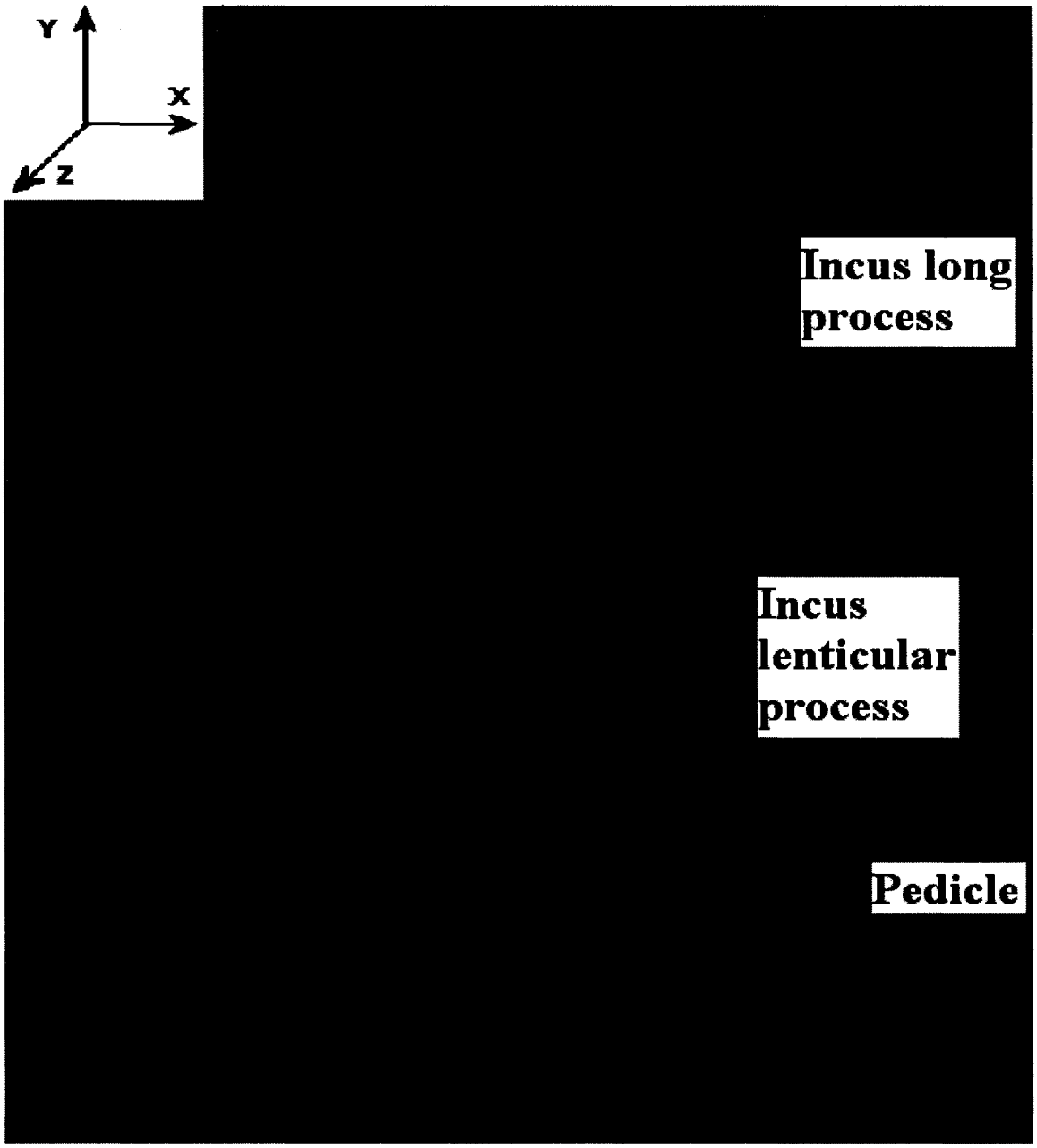

Figure 7.13: *VRML model showing the displacement vectors of a section of the ossicles, including the incus long process, the pedicle and the incus lenticular process. The orientations are the same as in Figure 7.12.*

Figure 7.14 shows only the pedicle, with the displacement vectors. The maximum and minimum vector magnitudes of the pedicle are 36 nm (at the anterior edge) and 33 nm (at the posterior edge). This represents only an 8.4% difference. In relation to the pedicle's very small dimensions relative to the overall ossicular dimensions, however, the difference is quite significant. It is difficult to determine whether this is mainly the effect of motion of the ossicles or of flexibility of the pedicle.

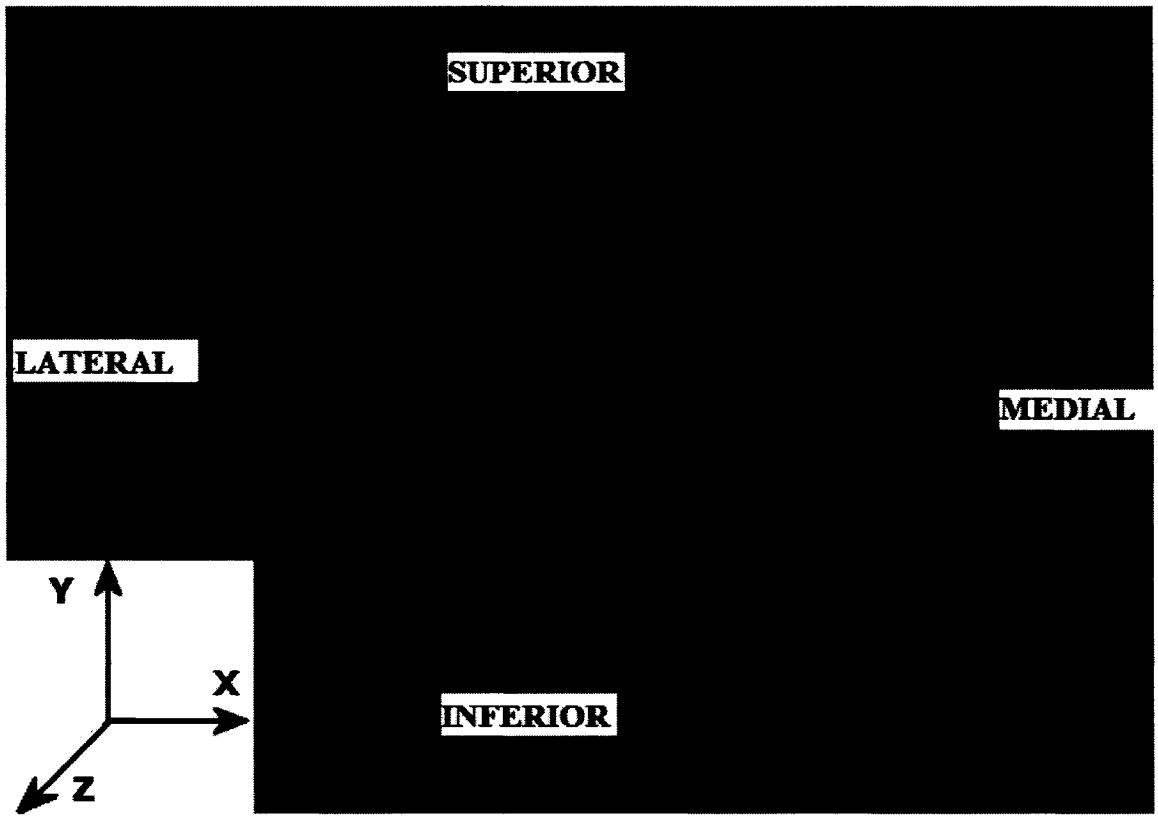

Figure 7.14: *VRML model of the pedicle. The anterior side is in the +z direction, and the posterior side is in the -z direction. The orientations are the same as in Figure 7.12.*

7.4.5 Stapes footplate displacements

Figure 7.15 shows the displacement pattern on the stapes footplate. The displacements are almost completely uniform across the footplate, as indicated by a homogeneous beige colouring. The difference between the maximum and minimum footplate displacements is only 0.24%. This implies a piston-like motion of the stapes, as also observed in Figures

7.11 and 7.12.

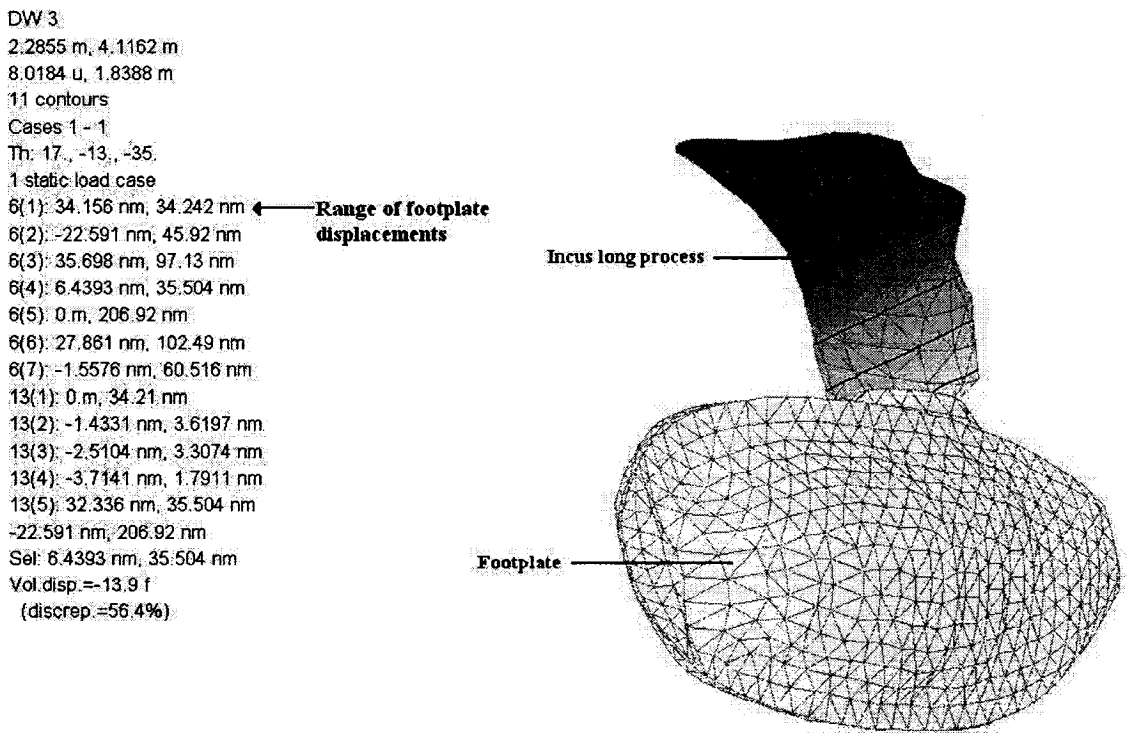

Figure 7.15: *The displacement pattern across the footplate is uniform, confirming the piston-like motion of the stapes.*

7.5 Sensitivity analysis

A series of sensitivity tests is performed to evaluate the significance of certain parameters in the finite-element model. The parameters investigated were: (1) the thicknesses of the pars flaccida and pars tensa (*Tpf* and *Tpt*, respectively) and (2) the Young's moduli of the pars flaccida, pars tensa, stapedial annular ligament, anterior mallear ligament, posterior incudal ligament and pedicle (*Ypf, Ypt, Ysal, Yaml, Ypil* and *Yped,* respectively). All the displacement values that will be shown are vector magnitudes. The effects on the footplate displacements will be examined first, followed by the effects on the TM and on the umbo. These are measures of middle-ear output (footplate) and input (TM and umbo), and are commonly measured experimentally. The effects on the umbo-to-stapes ratio and the TM-to-umbo ratio will also be presented; these two ratios may be taken as measures

of the ossicular lever ratio and of the coupling between the eardrum and the manubrium, respectively (cf. Chapter 3). Finally, the effects of the anterior mallear ligament and posterior incudal ligament on the axis of rotation will be examined. Such tests attempt to distinguish the highly influential parameters, whose values must be carefully chosen, from those whose values have little effect on the model's behaviour.

7.5.1 Stapes footplate displacements

The sensitivity of the model to its eight parameters is shown in Figure 7.16. Values for each parameter range from 0.1 times to 3 times its nominal value. All curves are monotonic over this range. Overall, as expected, the displacements get smaller as the model gets stiffer.

Excluding *Yaml*, when the parameters are decreased by a factor of 10 the footplate displacements are increased by 13% (*Ypil*) to 42% *(Yped)*. When the same parameters are increased by a factor of 3, footplate displacements are decreased by 13% (*Ypil*) to 55.5% (*Tpt*). For parameter *Yaml*, footplate displacements are increased by only 0.6% at a ratio of 0.1, and decreased by only 1.7% at a ratio of 3.

Overall, *Yaml* has very little effect on the footplate. The stapes annular ligament (*Ysal*) has a greater influence on the footplate displacements than do the anterior mallear ligament (*Yaml*) and posterior incudal ligament (*Ypil*). A question arises whether *Yaml* and *Ypil* may affect the axis of rotation without much affecting the footplate displacement. This will be further discussed in Section 7.5.6.

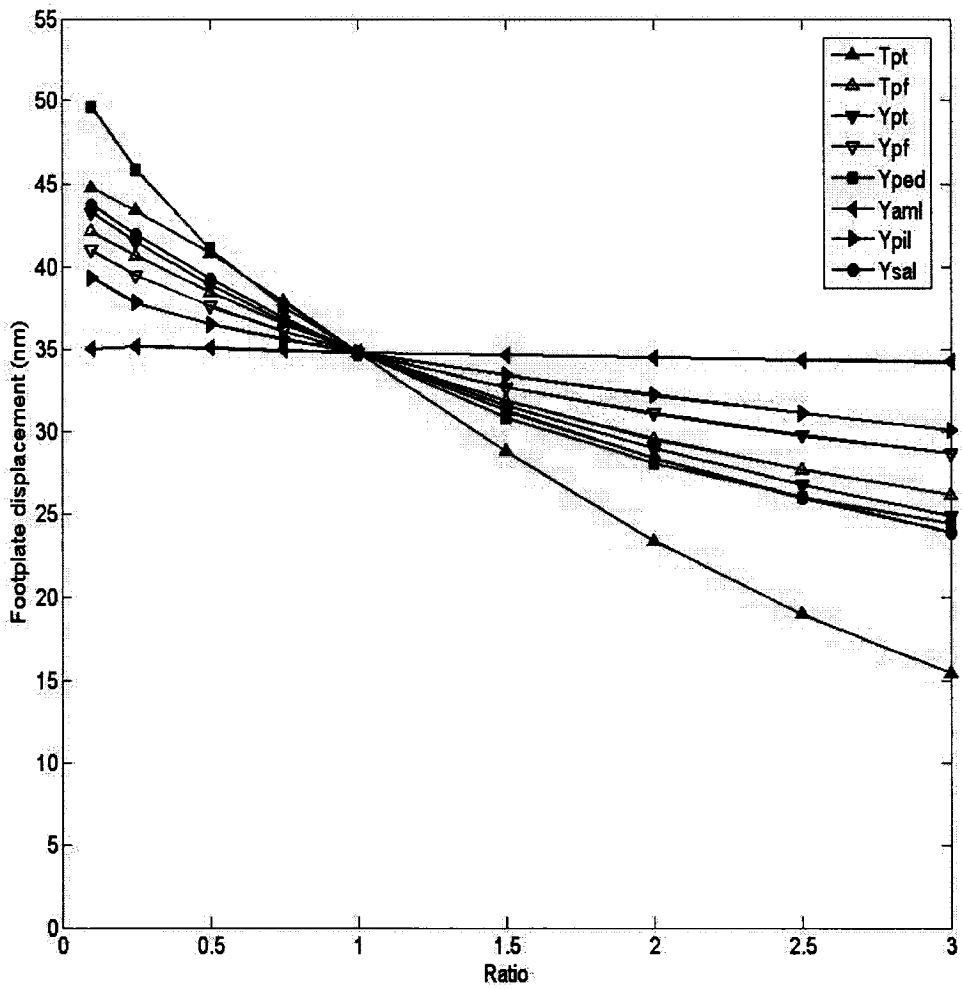

Figure 7.16: *Sensitivity of the footplate displacement to all eight parameters. The Young's modulus (Ypt & Ypf) and thickness (Tpt & Tpf) parameters of the TM are in black and red, respectively. The ligament parameters (Ysal, Ypil and Yaml) are in blue and the pedicle Young's modulus parameter (Yped) is in fuchsia.*

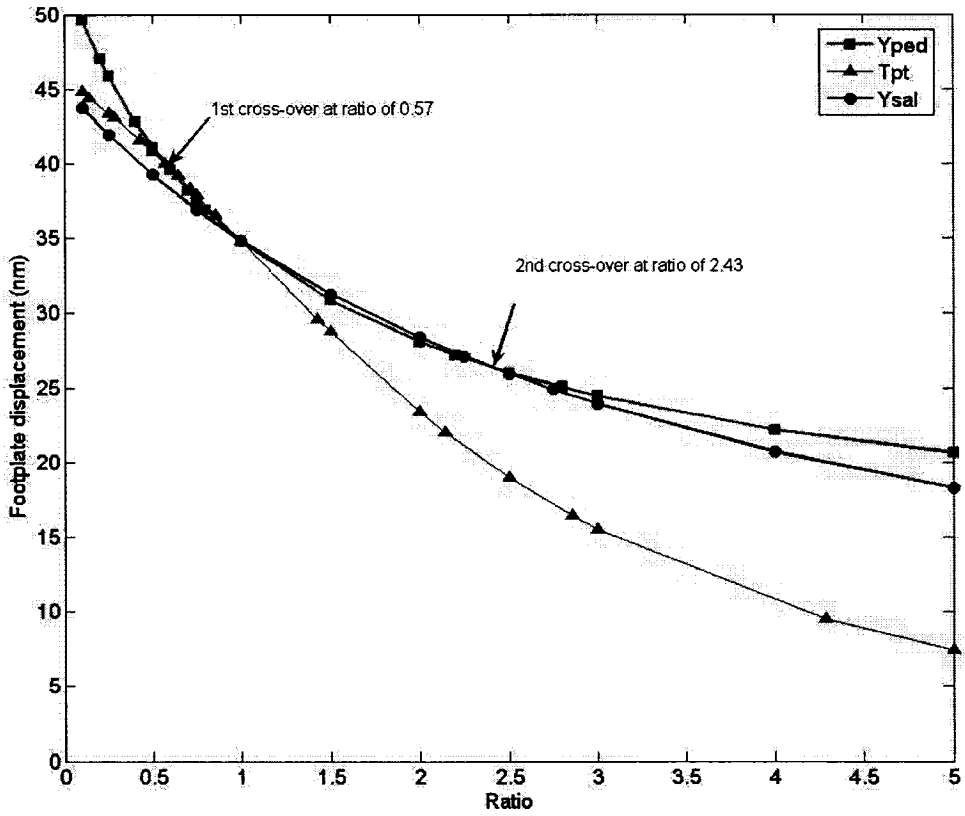

Figure 7.17: *Sensitivity of the footplate to three parameters (Yped in fuchsia, Tpt in red, and Ysal in blue). Parameter values ranged from 0.1 times to 5 times the nominal value. This plot is a clearer display of the three same curves from Figure 7.14.*

Figure 7.17 includes only parameters *Yped*, *Tpt* and *Ysal* but across a wider range of values, in order to clarify their relative influences. At a ratio of about 0.57, there is a cross-over point below which the effect of *Yped* on the footplate displacements is greater than the effect of *Tpt* or any other parameter. There is another cross-over point at a ratio of about 2.48, beyond which the effect of *Yped* is less than those of both *Ysal* and *Tpt*.

In a 3-D finite-element model of a cat middle ear, Ghosh & Funnell (1995) represented the ossicles with a fixed axis of rotation, and a simple flexible coupling between the incus

and the stapes provided a preliminary implementation of joint flexibility. The incudostapedial joint stiffness was varied from very small to very large values, and the footplate displacements were determined. Their results are shown in Figure 7.18. Footplate displacement drops for very low stiffness, because soft incudostapedial coupling does not transmit force well. As the incudostapedial stiffness increases, footplate displacement reaches a peak, then drops slightly and stabilizes at a constant value.

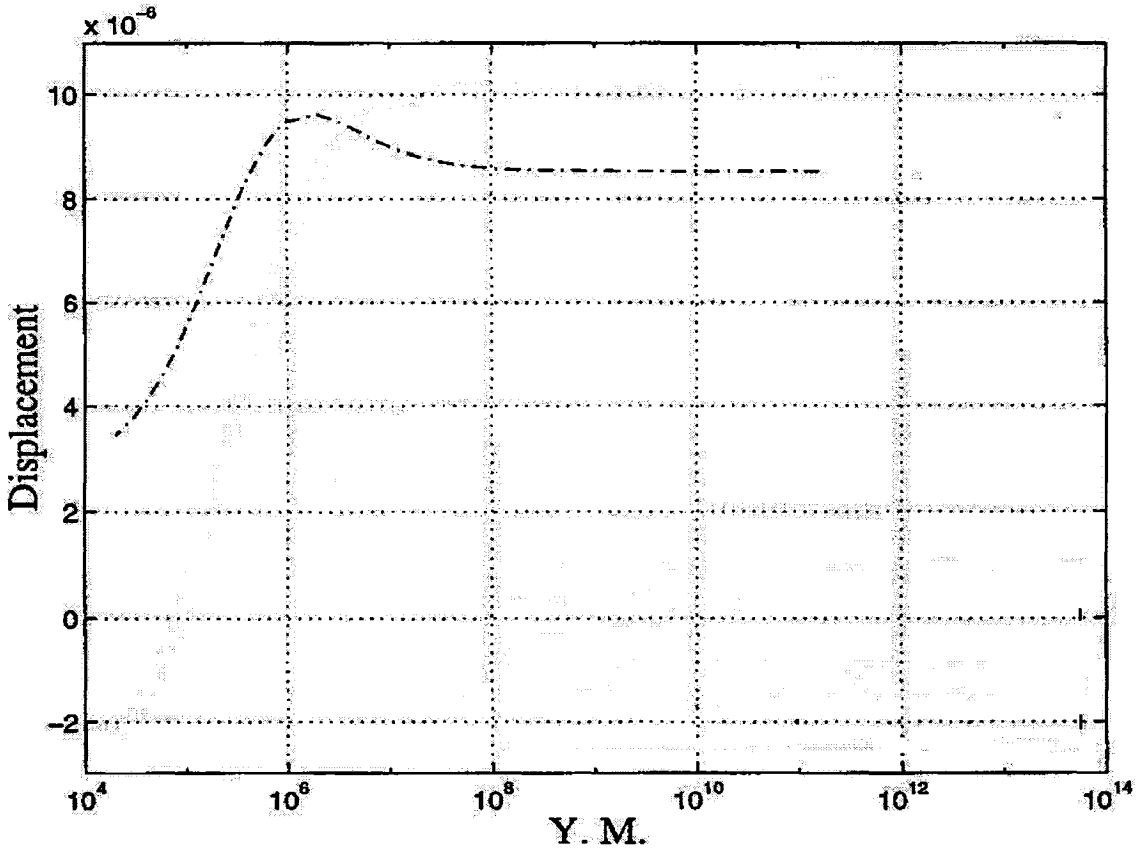

Figure 7.18: *Out-of-plane displacements of the footplate, with varying incudostapedial joint stiffness, at two points on the footplate: anteriorly (filled curve) and posteriorly (dotted curve). (Modified from Ghosh & Funnell, 1995)*

In order to look for a similar phenomenon, we decided to vary the stiffness of the pedicle to extreme values. The results are shown in Figure 7.19. Figure 7.20 shows the same results with the pedicle stiffness ratio on the x-axis.

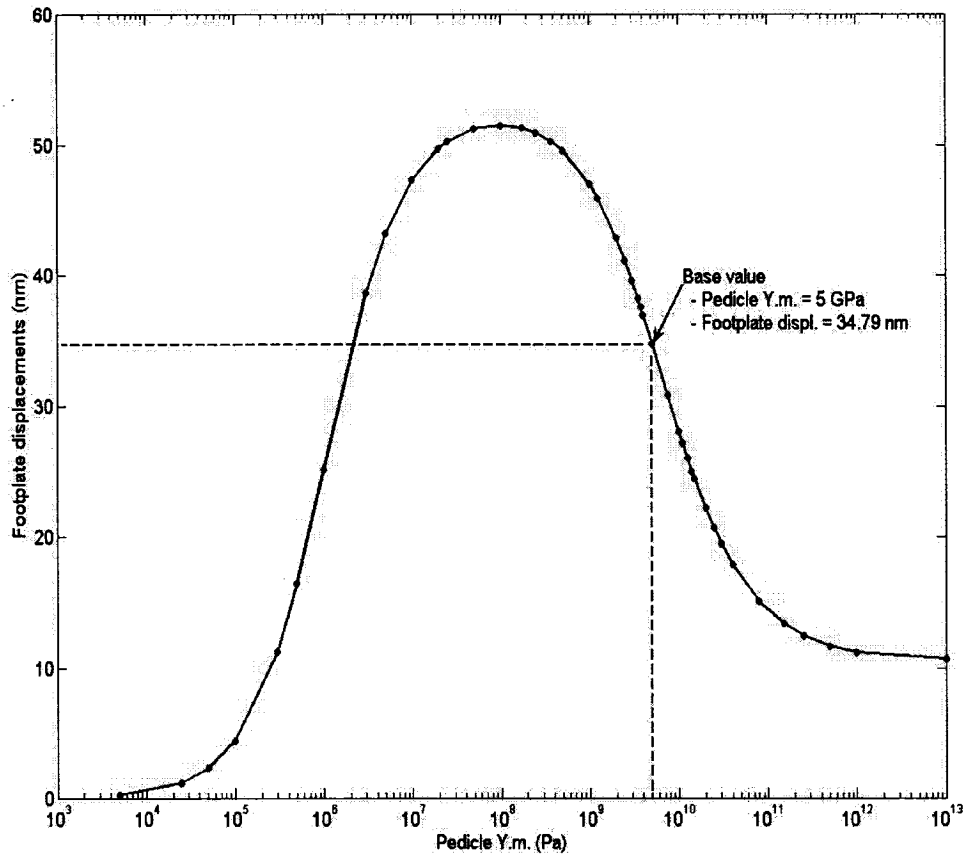

Figure 7.19: *Maximum footplate displacements with varying pedicle Young's modulus. The x-axis has a logarithmic scale.*

Figures 7.18 and 7.19 show similarities at all stages of the curve. As the stiffness decreases, footplate displacements approach zero. Footplate displacements increase as the stiffness of the joint (Figure 7.18) or pedicle (Figure 7.19) increases. At a certain stiffness value, the curves reach a peak before dropping. In both figures, as the joint stiffness is increased to extreme values, footplate displacements reach constant values. This means that the joint is so rigid that any further increase would have a negligible influence on the footplate displacements. At the base value, the displacement depends strongly on *Yped*, because of the high slope of this section of the curve.

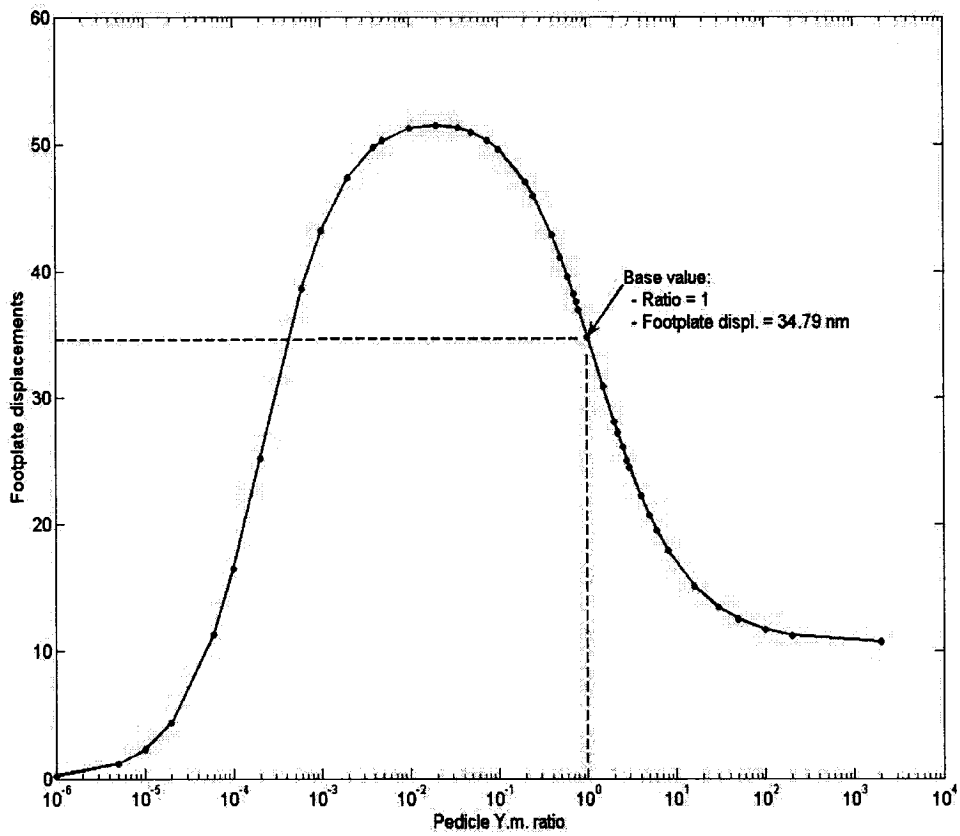

Figure 7.20: *Maximum footplate displacements with varying ratio of pedicle Young's modulus over the base value of the pedicle Young's modulus. The x-axis is in logarithmic scale.*

7.5.2 Pars Tensa displacements

The parameters with the greatest effects on the pars tensa (PT) displacement are the Young's modulus (*Ypt*) and thickness (*Tpt*) of the PT itself (Figure 7.21). When *Tpt* and *Ypt* are decreased by a factor of 10, PT displacements are increased by a factor of about 37 and 5, respectively. When the same parameters are increased by a factor of 3, PT displacements are decreased by about 67% and 42%, respectively. The remaining six parameters have relatively little (*Yped*, *Ypf*, *Tpf* and *Ysal*) or negligible (*Yaml* and *Ypil*) influence. When *Yped*, *Ypf*, *Tpf* and *Ysal* are decreased by a factor of 10, PT displacements are increased by about 23%, 12%, 15% and 24%, respectively. When they are increased

by a factor of 3, PT displacements are decreased by 26%, 16%, 21% and 23%, respectively. When *Yaml* and *Ypil* are decreased by a factor of 10, PT displacements are increased by only about 0.7% and 2%, respectively. When they are increased by a factor of 3, PT displacements are decreased by 0.7% and 8%, respectively.

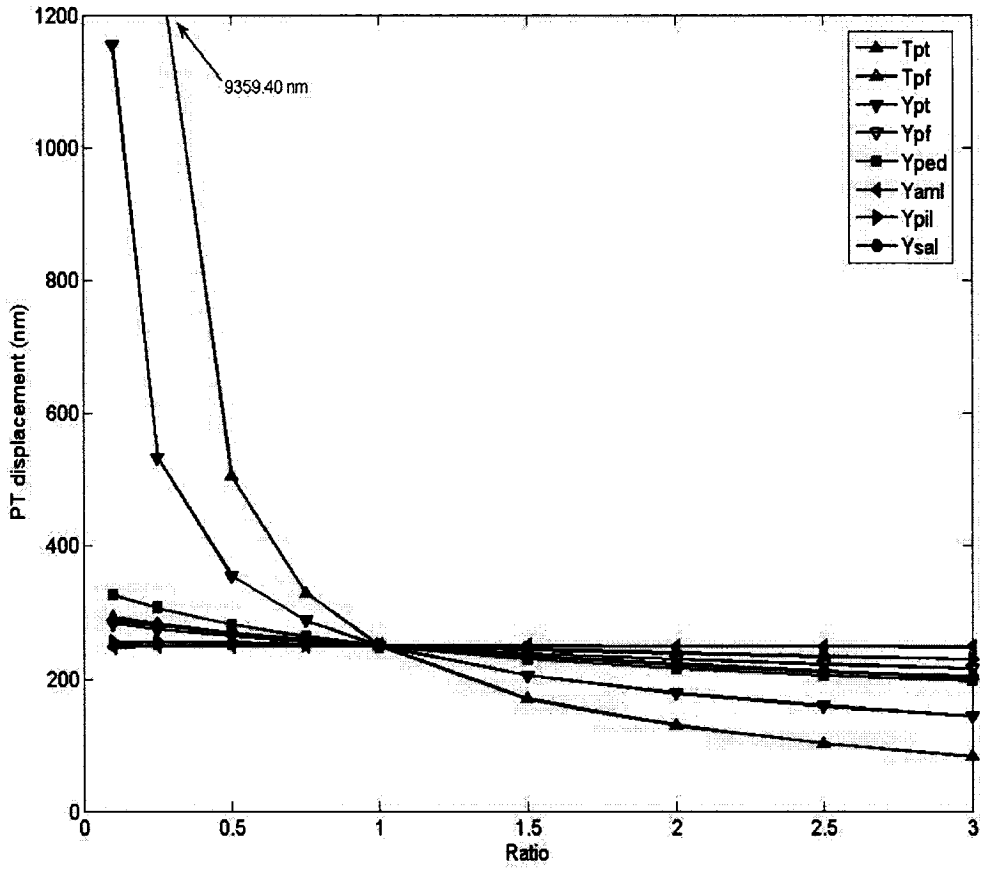

Figure 7.21: *Sensitiviy of the pars tensa to all eight parameters. The scheme is identical to the one used in Figure 7.16.*

Figure 7.21 shows that the stiffness of the pars tensa is influenced more by its thickness than by its elastic modulus. Figure 7.22 shows the effects of *Ypt* and *Tpt* with logarithmic scales.

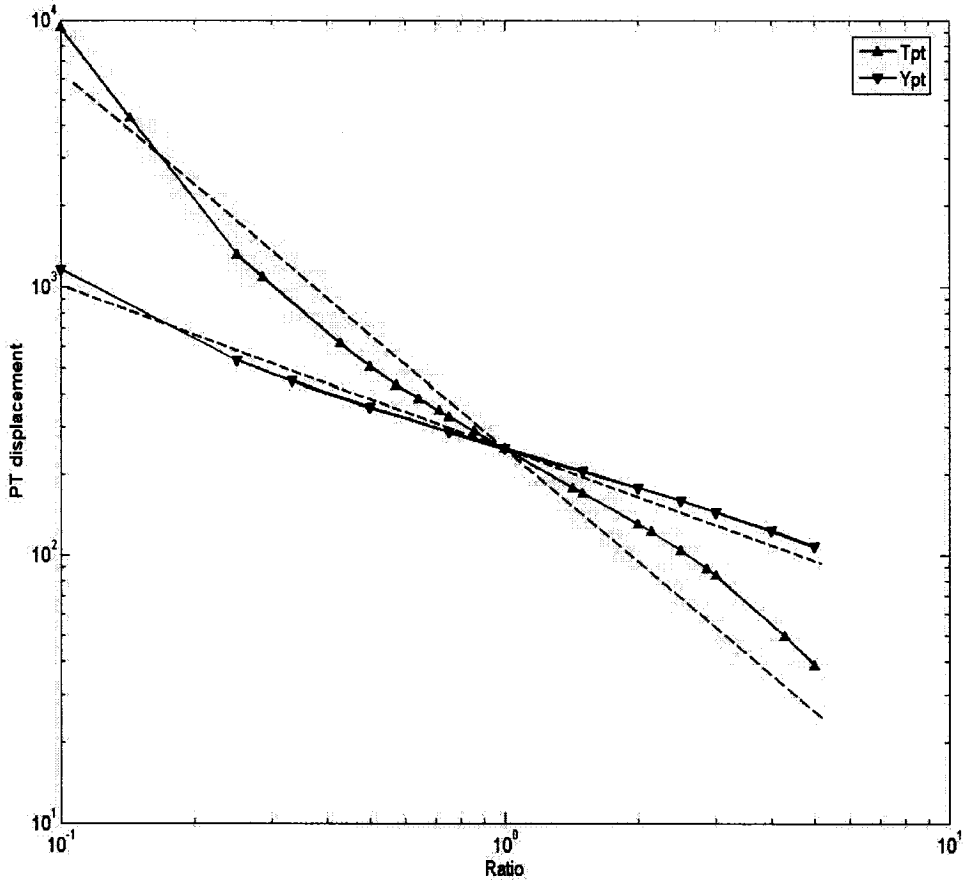

Figure 7.22: *Comparison between Ypt and Tpt, and their influence on the displacements of the pars tensa. Both axes are in logarithmic scales. The black dashed line represents a line of slope -1. The red dashed line represents a line of slope -3.*

There is an approximately linear relationship between the logarithm of the parameter ratio and the logarithm of the pars-tensa displacements, for both *Ypt* and *Tpt*. A linear curve on a log-log plot corresponds to an exponential equation of the form:

$$y = a\,x^{b}$$

where b is the slope of the curve.

In classical thin-plate theory, the out-of-plane displacement w of a thin plate is described as:

$$D\nabla^4 w = p$$

where p is the distributed load (force per unit area) acting in the same direction as w, and D is the bending rigidity of the plate defined as:

$$D = \frac{Et^3}{12(1-\nu^2)}$$

where E is the Young's modulus of the plate material, ν is the Poisson's ratio, and t is the thickness of the plate. As we can see, the thickness is cubed. The thickness thus has more effect on the stiffness than does the elastic modulus.

In Figure 7.22, two dashed straight lines (one black and one red) are superimposed on the two other curves. They represent slopes of 1 (black curve) and 3 (red curve). The *Ypt* black curve and *Tpt* red curve almost match the black dashed line and the red dashed line, respectively. The slopes of 3 and 1 for the red and black curves, respectively, indicate that the eardrum's behaviour is similar to the vibration of a thin plate and suggest that the eadrum's behaviour is dominated by bending stiffness rather than by in-plane stiffness.

7.5.3 Umbo displacements

The sensitivity of the umbo to the same 8 parameters is shown in Figure 7.23. There is relatively little difference between the influences of the various parameters on the umbo and their influences on the footplate. The most noticeable difference from Figure 7.16 is that here *Yaml* has a small influence on the umbo at low ratios. When *Yaml* is decreased by a factor of 10, umbo displacements are increased by about 4.3%.

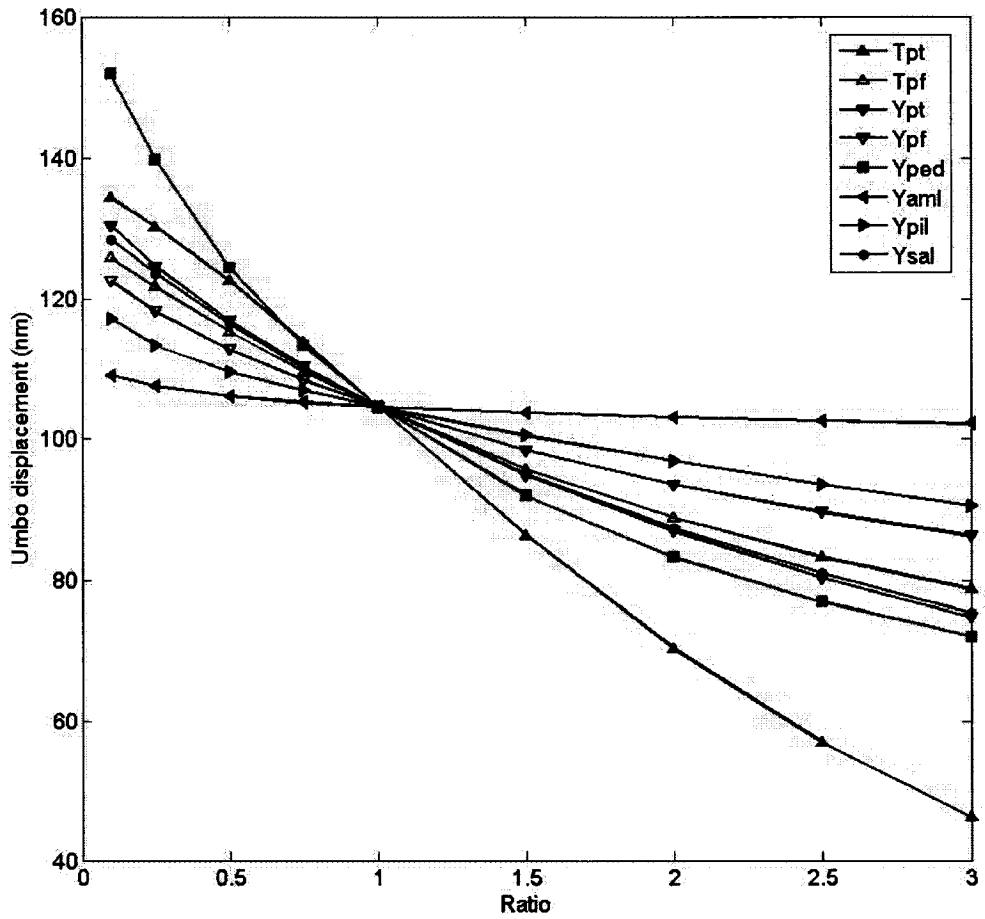

Figure 7.23: *Sensitivity of the umbo displacement to all eight parameters at 0.1, 0.25, 0.5, 0.75, 1.5, 2, 2.5 and 3 times their nominal values.*

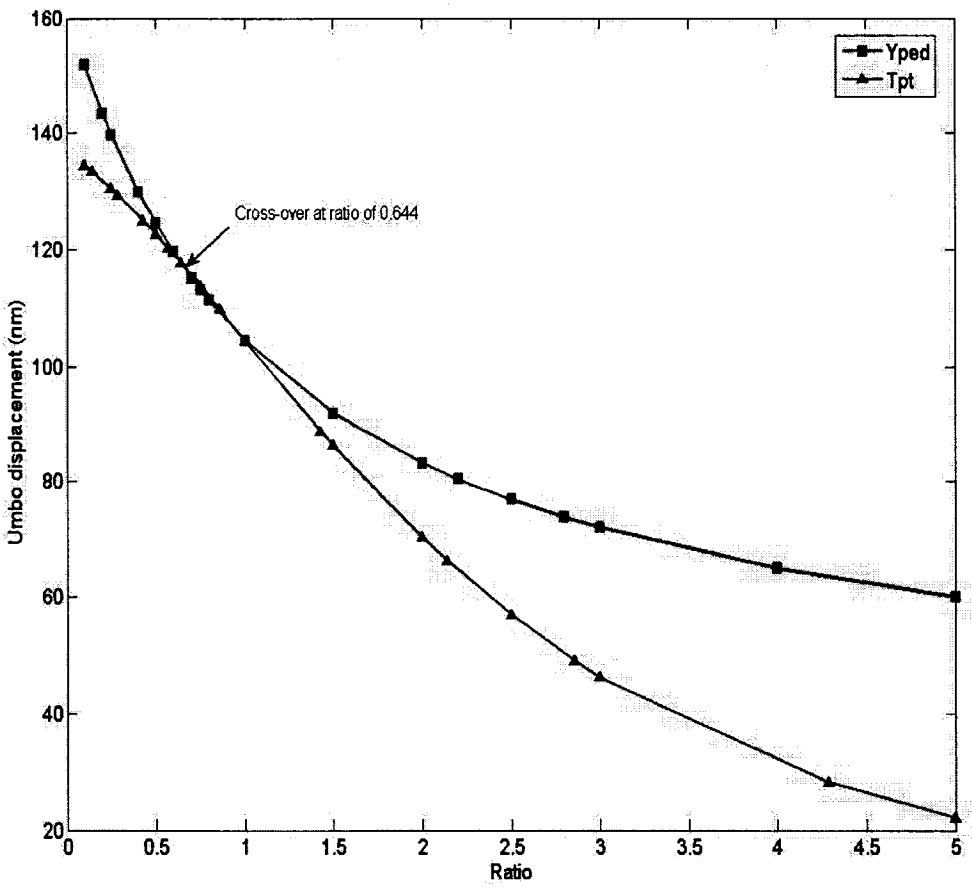

Figure 7.24: *Sensitivity of the umbo to Yped and Tpt. X-values ranged from 0.1 times to 5 times the nominal value. This plot is a clearer display of the two same curves from Figure 7.21.*

Figure 7.24 includes only parameters *Yped* and *Tpt* but across a wider range of values, in order to clarify their relative influences. At a ratio of about 0.64, there is a cross-over point below which the effect of *Yped* on the footplate displacements increases faster than the effect of *Tpt* and any other parameter. The second cross-over point is the base value at a ratio of 1.

7.5.4 Ossicular ratio

As a measure of the ossicular lever ratio, we calculated the ratio of the umbo

displacement to the stapes displacement (U/S) for each parameter (Figure 7.25). The vertical scale is expanded because, as mentioned in the previous section, there is very little difference between the influences of the various parameters on the umbo and their influences on the footplate.

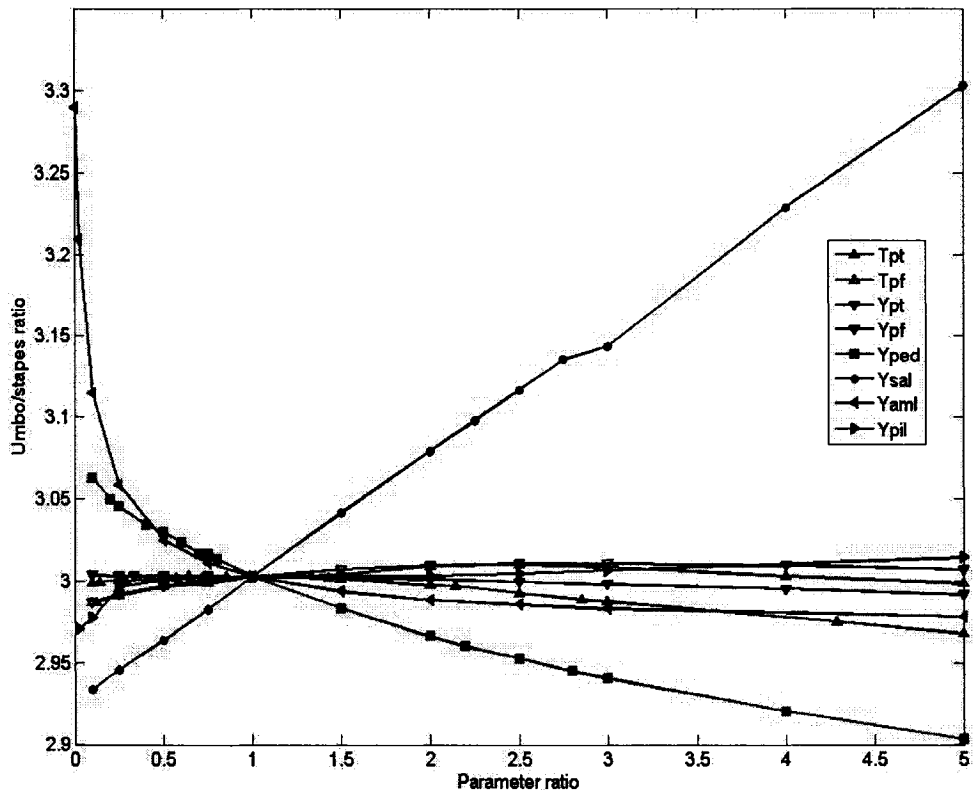

Figure 7.25: *Effect of each parameter on the umbo-to-stapes ratio, as a measure of ossicular ratio.*

When the stapes annular ligament is stiffened, the stapes footplate displacements are decreased (with little effect on the TM), and the U/S ratio evidently increases. *Yaml* has a significant effect on the U/S ratio for values below the nominal value. When the stiffness of the anterior mallear ligament decreases, the malleus is less constrained and lateral motions appear. Lateral motions are not so effective in transferring loads across the ossicles. Hence, stapes footplate displacements decrease, and the U/S ratio increases. This will be further discussed in Section 7.5.6.

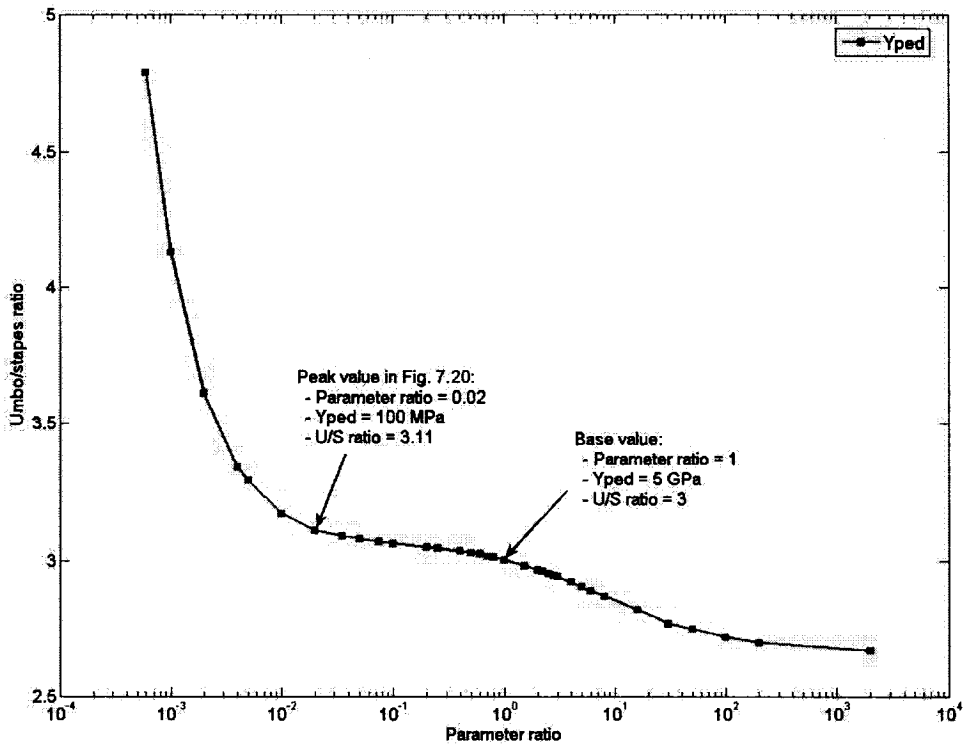

Figure 7.26: *Sensitivity of the umbo/stapes ratio to Yped. X values ranged from 0.0006 to 2000 times the base value.*

In order to look for effects related to those shown in Figure 7.20, the *Yped* curve of Figure 7.25 is shown in Figure 7.26 across a wider range of values. The ratio of 0.02 represents the *Yped* parameter ratio value corresponding to the peak of the footplate-displacement curve in Figure 7.20. When the ratio is increased beyond 0.02, the U/S ratio decreases until it reaches a constant value. This behaviour is similar to that in Figure 7.20. As the ratio is decreased below 0.02, the footplate displacements decrease to zero, which explains the sharp increase of the U/S ratio in Figure 7.26.

All other parameters had little effect on the U/S ratio.

7.5.5 TM-manubrium coupling

As a measure of the coupling between the eardrum and the ossicles, we calculated the PT-to-umbo (PT/U) ratio for each parameter (Figure 7.27).

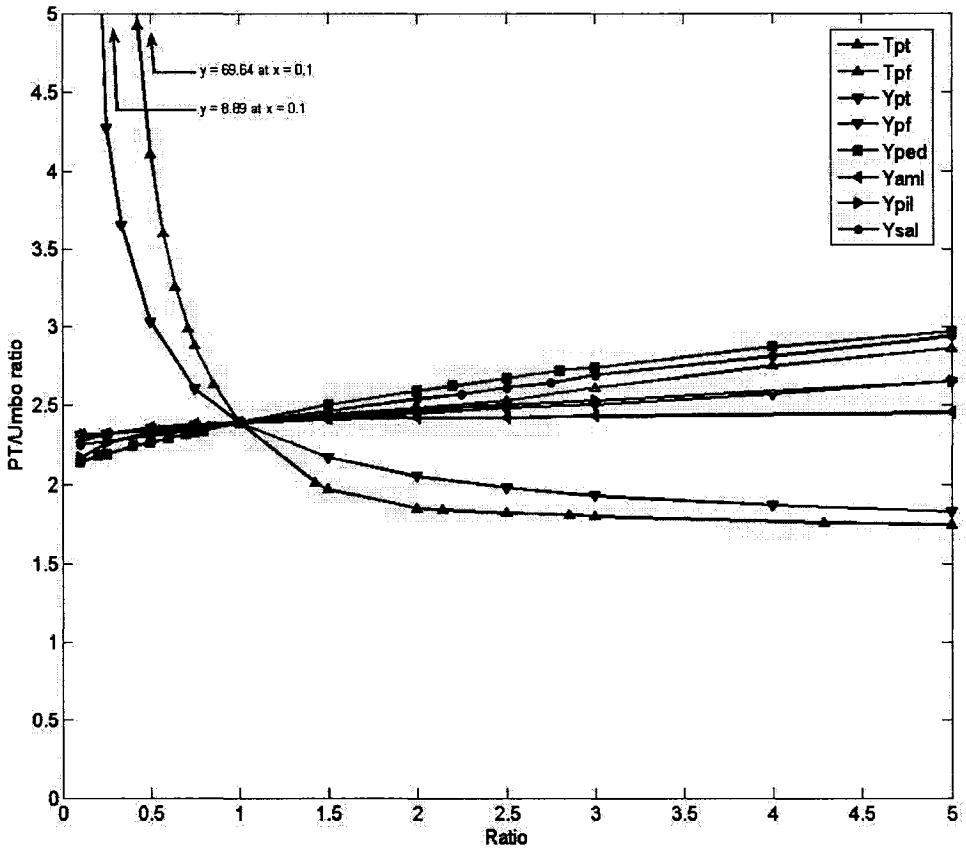

Figure 7.27: *Effect of each parameter on the PT-to-umbo ratio, as a measure of the coupling between the eardrum and the ossicles.*

When *Tpt* and *Ypt* are decreased by a factor of 10, the PT/U ratio is increased by a factor of about 28 and 2, respectively. For the other six parameters, the PT/U ratio is decreased by only about 3% (*Tpf*) to 10% (*Yped*).

When *Tpt* and *Ypt* are increased by a factor of 5, the PT/U ratio is decreased by about 27% and 23%, respectively. For the other six parameters, the PT/U ratio is increased by about 2% (*Yaml*) to 13% (*Yped*).

Ypt and *Tpt* on the one hand, and the remainning six parameters on the other hand, have opposite effects. As the eardrum becomes very stiff, it and the manubrium are relatively unaffected by the rest of the middle-ear system; the PT/umbo ratio decreases and approaches a constant. From another standpoint, as the ossicular system is stiffened, the manubrium becomes nearly fixed; the umbo displacements decrease and the PT/umbo ratio increases.

7.5.6 Axis of rotation

In an attempt to understand how the apparent axis of rotation is influenced by the anterior mallear ligament (AML) and posterior incudal ligament (PIL), we ran simulations on the model for six different cases (see Figure 7.28):

- A: AML and PIL are kept intact
- B: both the AML and PIL Young's moduli are set to zero
- C: only the AML Young's modulus is set to zero
- D: only the PIL Young's modulus is set to zero
- E: only the AML Young's modulus is increased by a factor of 10 (i.e., 200 MPa)
- F: only the PIL Young's modulus is increased by a factor of 10 (i.e., 200 MPa)

In case A, we can see (as described previously) that the apparent axis of rotation passes through the AML and PIL.

When both the AML and PIL have zero Young's modulus (case B), the axis of rotation is shifted completely to the left of the figure (not visible). The parallel contour lines indicate the direction of the axis of rotation. Footplate and umbo displacements are increased by about 46% and 29%, respectively. The umbo-to-stapes (U/S) ratio is decreased by about 12%.

When the AML's Young's modulus is set to zero (case C), the anterior end of the axis of rotation is shifted to the left of the AML, and the axis still passes through the PIL. Footplate displacements are decreased by only about 3%, and umbo displacements are increased by about 7%. The U/S ratio is increased about 10%.

In case D, when the PIL's Young's modulus is set to zero, the posterior end of the axis of rotation is shifted slightly to the right of the PIL (clearly by a lesser amount than in case C), and the axis still passes through the AML. Footplate and umbo displacements are increased by about 18.2% and 18.0%, respectively. The U/S ratio changes by a mere 0.2%.

When the AML's Young's modulus is stiffened (case E), the axis of rotation is slightly shifted to the right at both ends. Footplate and umbo displacements are decreased by about 64.6% and 65.1%, respectively. The U/S ratio decreases by only 1.5%.

When the PIL is stiffened (case F), the anterior end of the axis of rotation is considerably shifted to the left of the AML. Footplate and umbo displacements are decreased by 99.3% and 98.7%, respectively. The U/S ratio is increased by about a factor of 2.

These results show interesting additional observations:

- When the AML is cut, we notice a big axis change but a very small change in the ossicular ratio (only a 10% increase).
- When the PIL's stiffness is increased by a factor of 10 above the nominal value, we notice a large axis change but a small change in the ossicular ratio (only a factor of 2).
- When the AML's stiffness is increased by a factor of 10 above the nominal value, there is practically no change in either the axis or the ossicular ratio.
- When the PIL is cut, we notice a very small axis change and no change in the ossicular ratio.

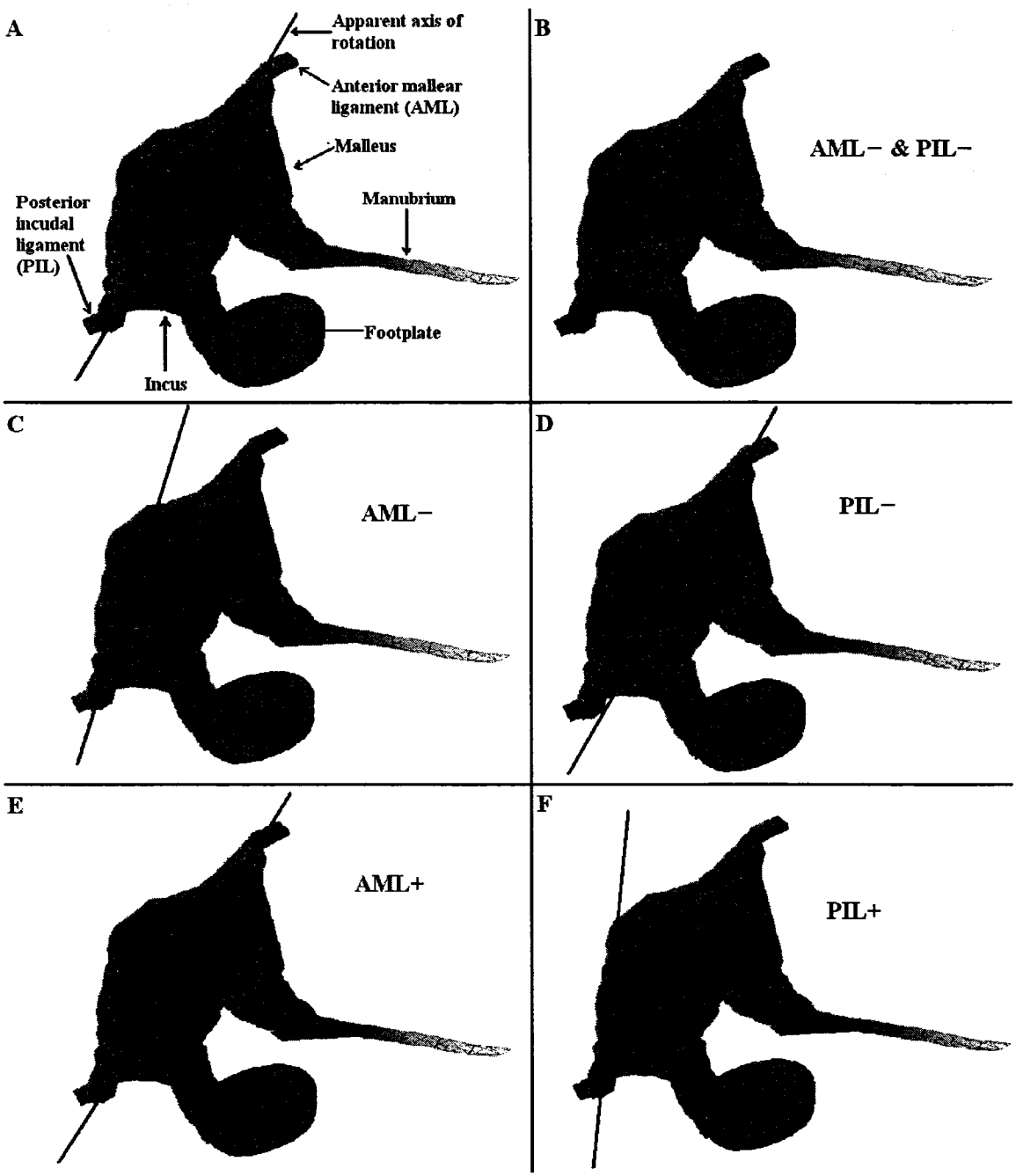

Figure 7.28: *Sensitivity of the axis of rotation to the anterior mallear ligament and the posterior incudal ligament.*

7.5.7 Eardrum shape

Funnell & Laszlo (1978) developed a finite-element model of the cat eardrum with a rudimentary middle-ear part. The shape of the eardrum was defined by a normalized radius-of-curvature parameter. They varied the depth of the cone of the eardrum and the degree of curvature and showed that the shape of the eardrum has a significant influence on middle-ear mechanics. In this section, we present preliminary results on the effects of changing the eardrum shape of our model by presenting just one additional TM shape.

The Fad software, a finite-element preprocessor developed in our lab by Dr. W.R.J. Funnell, was used to modify the shape of the eardrum by relaxing the nodal coordinates. Each node on the eardrum is moved in turn to the position which is the average of the positions of all the nodes to which it is connected. The same process is repeated until none of the nodes moves more than some threshold.

Figure 7.29 shows the eardrum segmented from the MR data (A) and the newly shaped eardrum (B), in side and front views, as well as their displacement patterns. The displacement pattern in A is the same as in Figure 7.9. In B, two areas of maximum displacement are displayed. They are further away from the manubrium and closer to the annular ring than they are in A. The maximum displacement in B appears in the posterior region, as in A. Maximum TM displacement increased from about 250 nm (A) to about 334 nm (B), umbo displacement decreased from about 105 nm (A) to about 40 nm (B), and stapes displacement decreased from about 35 nm (A) to about 13 nm (B). The U/S ratio is almost identical in A and B. The PT/U ratio, however, increased from 2.4 (A) to 8.4 (B), demonstrating that the shape of the eardrum has a significant effect on middle-ear mechanics.

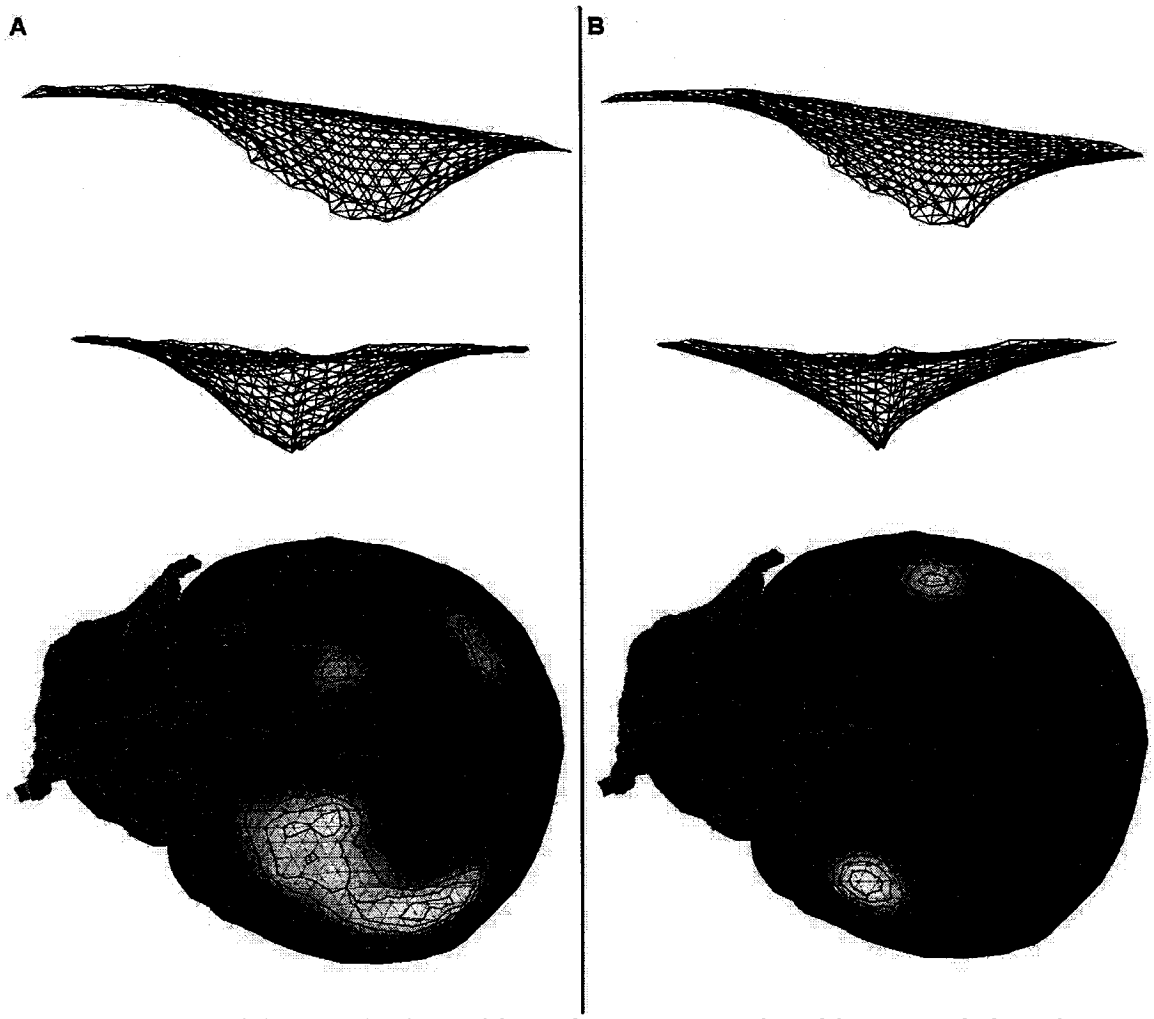

Figure 7.29: *Effect of changing the shape of the eardrum. A: TM in side and front views, before relaxing the shape. B: TM in side and front views after relaxing the shape.*

7.6 Comparison with experimental measurements

To validate our model, it is necessary to compare its behaviour with experimental data. Our gerbil middle-ear model has no inertial or damping terms, and therefore corresponds to low acoustic frequencies.

7.6.1 Eardrum measurements

Von Unge *et al.* (1993) assessed the shape of the gerbil eardrum and measured its displacement patterns under static pressure with a real-time moiré interferometer. Two

points of maximum displacement were reported: one in the anterior part, slightly superior to the umbo; the second one in the posterior part, somewhat more superiorly. The larger of the two was in the posterior region. As shown in Figure 7.9, these findings are in very good qualitative agreement with the results from our TM model with respect to the positions of the points of maximum displacement. In terms of the displacements themselves, our values were expected to be different because of viscoelastic effects in their measurements, and because their pressures were very high and the displacements were non-linear.

7.6.2 Ossicular measurements

Although a number of studies have involved experimental measurements on gerbil middle ears, few have included responses below 1 kHz. Ravicz & Rosowski (1997), Overstreet & Ruggero (2002) and Overstreet *et al.* (2003) dealt exclusively with high-frequency responses. Rosowski *et al.* (1999), Olson & Cooper (2000) and Ravicz & Rosowski (2004) looked at both low and high frequencies.

Rosowski *et al.* (1999) and Ravicz & Rosowski (2004) used a probe-tube microphone and a laser Doppler vibrometer to measure stapes displacement at the posterior crus. The laser beam was focused at an angle of between 30 and 45 degrees relative to the direction of piston-like stapes translation. A cosine correction was used to adjust all measurements to a value consistent with the supposed direction of translation. Olson & Cooper (2000) used an interferometer to measure the stapes displacements.

To date there have been no measurements of gerbil TM displacements. Only Rosowski *et al.* (1999) measured displacements at (or at least near) the umbo.

The results of the low-frequency experimental studies are shown in Figure 7.30, and are summarized in Table 7.1. The figure shows a log plot of the stapes velocity results of four studies. The stapes velocity increases linearly up to about 1 kHz. The behaviour is more complex beyond 1 kHz. Only the low-frequency results (i.e., 100 Hz to 1 kHz range) will be used for comparison with our finite-element model. The results from Ravicz &

Rosowski (2004) have a variability of about 10% in the low-frequency range. We averaged the values from Rosowski *et al.* (1999), Oslon & Cooper (2000) and Ravicz & Rosowski (2004) across a frequency range of 100 Hz to 1 kHz. The data from Oslon & Cooper (2000) are from Ravicz & Rosowski (2004), because only the abstract of Oslon & Cooper (2000) is available to us. In all three studies, stapes velocities were measured at different frequencies. In order to compare with our displacement results, we converted the reported stapes velocities to displacements by dividing by the frequency.

Our footplate displacement differs from those of Rosowski *et al.* (1999) and Olson & Cooper (2000) by approximately 33% and 27%, respectively, and is almost identical to the value of Ravicz & Rosowski (2004).

The ratio of umbo displacement to footplate displacement gives an indication of the ossicular lever ratio, which is one of the factors often used to define the energy transfer mechanism of the middle ear (cf. Chapter 3). Rosowski *et al.* (1999) reported a ratio of about 3.5. In our model the ratio is 3, which agrees quite well with their value.

Displacements (nm)	**Model**	**Rosowski *et al.* (1999)**	**Olson & Cooper (2000)**	**Ravicz & Rosowski (2004)**
TM (pars tensa)	250	-	-	-
Umbo	104.5	183.8	-	-
Footplate	34.8	52.5	47.7	35

Table 7.1: *Summary of gerbil middle-ear experiments. Variability is indicated in Figure 7.25*

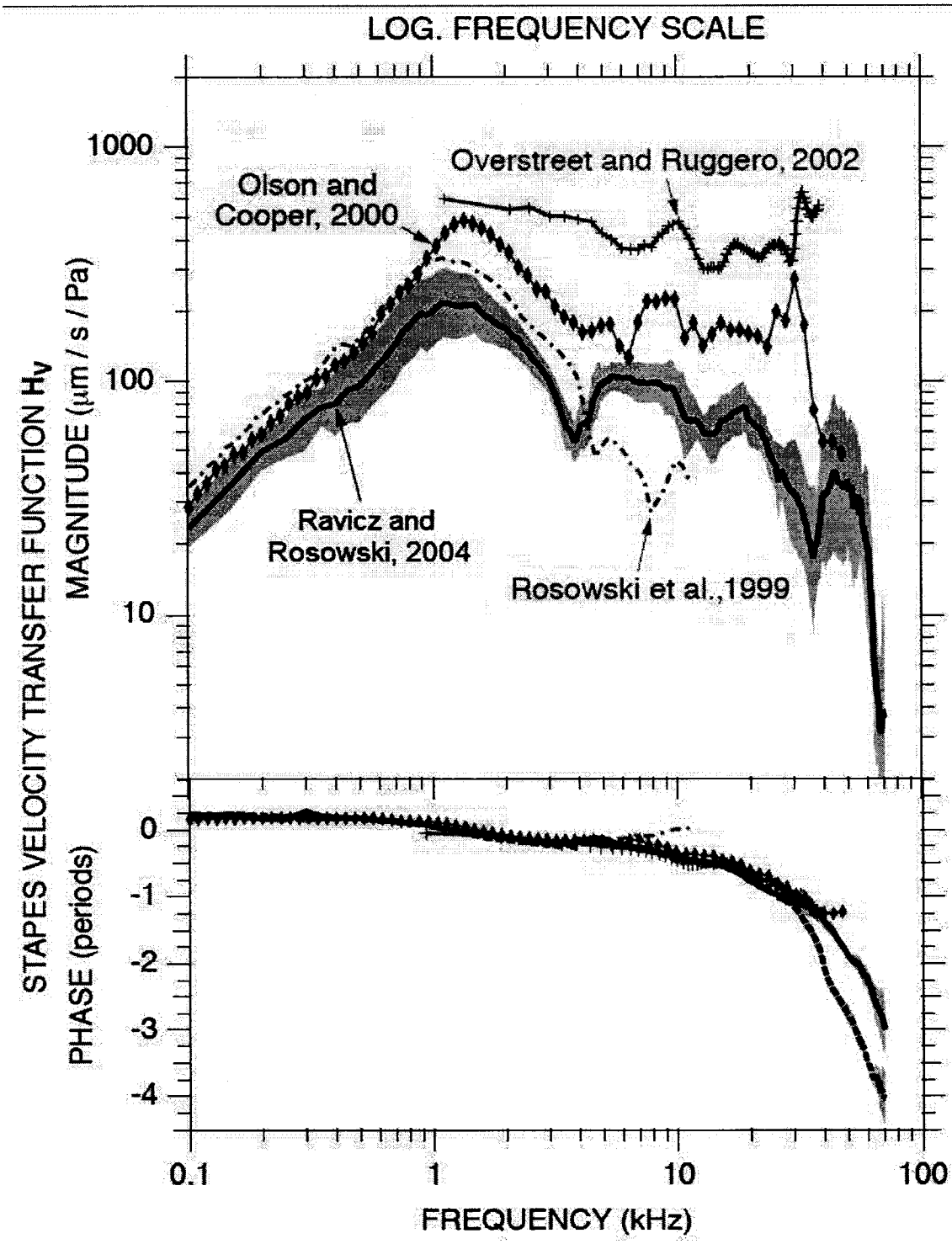

Figure 7.30: *Stapes velocity results from Ravicz & Rosowski (2004), Fig. 9, also showing other studies. Low-frequency responses are defined below 1 kHz. The transfer function Hv is the stapes velocity normalized by the ear-canal pressure (or input pressure).*

7.6.3 Ligament measurements

The apparent axis of rotation observed in our model (cf. Section 7.4.3) is similar to the classical description given in the literature for low frequencies: passing from the anterior mallear ligament (AML) to the posterior incudal ligament (PIL).

Nakajima *et al.* (2004) determined the effects of both stiffening and removing the AML and PIL on acoustic response in fresh human ossicles for frequencies below 1 kHz. Sound-induced umbo and stapes velocities were measured by laser vibrometry. Stiffening of the AML resulted in a decrease of umbo and stapes displacements by a factor of 2 or less. In our model, the umbo and stapes displacements decreased by 65% (cf. Section 7.5.6). No experimental or finite-element studies have included the effects of stiffening the PIL.

Experimental removal of the AML resulted an increase in umbo displacements of less than 60% and a change in footplate displacements of less than 30%. Removal of the PIL resulted in an increase in umbo displacements of less than 40% and a change in footplate displacements of less than 15%. In our model, when the AML's stiffness was set to zero, the umbo displacements increased by 7% and the stapes footplate displacements decreased by 3%. When the PIL's stiffness was set to zero, the umbo and stapes displacements increased by 18%.

Nakajima et al. (2004) concluded that removal of either the AML or PIL affects ossicular motion minimally at low frequencies. Large and complex changes were reported, however, when removing both the AML and PIL.

These results are qualitatively consistent with our findings in Section 7.5.6.

CHAPTER 8

CONCLUSIONS AND FUTURE WORK

8.1 Conclusions

The focus of this research was to develop a 3-D finite-element model of the gerbil middle ear with a detailed geometry based on MRI and micro-CT data, and to quantify the mechanics in response to static pressure loading. Only *a priori* material-property estimates from the literature were used, and no attempt has been made to match experimental measurements by adjusting certain parameters.

An MRM dataset with a voxel size of 45 μm (provided by Drs. MM Henson and OW Henson, Jr., and the Duke University Center for In-Vivo Microscopy) and an X-ray micro-CT dataset with a voxel size of 5 um (provided by Dr. WF Decraemer from the University of Antwerp), supplemented by histological images, are the basis for 3-D reconstruction and mesh generation. The eardrum model is based on phase-shift moiré shape measurements by Dr. WF Decraemer in collaboration with Dr. M von Unge and Dr. JJJ Dirckx. The middle-ear structures were segmented with locally developed software, based on the MRM and X-ray micro-CT datasets, and were assigned mechanical properties taken from the literature.

The final model included the tympanic membrane, the three ossicles (malleus, incus and stapes) and three ligaments (anterior mallear ligament, posterior incudal ligament and stapedial annular ligament). Particular attention was paid to the pedicle of the incus.

Preliminary results consisted of convergence tests to determine an appropriate mesh resolution for the model and a stiffness for the ossicles. Then, the final model's behaviour in response to a static pressure of 1 Pa was analysed. Finally, a series of sensitivity tests was performed to evaluate the significance of the different parameters in the finite-element model. To validate the model, the results were compared with experimental data from the literature.

The Young's modulus and thickness of the pars tensa had the greatest effect on the pars tensa displacements and, along with the Young's moduli of the pedicle and the stapedial annular ligament (SAL), on the umbo and stapes displacements. The Young's moduli of the PIL and AML had the least effect on the model. The Young's moduli of the AML, SAL and pedicle had a large influence on the ossicular ratio (umbo-to-stapes ratio), the remaining parameters having insignificant effects. The coupling between the tympanic membrane and the manubrium was found to be highly influenced by the pars-tensa parameters, and to a lesser extent by the thickness of the pars flaccida, and the Young's moduli of the pedicle and SAL. Finally, the shape of the eardrum was shown to have an effect on the displacements of the middle-ear components, and on the displacement profile of the eardrum itself.

Overall, our finite-element model demonstrates good agreement with experimental data. The displacement pattern of the pars tensa in our model is similar to profiles measured experimentally (von Unge *et al.*, 1993). The umbo and stapes displacements, as well as the ossicular displacement ratio, compare satisfactorily with low-frequency measurements from Rosowski *et al.* (1999), Olson & Cooper (2000) and Ravicz & Rosowski (2004). The predominantly piston-like motion of the stapes at low-frequencies is consistent with Rosowski *et al.* (1999). The ossicular axis of rotation extended from the anterior mallear ligament (AML) to the posterior incudal ligament (PIL), corresponding to the classical description.

The axis of rotation was influenced by the AML when it was cut, by the PIL when it was stiffened, and by both together when they were cut. These results are consistent with Nakajima *et al.* (2004).

In a finite-element model analysis (based on the human model by Koike & Wada, 2002) of stiffening the AML, by Huber *et al.* (2003), the AML's Young's modulus was increased by a factor of 1000, resulting in a Young's modulus similar to bone. Such an increase in stiffness resulted in a decrease of stapes motion by about 80% to 150%. Similarly, in our model, the umbo and stapes displacements decreased by 65% when the AML's Young's

modulus was increased by a factor of 10.

The finite-element results are significant for a quantitative understanding of middle-ear mechanics. They will contribute to understanding the effects of eardrum pathologies, designing hearing-aid transducers and middle-ear prostheses, assisting the detection of middle-ear pathology, and improving the teaching of anatomy and surgical techniques.

8.2 Future work

There are several enhancements that should be undertaken in the future in order to continue improving the model:

- This study analyzed the mechanics of the gerbil middle ear in response to static pressure loading. Dynamic analysis should be performed. The inertial and damping properties would be included in the model. In doing so, we could more completely validate our model with experimental data at frequencies within the human audible range (200 Hz to 20 kHz).
- The study should be extended to non-linear analysis. The large (non-linear) displacements would be compared with recent moiré data from Decraemer's lab (Decraemer *et al.*, 2003; Dirckx & Decraemer, 2003).
- In our study, the periphery of the eardrum was assumed fixed. A finite-element representation of the fibrocartilaginous ring (including the smooth-muscle cells) around the TM, must be included in the model. The subsequent results would be compared with the measurements of Yang & Henson (2002). In that study, cochlear microphonic thresholds were recorded to study the physiological effects of smooth muscle, by applying drugs known to relax and control smooth muscle.
- A set of different eardrum shapes should be included to study their influence on the overall behaviour of the middle ear.
- Displacement measurements of the gerbil eardrum are non-existent, and should be made. Measurements at different points along the manubrium would help to investigate the coupling between the eardrum and the malleus.
- Measurements at different locations on the stapes would be useful to understand its motion (piston-like, rocking ...) at low and high frequencies.

- Measurements at different locations on the malleus and incus would also serve to clarify the relative motion of the ossicles at different frequencies.
- Measurements at the pedicle and incudostapedial joint would help to better understand the mechanism of the coupling between the incus and the stapes.
- A more thorough representation of the pedicle, the incudomallear and incudostapedial joints, and the overall ligament/bone connection, would serve to improve our understanding of ossicular motion.
- A model of the outer ear and inner ear can be added to investigate their effects on the middle-ear behaviour.

REFERENCES

Ascenzi A & Bonucci E (1967): *The tensile properties of single osteons*. Anat Rec, 158(4): 375-386.

Ayache N (1995): *Medical computer vision, virtual reality and robotics*. Image and Vision Computing, 13 (4), 295-313.

Bast TH & Anson BJ (1949): *The temporal bone and the ear*. Cited by Wever EG & Lawrence M (1954).

Bathe KJ (1982): *Finite-element procedures in engineering analysis*. Prentice-Hall Inc., Englewood Cliffs, NJ.

Békésy, G v (1949): *The structure of the middle ear and the hearing of one's own voice by bone conduction*. J Acoust Soc Am 21: 217-232.

Békésy (1960): *Experiments in hearing*, McGraw Hill, NY.

Bezold F (1882): *Die Corrosions-Anatomie des Ohres*. Cited by Wever EG & Lawrence M (1954).

Bizais Y, Barillot C & Paola RD (1995): *Information processing in medical imaging*. Proceedings of 14th Int. Conf., Kluwer Academic.

Brown BH, Smallwood RH, Barber DC, Lawford PV & Hose DR (1999): *Medical physics and biomedical engineering*. Institute of Physics publishing, Bristol and Philadelphia.

Carmel PW & Starr A (1963): *Acoustic and nonacoustic factors modifying middle-ear muscle activity in waking cats*. J Neurophysiol, 26: 598-616.

Chole RA, Kodama K (1989): *Comparative histology of the tympanic membrane and its relationship to cholesteatoma.* Ann Otol Rhinol Laryngol, 98: 761-766.

Crane Jr. HL, Gibbs NE, Poole Jr. WG & Stockmeyer PK (1976): *Algorithm 508: Matrix bandwidth and profile reduction.* ACM Trans. Math. Software 2, 375-377, complete source in "*Collected Algorithms*" from ACM.

Currey JD (1979): *Mechanical properties of bone tissues with greatly differing functions.* J Biomech, 12: 313-319.

Curry III TS, Dowdey JE & Murry Jr. RC (1990): *Christensen's physics of diagnostic radiology.* Lea & Febiger, 432-505.

Decraemer WF, Maes MA, Vanhuyse VJ (1980): *An elastic stress-strain relation for soft biological tissues based on a structural model.* J Biomech, 13: 463-468.

Decraemer WF, Khanna SM & Funnell WRJ (1989): *Interferometric measurement of the amplitude and phase of tympanic membrane vibrations in cat.* Hear Res, 38: 1-17.

Decraemer WF, Khanna SM & Funnell WRJ (1991): *Malleus vibration mode changes with frequency.* Hear Res, 54: 305-318.

Decramer WF, Khanna SM & Funnell WRJ (1994): *A method for determining three-dimensional vibrations in the ear.* Hearing Research 77: 19-37.

Decraemer et al. (1994): *Bending of the manubrium in cat under normal sound stimulation.* Proc Opt Imaging Tech Biomed, *2329*: 74-84.

Decraemer WF & Khanna SM (1996): *Vibration modes and the middle-ear function.* Proceedings of Middle-ear mechanics in research and otosurgery, Dresden, 21-26.

Decraemer WF, Khanna SM & Funnell WRJ (1999): *Measurement and modeling of the*

3-dimensional vibration of the stapes in cat. Proc Int Symp on recent developments in auditory mechanics (Sendai, Japan, 1999 July), World Scientific Pub., US, UK, Singapore, 36-43.

Decraemer WF, Khanna SM, Rosowski JJ & Merchant SN (2001): *Complete 3 dimensional motion of the ossicular chain in a human temporal bone*. 24th ARO MidWinter Mtg.

Decraemer WF, Gea SLR & Dirckx JJJ (2003): *Three-dimensional displacement of the gerbil ossicular chain under static pressure changes*. 26th ARO MidWinter Mtg.

Dirckx JJJ & Decraemer WF (1989): *Phase shift moiré apparatus for automatic 3-D surface measurement*. Rev Sci Instr, 60: 3698-3701.

Dirckx JJJ & Decraemer WF (1990): *Automatic calibration method for phase shift shadow moiré interferometry*. Appl Opt, 29: 1474-1476.

Dirckx JJJ & Decraemer WF (1991): *Human tympanic membrane deformation under static pressure*. Hearing Research, 51(1): 93-105.

Dirckx JJJ, Decraemer WF, von Unge M & Larsson Ch (1998): *Volume displacement of the gerbil eardrum pars flaccida as a function of middle ear pressure*. Hearing Research 118(1-2): 35-46.

Dirckx JJJ & Decraemer WF (2001): *Effect of middle ear components on eardrum quasi-static deformation*. Hearing Research, 157: 124-137.

Dirckx JJJ & Decraemer WF (2003): *Pressure Induced Eardrum Deformation at Progressive Stages of Middle Ear Dissection*. 26th ARO MidWinter Mtg.

Drake RL, Vogl W & Mitchell AWM (2005): *Gray's anatomy for students*. Churchill Livingstone, Elsevier Inc.

Etholm B & Belal Jr A (1974): *Senile changes in the middle-ear joints*. Ann Otol Rhinol Laryngol, 83(1): 49-54.

Evans FG (1973): *Mechanical properties of bone*. (Thomas, Springfield, IL), p. 35.

Fulghum RS, Chole RA, Brinn JE, Branigan AE (1987): *Mongolian gerbil tympanic membrane. Normal and with induced otitis media.* Arch Otolaryngol, 113: 521-525.

Fung YC (1993): *Biomechanics: Mechanical properties of living tissues*. 2nd edition, New York, Springer.

Funnell WRJ & Laszlo CA (1978): *Modeling the cat eardrum as a thin shell using the finite-element method.* J Acoust Soc Am 63: 1461-1467.

Funnell WRJ, Khanna SM, Decraemer WF (1992): *On the degree of rigidity of the manubrium in a finite-element model of the cat eardrum*. J Acoust Soc Am, 91(4): 2082-2090.

Funnell WRJ & Decraemer WF (1996): *Finite-element modelling of the cat middle ear with elastically suspended malleus and incus*. 19th Midwinter Res Mtg, Assoc Res Otolaryngol, St. Petersburg Beach.

Funnell WRJ & Decraemer WF (1996): *On the incorporation of moiré shape measurements in finite-element models of the cat eardrum*. J Acoust Soc Am, 100(2): 925-932.

Funnell WRJ (1996): *Low-frequency coupling between eardrum and manubrium in a finite element model*. J Acoust Soc Am, 99: 3036–3043

Funnell WRJ, Siah TH, McKee MD, Daniel SJ & Decraemer WF (2005): *On the coupling between the incus and the stapes in the cat*. JARO 6(1): 9-18.

Funnell SM (1989): *An approach to finite-element modelling of the middle-ear.* M.Eng. Thesis, McGill University, Montréal.

Fuse T, Aoyagi M, Koike Y & Sugai Y (1992): *Diagnosis of the ossicular chain in the middle ear by high-resolution CT.* O.R.L. J. Otorhinolaryngol. Relat. Spec. 54, 251-254.

Ghosh SS & Funnell WRJ (1995): *On the effects of incudostapedial joint flexibility in a finite-element model of the cat middle ear.* Proc. IEEE-EMBS 17th Annual Conference & 21st Can. Med. & Biol. Eng. Conf., Montreal: 1437-1438.

Graham MD, Reams C & Perkins R (1978): *Human tympanic membrane-malleus attachment.* Ann ORL 87: 426-431.

Grandin H Jr (1986): *Fundamentals of the finite-element method.* Macmillan Publishing Company, New York, NY.

Guinan Jr. JJ & Peake WT (1967): *Middle-ear characteristics of anesthetized cats.* J Acoust Soc Am, 41(5): 1237-61.

Gulya AJ & Schuknecht HF (1995): *Anatomy of the temporal bone with surgical implications.* The Parthenon Publishing Group Inc., 2nd Edition, Pearl River, NY.

Gundersen T (1976): *Holographic vibration analysis of the ossicular chain.* Acta Otolaryngol., 82(1-2): 16-25.

Gundersen T & Schuknecht HF (1976): *Anatomy of the temporal bone with surgical implications.* 2nd edition Parthenon Press, Pearl River, New York.

Gyo K, Arimoto H & Goode RL (1987): *Measurement of the ossicular vibration ratio in human temporal bones by use of a video measurement system.* Acta Otolaryngol,103: 87–95.

Ham AW & Cormack DH (1979): *Histology.* JB Lippincott Company, 8th edition, 12-16.

Hamelin LP, Labonté F & Pelletier B (1999): *An active contour Snake algorithm.* Internal report, McGill University, Montréal.

Hatamzadeh-Tabrizi (2003): *Using Active Contours for Segmentation of Middle-ear Images.* Master's thesis, McGill University, Montréal.

Heiland K, Goode R, Asai M, Huber A (1999): *A human temporal bone study of stapes footplate movement.* Am. J. Otol. 20(1): 81-86.

Helmholtz HLF (1869): *The mechanism of the middle-ear ossicles and of the eardrum.* Pflügers Arch f Physiol (Bonn) 1: 1-60 (in German; transl by AH Buck & N Smith (W Wood & Co, New York, 69 pp, 1873) and by J Hinton (Pub New Sydenham Soc (London) 62: 97-155, 1974)).

Henson OW Jr. & Henson MM (2000): *The tympanic membrane: highly developed smooth muscle arrays in the annulus fibrosus of mustached bats.* JARO, 1, 25-32.

Henson MM, Rask-Andersen H, Madden VJ & Henson OW (2001): *The human tympanic membrane: Smooth muscle in the region of the annulus fibrosus.* 24th ARO MidWinter Meeting, St. Petersburg Beach.

Henson OW, Henson MM & Cannon J (2001): *Comparative study of smooth muscle and collagen fibers in the attachment zone of the tympanic membrane.* 24th ARO MidWinter Meeting, St. Petersburg Beach.

Herrera D, Maysinger D, Funnell WRJ & Cuello AC (1991): *Quantification of c-fos and GFAP expression following topical application of KCl to the brain surface.* 3rd IBRO World Cong. Neuroscience, Montréal.

Herrera DG, Maysinger D, Almazan G, Funnell WRJ & Cuello AC (1997): *Quantification of CFOS and glial fibrillary acidic protein in (GFAP) expression following topical application of potassium chloride to the brain surface*. Brain Res., 784, 71-81.

Huber T, Willi U, Ferrazzini M, Felix H, Eiber A & Linder T (2001): *The influence of stapes rocking on acoustic perception in the guinea pig*. 24th ARO MidWinter Mtg.

Huber A, Koike T, Wada H, Nandapalan V & Fisch U (2003): *Fixation of the anterior mallear ligament: diagnosis and consequences for hearing results in stapes surgery.* Ann Otol Rhinol Laryngol, 112: 348–355.

Huttenbrink KB (1996): *The middle ear as a pressure receptor.* Proceedings of the International Workshop on Middle-Ear Mechanics in Research and Otosurgery, Dresden, Germany, September 19-22.

Kak A & Slaney M: *Principles of Computerized Tomographic Imaging.* Society of Industrial and Applied Mathematics, 2001.

Kass M, Witkin A & Terzopoulos D (1986): *Snakes: Active Contour Models*. International Journal of Computer Vision, 3, 321-331.

Khanna SM & Tonndorf J (1972): *Tympanic-membrane vibrations in cats studied by time-averaged holography.* J Acoust Soc Am, 51: 1904-1920.

Khanna SM & Tonndorf J (1972): *Tympanic-membrane vibrations in human cadaver ears studied by time-averaged holography.* J Acoust Soc Am, 52: 1221-1233.

Khanna SM & Tonndorf J (1975): *Tympanic membrane shape determined by moiré topography.* J Acoust Soc Am 57 Suppl: 72 (abstract).

Kirikae I (1960): *The Structure and Function of the Middle Ear.* Univ. Tokyo, vi+157 pp.

Koike T, Wada H, Kobayashi T & Takasaka T (1996): *Finite-element method analysis of the human middle ear.* ARO Meet, New Jersey, paper 778.

Koike T, Wada H & and Kobayashi T (2002): *Modeling of the human middle ear using the finite-element method.* J Acoust Soc Am, 111: 1306-1317.

Kuypers LC, Dirckx JJJ & Decraemer WF (2000): *Eardrum thickness measured on confocal microscope virtual sections.* 23rd ARO MidWinter Mtg.

Kuypers L (2005): *Determination of the thickness of the tympanic membrane by confocal laser scanning microscopy.* Doctoral thesis, University of Antwerp, Antwerp, Belgium.

Ladak HM & Funnell WRJ (1996): *Finite-element modelling of the normal and surgically repaired cat middle ear.* J Acoust Soc Am, 100: 933-944

Lang SB (1969): *Elastic coefficients of animal bone.* Science, 165: 287-288.

Lim DJ (1968): *Tympanic membrane. Electron microscopic observation. Part 1. Pars tensa.* Acta Otolaryngol, 66: 181-198.

Lim DJ (1968): *Tympanic membrane. Electron microscopic observation. Part 2. Pars flaccida.* Acta Otolaryngol, 66: 515-532.

Lim DJ (1970): *Human tympanic membrane. An ultrastructural observation.* Acta Otolaryngol, 70: 176-186.

Lobregt S & Viergever MA (1995): *A discrete dynamic contour model.* IEEE Trans. on Medical Imaging, 14 (1), 12-24.

Lynch TJ, Nedzelnitsky V & Peake WT (1982): *Input impedance of the cochlea in cat.* J Acoust Soc Am, 72:108-130.

McInerney T & Terzopoulos D (1996): *Deformable models in medical image analysis.* IEEE Proceedings of the Workshop on Mathematical Methods in Biomedical Image Analysis, 171-180.

Mente PL & Lewis JL (1994): *Elastic modulus of calcified cartilage is an order of magnitude less than that of subchondral bone.* J Orthopædic Res, 12: 637–647.

Merchant SN, Ravicz ME & Rosowski JJ (1996): *Acoustic impedance of the stapes and cochlea in human temporal bone.* Hearing Research, 97: 30–45.

Mikhael CS (2005): *Finite-element modeling of the human middle ear.* Master's thesis, McGill University, Montreal.

Miller JV (1990): *On geometrically deformable models for the extraction of closed shapes from volume data.* Master's thesis, Rensselaer Polytechnic Institute, New York.

Nakajima HH, Peake WT, Rosowski JJ & Merchant SN (2004): *Ossicular ligaments and the axis of rotation.* Abstract & poster from ARO 2004 MidWinter Meeting.

Oaks E (1967): *Structure and function of inflated middle ears of rodents.* University Microfilms, Inc., Ann Arbor, Michigan.

Olson E & Cooper N (2000): *Stapes motion and scala vestibuli pressure in gerbil.* 23rd ARO MidWinter Meeting.

Overstreet EH & Ruggero MA (2002): *Development of a wide-band middle-ear transmission in the Mongolian gerbil.* J Acoust Soc Am, 111 (1): 261-270.

Overstreet EH, Richter CP, Temchin AN, Cheatham MA & Ruggero MA (2003): *High-frequency sensitivity of the mature gerbil cochlea and its development.* Audiol Neurootol, 8: 19-27.

Palva T, Ramsay H & Northrop C (2001): *Color atlas of the anatomy and pathology of the epitympanum*. Karger AG, Basel, Switzerland.

Prendergast PJ, Ferris P, Rice HJ & Blayney AW (1999): *Vibro-acoustic modeling of the outer and middle ear using the finite-element method.* Audiol Neurootol, 4: 185-191.

Ravicz ME & Rosowski JJ (1997): *Sound-power collection by the auditory periphery of the Mongolian gerbil Meriones unguiculatus. III. Effect of variations in middle-ear volume on power collection.* J Acoust Soc Am,101: 2135-2147.

Ravicz ME & Rosowski JJ (2004): *High-frequency sound transmission through the gerbil middle ear.* 27th ARO MidWinter Mtg.

Reilly RJ & Burstein AH (1975): *The elastic and ultimate properties of compact bone tissue*. J Biomech, 8: 393-405.

Rho JY, Tsui TY & Pharr GM (1998): *Elastic properties of osteon and trabecular bone measured by nanoindentation.* J Biomed Mater Res, 45: 48-54.

Rosowski JJ, Teoh SW & Flandermeyer DT (1997): *The effect of the pars flaccida of the tympanic membrane on the ear's sensitivity to sound.* Diversity of Auuditory Mechanics, World Scientific, Singapore, pp. 129-135.

Rosowski JJ, Ravicz ME, Teoh SW & Flandermeyer D (1999): *Measurements of middle-ear function in the Mongolian gerbil, a specialized mammalian ear.* Audiol Neurootol 4(3-4): 129-136.

Ruppert J (1995) :*A Delaunay refinement algorithm for quality 2-dimensional mesh generation*. Journal of Algorithms, 18(3): 548-585.

Siah (2002): *Finite-element modelling of the mechanics of the coupling between the incus and the stapes in the middle ear.* Master's Thesis, McGill University, Montreal, Canada.

Siebenmann F (1897): *Mittelohr und labyrinth*, in Karl von Bardeleben's Handbook of Anatomy of Menschen, V, Abt 2, Lief 6, 195-324.

Silverstein (1972): *Atlas of the human and cat temporal bone*. Thomas publisher, Springfield, IL.

Speirs AD, Hotz MA, Oxland TR, Hausler R & Nolte L-P (1999): *Biomechanical properties of sterilized human auditory ossicles*. J Biomech, 32: 485-491.

Stuhlman O Jr. (1937): *The nonlinear transmission characteristics of the auditory ossicles*. J. Acoust. Soc. Amer. 9: 119-128. Cited by Wever EG & Lawrence M (1954).

Stytz M, Frieder G & Frieder O (1991): *Three-dimensional medical imaging: algorithms and computer systems*. ACM Computing Surveys, 23 (4), 421-499.

Sun Q, Gan RZ, Chang KH & Dormer KJ (2002): *Computer-integrated finite-element modeling of human middle ear.* Biomechan Model Mechanobiol, 1:109-122.

Swartz JD (1983): *High-resolution computed tomography of the middle ear and mastoid, I: normal radioanatomy including normal variations*. Radiology 148, 449-454.

The Columbia Encyclopedia (2004), 6th Edition.

Vander, Sherman & Luciano (2004): *Human physiology: the mechanisms of body function*, 9th Edition.

von Unge M, Bagger-Sjoback D & Borg E (1991): *Mechanoacoustic properties of the tympanic membrane: a study on isolated Mongolian gerbil temporal bones*. Am. J. of Otology, 12(6) 407-419.

von Unge M, Decraemer WF, Dirckx JJ & Bagger-Sjöbäck D (1999): *Tympanic*

membrane displacement patterns in experimental cholesteatoma. Hearing Research, 128(1-2): 1-15.

van Wijhe RG (2000): *A finite-element model of the middle ear of the moustached bat.* Master's thesis, McGill University, Montreal.

Wever EG & Lawrence M (1954): *Physiological acoustics.* Princeton University Press, Princeton, NJ.

Wolff D, Bellucci RJ & Eggston AA (1957): *Microscopic anatomy of the temporal bone.* The Williams & Wilkins Company, Baltimore, MA.

Xu C & Prince JL (1997): *Gradient vector flow: a new external force for snakes.* Proc. IEEE Conf. On Computer Vision and Pattern Recognition, 66-71.

Xu C & Prince JL (1998): *Snakes, Shapes, and gradient vector flow.* IEEE Trans. On Image Processing, 359-369.

Yang X & Henson OW Jr (2002): *Smooth muscle in the annulus fibrosus of the tympanic membrane: physiological effects on sound transmission in the gerbil.* Hearing Research 164: 105-114.

Yezzi Jr. A, Kichenassamy S, Kumar A, Olive P & Tannenbaum A (1997): "A geometric snake model for segmentation of medical imagery," IEEE Trans. on Medical Imaging, 16 (2), 199-209.

Yoon HS & Katz JL (1976): *Ultrasonic wave propagation in human cortical bone-II. Measurements of elastic properties and microhardness.* J Biomech, 9: 459-464.

Zhou X, Peck TL, Litchfield JB (1995): *Magnetic Resonance Microscopy.* Annual reports on NMR spectroscopy, vol. 31, 31-80.

Zienkiewicz OC & Taylor (1989): *The finite-element method.* McGraw-Hill International (UK), 4th edition.